January 2021

Hydraulic Fracture Propagation And Its Geometry Evolvement In Transversely Isotropic Formations

Dezhi Qiu

HYDRAULIC FRACTURE PROPAGATION AND ITS GEOMETRY EVOLVEMENT IN TRANSVERSELY ISOTROPIC FORMATIONS

by

Dezhi Qiu

Bachelor of Mechanical Engineering, Changzhou University, Changzhou, Jiangsu, China, 2015

Master of Petroleum Engineering, Northeast Petroleum University, Daqing, Heilongjiang, China, 2018

A Dissertation
Submitted to the Graduate Faculty
of the
University of North Dakota
In fulfillment of the requirements

for the degree of

Doctor of Philosophy

Grand Forks, North Dakota

August

2021

Name: dezhi qiu

Degree: Doctor of Philosophy

This document, submitted in partial fulfillment of the requirements for the degree from the University of North Dakota, has been read by the Faculty Advisory Committee under whom the work has been done and is hereby approved.

DocuSigned by:
Vamegh Rasouli
0EB956E8C9C9456...
Vamegh Rasouli

DocuSigned by:
Branko Damjanac
7986499872794AB...
Branko Damjanac

DocuSigned by:
Hui Pu
C63B8AB854E4448...
Hui Pu

DocuSigned by:
Kegang Ling
AE10F7CCAFC7487...
Kegang Ling

DocuSigned by:
Iraj Mamaghani
76231706E0AA4C6...
Iraj Mamaghani

This document is being submitted by the appointed advisory committee as having met all the requirements of the School of Graduate Studies at the University of North Dakota and is hereby approved.

DocuSigned by:
Chris Nelson
2E0AF088C733403...
Chris Nelson
Dean of the School of Graduate Studies

7/21/2021
Date

PERMISSION

Title	Hydraulic Fracture Propagation and Its Geometry Evolvement in Transversely Isotropic Formations
Department	Petroleum Engineering
Degree	Doctor of Philosophy

In presenting this document in partial fulfillment of the requirements for a graduate degree from the University of North Dakota, I agree that the library of this University shall make it freely available for inspection. I further agree that permission for extensive copying for scholarly purposes may be granted by the professor who supervised my dissertation work or, in her/his absence, by the Chairperson of the department or the Dean of the Graduate School. It is understood that any copying or publication or other use of this dissertation or part thereof for financial gain shall not be allowed without my written permission. It is also understood that due recognition shall be given to me and to the University of North Dakota in any scholarly use which may be made of any material in my dissertation.

Dezhi Qiu

6/30/2021

Table of Contents

List of Figures

List of Tables

Acknowledgments

I would like to express my sincere appreciation to my senior advisor Dr. Vamegh Rasouli for all his great patience and insightful guidance during my three years Ph.D. study at the University of North Dakota. His knowledge and wisdom helped me open the door to science, and his diligence and hard work will always be an example for me to follow.

The Itasca IEP program provided the XSite license, which was critical to the success of this study. I would like to thank my committee member Dr. Branko Damjanac for kindly answering my questions and providing valuable suggestions. I would also like to thank other members of my advisory committee members Dr. Hui Pu, Dr. Kegang Ling, and Dr. Iraj Mamaghani, for their support and critical comments.

I would like to thank my teammate and best friend Xingcheng Wan for all his assistance in both research and life. I would also thank the whole team members of our hydraulic fracture, Jun Zhang, Xueling Song, Agustinus Zandy, Omar Akash, Nourelhouda Benouadah, Imene Bouchakour, Nejma Djabelkhir, and Foued Badrouchi. The in-depth discussions we had at the group meeting will not only help me in my research but will also serve as a lasting memory for us.

Last but not least, I would like to thank my parents, Kuanfang Qiu and Chunlan Zhang, for their support and encouragement during my pursuit of a Ph.D. I owe special thanks to my fiancée, Rui Huang, for all her endless love and sincere encouragement in my tough time. Wish our love would last forever.

Abstract

During the last two decades, the oil and gas industry started production from unconventional reservoirs, thanks to the rapid development of hydraulic fracturing technology. Fractures such as joints, faults, veins, and bedding planes are ubiquitous in unconventional formations such as laminated reservoirs. These discontinuities always form complex networks affecting the hydrological and mechanical behavior of subsurface rocks. Ideally, hydraulic fractures are expected to communicate these fracture networks to form a continuous path for fluid flow. However, the interaction mechanism between hydraulic fracture and natural fractures may result in different propagation paths to form various fracture geometries and stimulated reservoir volume (SRV). In order to optimize the fracturing treatment and predict the SRV in fractured reservoirs, it is necessary to investigate the fracture propagation pattern from the simple interaction modes between hydraulic fracture and natural fractures to complicated single and multi-stage fracture propagation in laminated reservoir perspectives.

This research is divided into three sections. In the first section, a novel model was proposed based on a lattice-based simulator, XSite, to predict interaction modes between hydraulic fracture and natural fractures considering the effect of formation mechanical properties, stress state, and fluid injection parameters. To build this predictive model, a number of fracturing simulations were executed to provide pressure time and interaction modes data. The conception interaction pressurization rate index (IPRI) obtained from pressure time data was proposed as an indicator to characterize the interaction modes. Several lab experiments were used to verify the accuracy of the predictive model.

In the second section, a more common fracture model was built to study the hydraulic fracture propagation in the laminated reservoir, which contains the natural interfaces and caprock layers, both significantly affecting the hydraulic fracture geometry. The results indicated that injection rate and caprock Young's modulus prone to the fracture propagation in the horizontal direction or along the interfaces, thus stress anisotropy and interfaces and caprocks tensile strength favor to the fracture propagation in the vertical direction as a tensile fracture.

In the third section of this research, a representative multi-stage model was developed to study the influence of formation properties and injection parameters on fracture evolution in the laminated reservoir. Tension and shear stimulated area were proposed to quantify the fracture propagation modes and directions in formation. A statistical method was used to build the predictive model to evaluate the formation stimulation potential based on considering contribution of all influential parameters. A series of artificially generated in possible range influencing factors verified the accuracy of the proposed model.

These three sections progressively investigate the propagation of hydraulic fracture in laminated reservoirs and develop a model for evaluating the reservoir's stimulation potential, which provides a guide for fracturing field operations.

Chapter 1

Introduction

1.1 Hydraulic Fracturing

Hydraulic Fracturing (HF), or commonly referred to as fracking, is currently the key stimulation technology in shale plays and tight reservoirs which exhibit very low permeability. HF is commonly applied in long horizontal laterals in order to create larger exposure area to the formation. The lateral length could be up to 10,000ft and the fracking is done in multi stages, up to 50, such as Bakken Shale in the Williston Basin in North Dakota, USA (Alcoser et al., 2012). HF operation relies on utilizing pressurized fluid as a transport power medium to initiate a bi-wing fracture plane from the wellbore and then keep pumping to propagate the fracture into the reservoir for a few thousand feet (Cheng & Zhang, 2020). It is known that the fracture propagates perpendicular to the minimum in-situ stress, also called preferred fracture propagation (PFP) direction (Fallahzadeh et al., 2017). Formation elastic properties and stress anisotropy, together with the injecting fluid's viscosity and flow rate are the key parameters in forming the geometry of the induced fracture. Therefore, the successful operation of a fracking job is inseparable from understanding the combined effect of different parameters, which indeed is a very complex problem to fully understand. Fracking in a brittle formation with relatively high stress anisotropy based on a good pumping schedule design results in large micro fracture to develop around the

main fracture plane. This shattered area, where aids the hydrocarbon to be drained and flow into the main fracture plane and then to the wellbore, defines the stimulated reservoir volume (SRV) or drained area. The SRV is used to establish the distances between different fracking stages along a lateral and the spacing between the adjacent horizontal wellbores (Waters et al., 2009). The application of the microseismic has been of significant use and benefit to the industry in order to post diagnose the success of a fracking job, as the cloud of data developed from microseismic shows the extension of the propagated fracture (Calvez et al., 2016). This technology, however, is costly and requires several steps of data filtering and analysis before interpretation.

1.1.1 HF in a Fractured Media

As briefly discussed above, HF is a complex problem with several parameters involved in the design of a fracking job. The problem becomes more complex when fracture propagation is studied in discontinuous media, such as naturally fractured reservoirs, laminated formations including shales or multi layered reservoirs. In any reservoir, some type of natural interfaces (NI) exist, so it is important to understand the effect of them on the propagation of the induced hydraulic fracture. Natural interface is a weak plane with generally negligible cohesion and toughness and the potential to be the fluid channel by activation (Wang, 2019).

The interaction between HF and NI can lead to three modes of crossing, opening, and arresting as schematically shown in Figure 1.1 (Sarmadivaleh, 2012). The parameters affecting the mode of interaction include the state of stresses, formation toughness on two sides of the NI, the angle at which the HF intersects the NI (angle of approach), frictional property of the NI, and the injecting fluid viscosity and rate. Several analytical models have been presented to define which interaction mode will take place. However, all these models are based upon simplified assumptions and only consider a few parameters (Blanton, 1986; H. Gu & Weng, 2010; Renshaw & Pollard, 1995). The

results of lab experimental works carried out by different researchers are beneficial in terms of post diagnosis of the interaction mode by visual observation and inspection of the samples. However, conducting valid, repeatable, and representative experiments under true triaxial stress conditions on cubical samples is very costly and time consuming. Numerical simulations have been extensively used for this purpose, based on the continuum and discontinue models (Dou et al., 2021; Nagel et al., 2013; Rueda et al., 2019; Shi et al., 2017; Q. Zhang et al., 2019). Any numerical simulation is useless unless it is calibrated and the results are validated using real data, either from lab or field. Once the simulation is adequately calibrated it may be used with precautions in order to predict the interaction mode and do several sensitivity analysis of different parameters (Bakhshi et al., 2019; Y. Zhou et al., 2020). In real field applications, the use of the microseismic will be of great help to see the extension of the HF and the mode of interaction. As noted earlier, this is an expensive method with great effort to set up the hardware to run the test and then filter and process the data. More importantly, the data are available after the conclusion of the HF operation, so real time observation of fracture propagation is not practical (Maxwell, 2011). Figure 1.2 shows, as examples, a proposed analytical model for predicting interaction modes, view of a sample after HF lab test, the results of numerical simulations showing the crossing mode, and the microseismic data cloud in a HF job in a naturally fractured reservoir. In the next chapter, a review of past analytical models, lab experimental studies, and numerical simulations to predict the interaction mode will be presented. It will also be mentioned that in this study we will use XSite software, which is a particle-based numerical simulator.

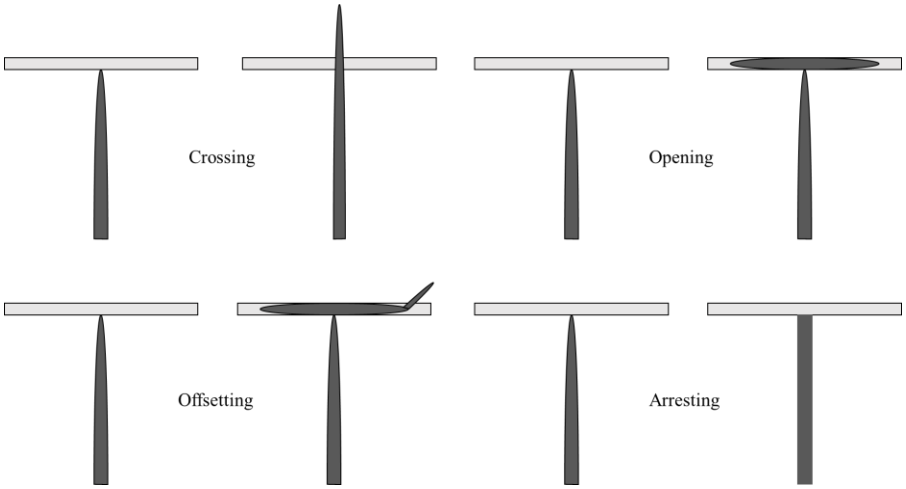

Figure 1.1 Four types of typical hydraulic fracturing interact with the natural fracture schematic diagram.

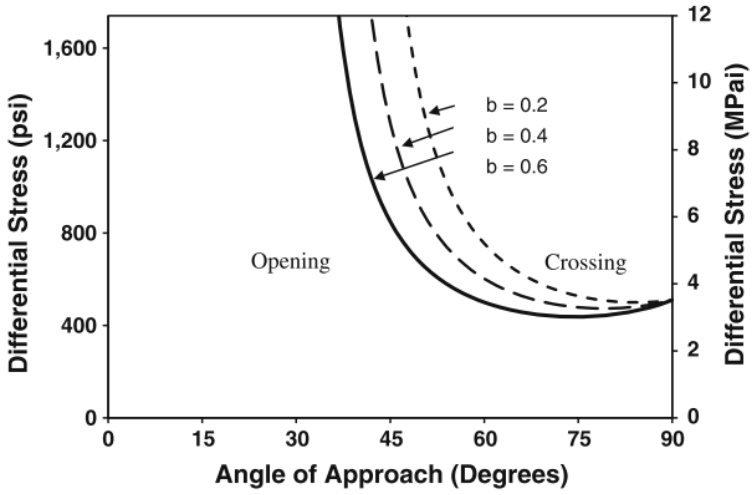

(a)

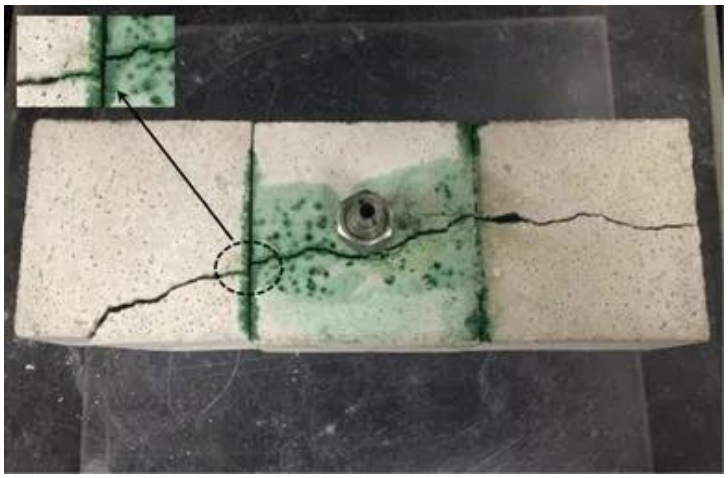

(b)

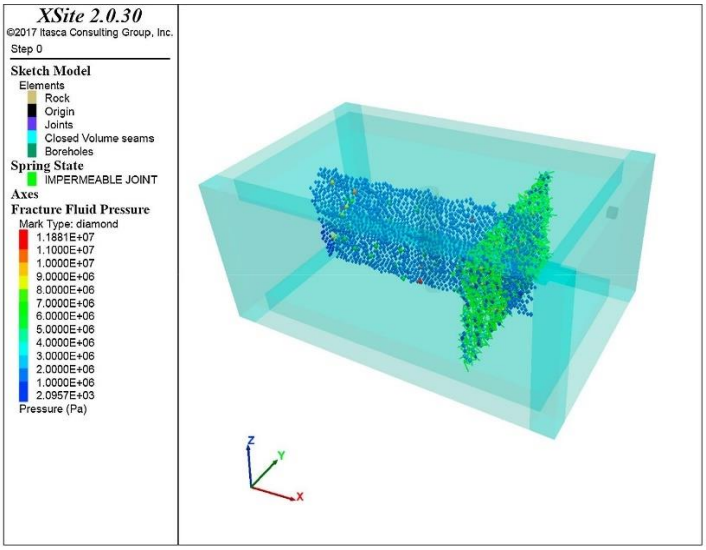

(c)

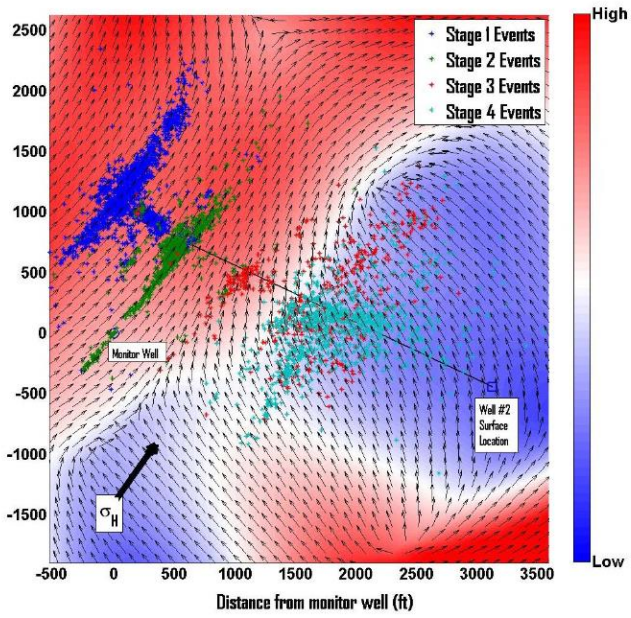

(d)

Figure 1.2 Examples for four methods (a) interaction prediction with analytical solution (b) Lab experiment (c) Case with XSite simulator (d) HF treatment in naturally fractured formation record with seismic events (Fu et al., 2016, 2019; Rich & Ammerman, 2010; Sarmadivaleh, 2012).

1.1.2 Discrete Fracture Network (DFN)

Discrete fracture network (DFN) refers to computational models that explicitly represent the geometrical properties of each individual fracture (e.g., size, length, orientation, aperture), and the topological relationships between individual fracture and fracture sets. This is done based on geological mapping, stochastic generation, and geomechanical simulation to characterize the naturally fractured reservoir (Lei et al., 2017). The distribution of natural fractures can be estimated from the fractures predicted by seismic, borehole image logs, structural geology information, and other methods (Bourne et al., 2000). Figure 1.3 shows an example of DFN, which is used for numerical simulations.

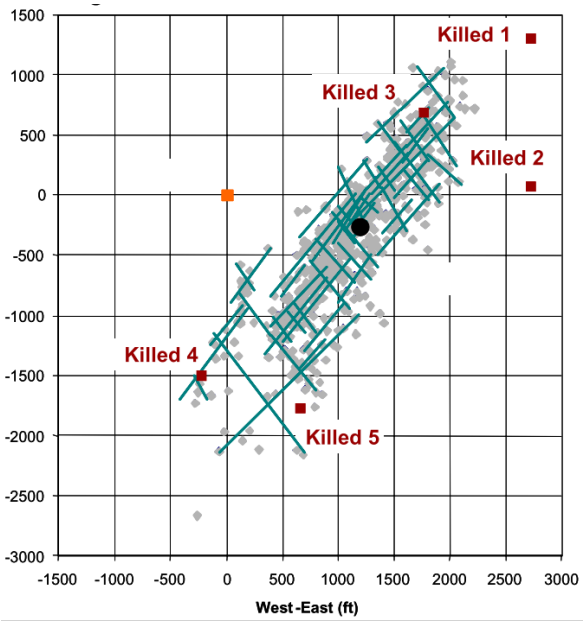

Figure 1.3 Example of fracture treatment map with top view. Gray dots are microseismic events and green lines are fracturing paths (Fisher et al., 2004).

The lack of adequate knowledge about the natural fractures (NF) geometrical and mechanical properties leads to an incorrect prediction of the interaction mode, regardless of what model is used, as compared with the real field. Seismic cannot capture small fractures, and its accuracy reduces as a function of depth. The borehole image logs have limited depth of investigation and

other methods suffer from their own shortcomings. Therefore, it is a challenge to correctly represent the distribution of the NFs in a given reservoir using the DFN.

The above challenges and the real need of the industry in better estimation of the HF geometry and SRV elicited the idea for this research study. This is presented in the next Section.

1.1.3 Bottomhole Pressure Data Diagnosis

As stated in the previous sections, the prediction of the interaction mode is of significant importance in a HF operation. In this research, the idea is to study the bottom hole pressure data during a HF job real time to see if there is any indication of what mode of interaction may occur. The initial idea was borrowed from the Nolte-Smith net pressure-time plot also known as the log-log plot presented in Figure 1.4 (Economides & Nolte, 2000). This plot shows four possible paths of pressure changes for fracture extension. Type 1 indicates the increasing net pressure as the fracture propagates in a confined height formation. Type 2 is a constant pressure plateau that can result from unstable growth or fluid loss. Type 3 represents the restricted propagation of hydraulic fracturing. Type 4 shows the fracture crossing a barrier and encountering a lower stress zone. According to the interpretation of different plots, Type 3 and 4 may represent interaction modes between HF and NI.

The expectation is that different parameters will affect the response of the log-log plot depending on their contribution to the interaction mode. Therefore, the idea is to use the analytical models as the initial guide to numerically simulate many different cases of interaction modes by sensitivity analysis of different parameters and compare the change in the log-log plot responses.

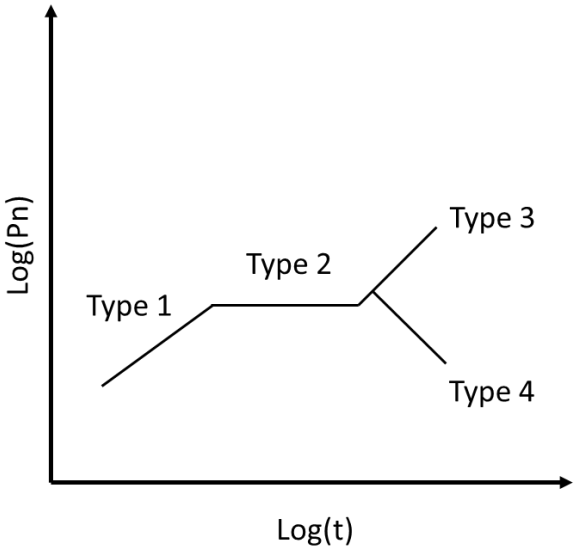

Figure 1.4 Log-log pressure-time interpretation plot for various fracture propagation modes.

The proposed method is based on real time monitoring of pressure data during the HF job, so the hope is that it helps to monitor and predict the interaction mode live and take necessary treatment actions immediately as necessary. This could be, for instance, the change in fluid viscosity. In addition to real time interpretation of pressure data, this is a low-cost method comparing to microseismic. However, it is not suggested that this proposed method to replace microseismic but used as an early tool to diagnose the interaction mode and complementary to the microseismic.

By simulating a large number of interaction cases, a bank of data representing the impact of different parameters on the interaction mode will be produced. This data can be used for predicting the interaction mode based on big data analytics, artificial intelligence (AI) algorithms, and similar approaches.

1.2 Research Objectives

This thesis aims at developing a quantitative model to predict the HF and NI interaction modes as well as predicting the fracture propagation and its geometry evolvement in transversely isotropic formations. The specific objectives of this study are summarized here:

1. A comprehensive review of the past research and studies on prediction of the interaction mode and hydraulic fracture propagation path in fractured or laminated reservoirs, including analytical models, experimental studies, numerical simulations, and field work. In specific, the objective is to assess the impact of different parameters on the fracture propagation path and geometry evolution based on past studies.

2. Use the lattice numerical simulation using XSite software in this study and highlight the advantages of using this particle-based distinct element method for the applications of this work.

3. Run a number of representative numerical simulations with changing different parameters and analyze all extracted quantitative parameters from corresponding pressure-time curves to build a data mining based predictive model to find potential relations between interaction modes and pressure curve change. We use the lab experiment data as examples to assess the application of the developed model.

4. Execute a number of simulations to study the single cluster fracture propagation path in the laminated reservoir, which is contained by upper and lower caprock layers. Hydraulic fracture penetrate-ability in vertical versus connectivity in horizontal are quantitatively analyzed with the impact of different mechanical properties and injection parameters in the possible range.

5. Further study on multi-cluster hydraulic fracture propagation patterns in a laminated reservoir is modeled with XSite. We consider the effect of all parameters on fractures propagation in terms of vertical and horizontal patterns and qualitatively measure the contribution of each influential parameter on penetrate-ability and connectivity.

6. A predictive model is built based on the analysis of the contribution of all influencing factors to evaluate stimulation potential considering fractures initiated from multi-clusters in the medium as laminated, which is more representative of the real field.

1.3 Research Methodology

In order to achieve the objectives of this research as set above, we do the following steps.

1. XSite, a new lattice-based method, will be used in this study to run a large volume of numerical simulations based on real field data.

2. The analytical models will be first used to compare with few simulation results for the verification purpose.

3. A large volume of simulation data will be collected as a database in this study for data mining purposes to find the potential relations between simulation results and pressure curve change.

4. Nondimensionalization of all influencing factors facilitates the comparison of each factor's impact on hydraulic fracture propagation.

5. Statistical models will be used to achieve the weight functions to characterize the stimulation potential considering the effect of each parameter.

6. Schematic plots of stimulated area plots will be presented as a result of this work to indicate the impact of each parameter change on the fracture propagation.

1.4 Significance

This research creates a novel method to diagnostic the interaction mode and then further analyze fracture propagation from single to multi clusters and its geometry in fractured or laminated reservoirs. This work is distinguished from similar studies in multifold, including:

1. The use of the newly developed XSite software and its unique features will be a new practice in this study.
2. The use of some analytical models will be examined throughout this study and can provide a good understanding of their usage limits.
3. The proposed methodology can be applied real time by monitoring the change of the pressure data during the HF operation job or in the lab. This carries several advantages compared to microseismic and other diagnostic methods.
4. The tension and shear stimulated area will be used to predict the impact of each parameter and the fracture geometry evolution that may occur based on the analysis of tension and shear stimulated area.
5. The integrated model is capable of evaluating stimulation potential, especially in complicated geological conditions like fractured or laminated reservoirs.
6. The use of statistical models to determine the weight functions corresponding to the impact of each parameter is of great use for implication by other researchers.

1.5 Thesis Structure

This thesis is composed of six Chapters.

Chapter 1 briefly introduces the concept of the interaction modes and hydraulic fracture propagation in transversely isotropic media. This Chapter also includes the objectives, methodology, and significance of this research.

A review of analytical models, experimental studies, and numerical simulations to predict the interaction modes and propagation pattern in the laminated reservoir will be presented in Chapter 2. These approaches are compared, and the advantages and shortcomings of each method will be highlighted.

Chapter 3 includes the results of a large number of numerical models where sensitivity analysis of different parameters is done to determine their impact on the interaction mode. These results are collected as a database to develop a model with a statistical method for predicting interaction modes. Lab experiments will be compared with predicted data to prove the accuracy of the developed model.

Several parameters are analyzed regarding their impact on hydraulic fracture propagation geometry in the laminated reservoir will be presented in Chapter 4. The total stimulated area consisted of tension and shear stimulated area, which is used to distinguish the hydraulic fracture propagation path and quantitatively demonstrate each parameter contribution to the transition of propagation path in laminated formation.

Chapter 5 presents a study of a more representative multi-cluster hydraulic fracture propagation in a laminated reservoir. All possible influencing factors on hydraulic fracture are considered in this

study to develop a weight function to evaluate the contribution of each factor to stimulation potential.

Chapter 6 presents the conclusions of this study with some recommendations for future work.

1.6 Summary

This Chapter presented the importance of predicting the interaction mode when a hydraulic fracture intersects a natural interface as well as the fracture geometry evolution in fractured formation. It was discussed that different parameter has different contributions to interaction modes and fracture propagation in barrier layer provide a chance to correctly predict the fracture geometry in complicated formation. The concept of the stimulated area data analysis, as a new method to predict the fracture propagation path developed in this study, was presented. Accordingly, the objectives, research methodology, and significance of this research study were outlined.

In the next Chapter, a summary of some of the past studies done to predict the interaction modes and fracture geometry will be presented.

Chapter 2

Literature Review

In this Chapter, a brief discussion on different parameters affecting the initiation and propagation of hydraulic fracture will be presented. This will be followed by a summary of some of the major analytical models already used to predict the interaction modes. Also, some aspects of numerical simulations of the interaction mode will be reviewed. This Chapter will conclude with a review of some diagnostic methods for HF propagation.

2.1 HF Pressures & Geometry Models

As mentioned in the previous Chapter, HF is the prime technology to stimulate unconventional plays. In general, in a HF job, a viscous fluid is injected through an isolated section of the wellbore, commonly horizontal laterals, in order to initiate and propagate a fracture plane of a few hundred feet into the reservoir. Figure 2.1 shows schematically the plot of the pressure-time curve obtained during the job. As the fluid injection is done at a constant flow rate, any change in the slope of this curve is related to the change of the rock volume, assuming there is not much leak into the formation. After the injection of the fluid some initial fractures are developed around the wellbore with fluid leakage and invasion into the formation near the wellbore. This point, known as the leak-off point, is usually associated with a small reduction of the pressure. Continuation the fluid injection, a fracture will open at the wellbore wall, and a noticeable drop in pressure is observed.

This is the breakdown pressure, after which under constant flow rate, the fracture propagates perpendicular to the minimum stress direction. Once the designed length for the fracture is reached the pump is stopped and a sudden reduction in pressure is happening due to removal of all existing frictions along the flow path. This pressure is known as the instantaneous shut-in pressure (ISIP). Then the fracture will start to close due to the force of the minimum stress component unless proppant has been injected to keep it open. The pressure ultimately reaches the fracture closure pressure, which is equivalent to the minimum stress (Feng et al., 2015).

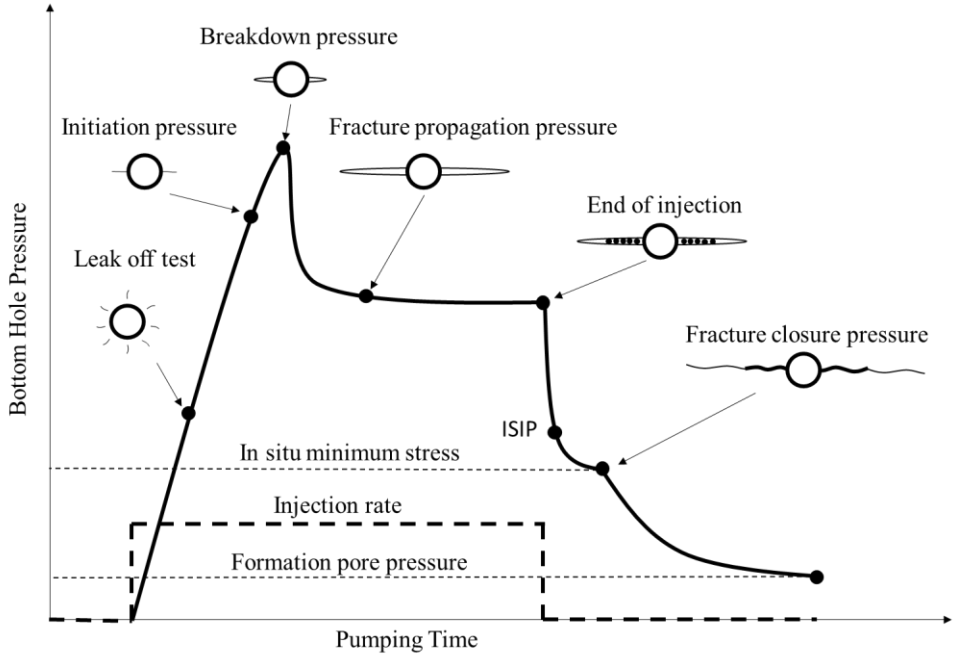

Figure 2.1 A typical hydraulic fracturing pressure-time curve (Sarmadivaleh, 2012).

Typically, there are three kinds of hydraulic fracturing propagation models: Perkins-Kern-Nordgren (PKN) model PKN (Nordgren, 1972; Perkins & Kern, 1961), Khristianovich-Geertsma-DeKlerk (KGD) model (Geertsma & Klerk, 1969; Khristianovic & Zheltov, 1955), and Penny shape model (Savitski & Detournay, 2002). Figure 2.2 shows a schematic diagram of these three models. PKN model is generally regarded to be suitable for fractures whose length/height ratio is

large. In contrast, in the KGD model the fracture is assumed to have a small length/height ratio. In a penny shaped fracture, it is considered that HF initiated from a point source and propagates radially. These 2D models are used in much commercial software to predict the geometry of the propagating fracture. However, as we will discuss later on, the fracture plane is not necessarily straight and, in most cases, follow a complex path due to the field stresses and rock texture. The use of models that can capture this complex geometry is preferred and will be used in this study (see Chapter 4 and 5).

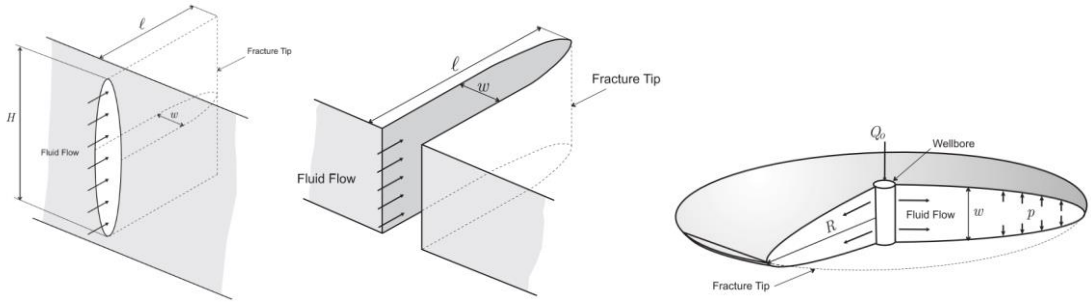

(a) **(b)** **(c)**

Figure 2.2 2D fracture geometry models: (a) PKN, (b) KGD, and (c) Penny-shaped (Adachi et al., 2007).

2.2 Parameters Affecting HF Pressures & Geometry

2.2.1 Stress anisotropy

The larger the stress anisotropy, the more straight the fracture plane will be. In the presence of low stress anisotropy, the rock texture will dominate the propagation of the fracture plane, hence the fracture follows the path of low resistance due to unlocked grains, weak cementing, natural fractures, and any other defects in the rock. In this situation fracture network will form with much less length as opposed to when the stress anisotropy is high. This type of geometry is also expected when the rock is more brittle or frackable, which is due to the high Young's modulus and the existence of more quartz minerals. This is shown schematically in Figure 2.3, where one can see how shales in different fields in North America have different behavior. In Bakken formation in

North Dakota, USA, where some of the largest shale oil production is ongoing, a complex fracture network is more observed as the field experiences relatively low stress anisotropy. We use Bakken data in the future Chapters as part of the analysis presented in this study.

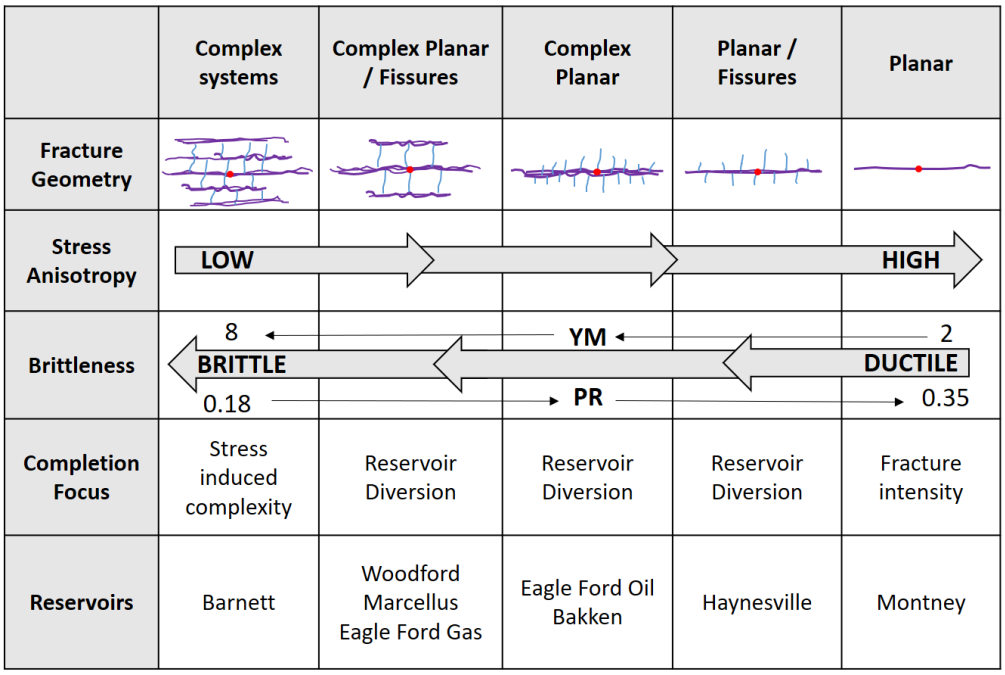

Figure 2.3 Hydraulic fracture geometry with the influence of stress anisotropy and brittleness (Leem et al., 2014).

Combining the stress anisotropy and the density of natural fractures in the field may result in different stimulated reservoir volumes (SRVs). As depicted in Figure 2.4, when the stress difference increases from 0 to 15 MPa, the induced fracture becomes larger in length and less dispersed into the natural fracture systems, which means more penetration into the formation. Therefore, a good knowledge of fracture systems in the field, which may be obtained using seismic data, as well as knowledge of field stresses, are essential to study the shale reservoirs and more accurately estimate the success of a HF job.

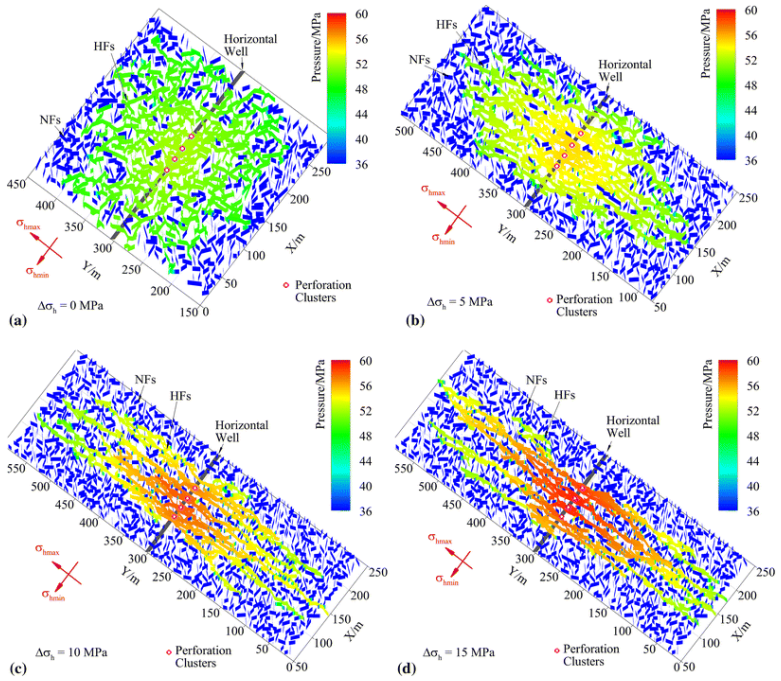

Figure 2.4 HF geometry due to the increase of stress anisotropy in a naturally fractured formation (Yushi et al., 2016).

2.2.2 Rock Properties

Different rock properties will affect the propagation of HF differently. The major rock properties of importance to our discussion are Young's modulus, Poisson's ratio, tensile strength, and toughness.

Young's modulus is the ratio of stress over strain when the rock is under compression load. This value is an indication of rock stiffness. The larger Young's modulus, the more brittle the rock and better for HF operation. The Poisson's ratio, which is the ratio of lateral to axial displacement of a rock under compressional load, responds in an opposite way. As the Poisson's ratio or rock deformability is increased, the brittleness reduces, which is less favorable for HF operation. The combination of Young's modulus and Poisson's ratio has been used to define the brittleness parameter in addition to several other parameters presented by other researchers (Mews et al., 2019).

Tensile strength is a measure of rock's resistance to breakage under tension load (Sun et al., 2018). It is usually considered as 10% of rock's uniaxial compressive strength (UCS), as due to the existence of fractures and other defects, rocks are very weak in tension. Tensile strength has a partial effect on fracture initiation pressure and it has a correlation with fracture toughness (Feng et al., 2016).

Fracture toughness represents the resistance of an existing fracture in a rock to propagate. This is in fact, the energy required to propagate the fracture and its dimension is MPa. $m^{0.5}$ (or psi. $in^{0.5}$). In general, the larger the fracture toughness, the more brittle the rock.

2.2.3 Fracturing Fluid Rheology

Fracking fluid is the only operational parameter that can be controlled during a HF operation. Initially, a low viscosity fluid, known as the pad, is injected to create the fracture. Then to propagate the fracture, a higher viscosity slurry with some small size grains (proppant) is injected in different steps to shape the fracture and keep it open after the shut-in pressure (Isah et al., 2021). Injection rate (Q) and fluid viscosity (μ) are the two operational parameters that can be changed during the design. The larger the flow rate, the higher the breakdown pressure. Also, by increasing the viscosity, the fracture propagates less in length and has a larger opening. Figure 2.5 shows examples of fracture network geometry as a function of flow velocity and fluid viscosity. The product of flow rate and viscosity is a measure of the energy that is applied by the fluid to propagate fracture and is referred to as the pressurization rate (μQ). Increasing the pressurization rate usually results in longitudinal (axial) fractures, where the fracture length is formed along the wellbore axis, as opposed to the transverse fracture, which is perpendicular to the borehole axis (Nejma, 2020). Figure 2.6 shows examples of axial and transverse fractures.

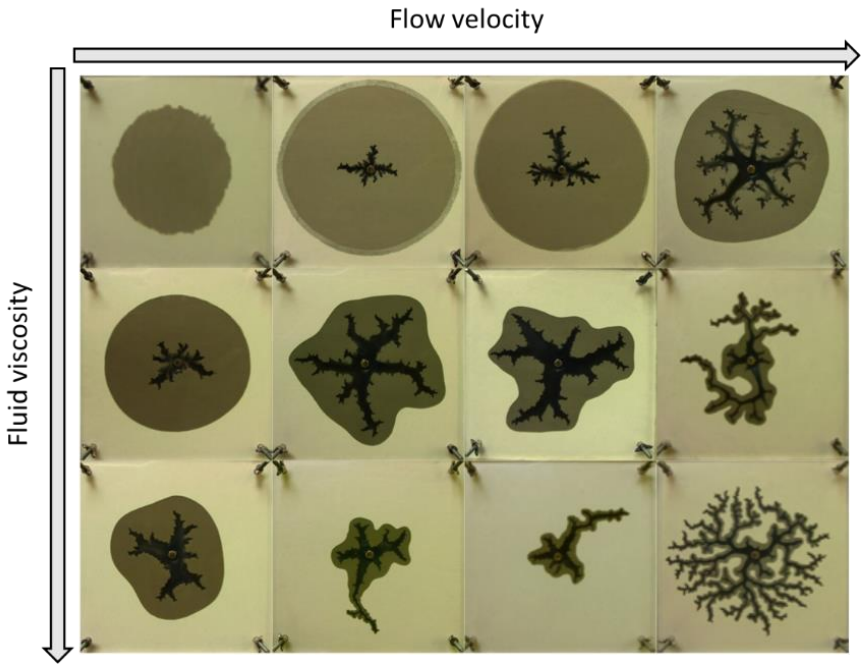

Figure 2.5 Fluid viscosity and velocity impact on hydraulic fracture. Light colored areas are dry sands only; black area is fluid only; brown colors are infiltrated area (Zhang, 2012).

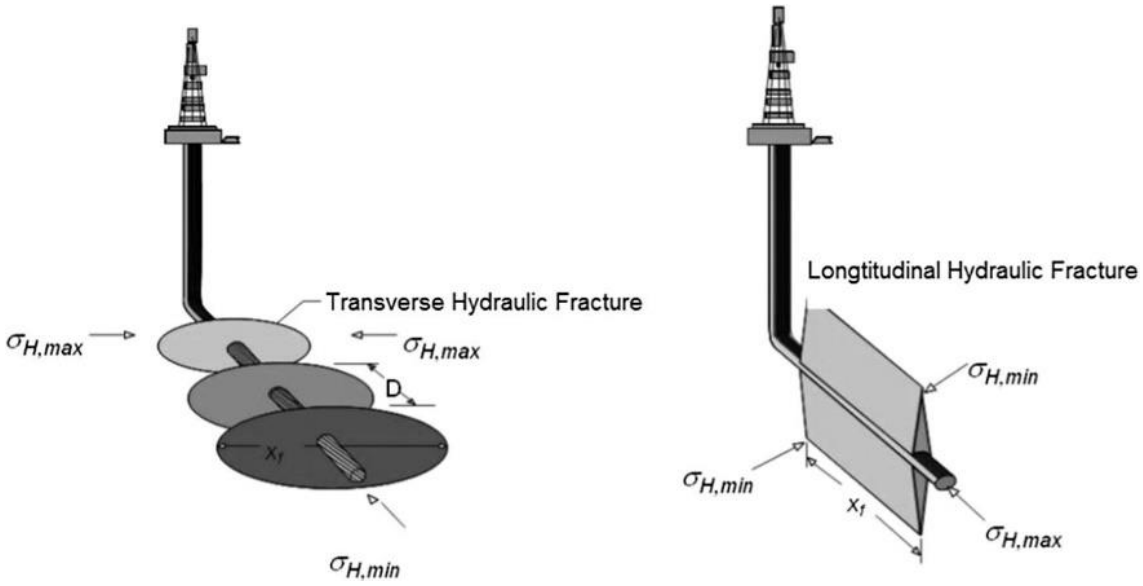

Figure 2.6 Fracture configuration from a horizontal well (Wang, 2016).

2.3 HF and NFs Interaction Modes

As discussed in Chapter 1, crossing, opening, and arresting are the three major interaction modes that are observed when a HF intersects a natural interface. Several factors may influence the type of the interaction modes, including state of stresses and stress anisotropy, formation toughness on the two sides of the interface, injecting fluid properties, and the frictional properties of the interface plane (Lu et al., 2020). The impact of each parameter on the interaction mode is discussed in the following subsections.

2.3.1 Parameters Affecting Interaction modes

2.3.1.1 State of Stresses

Figure 2.7 illustrates the impact of stress anisotropy on the induced fracture geometry. Large stress anisotropy will result in a single planar fracture, whereas low stress anisotropy can lead to a wide and complex fracture system (Qiu et al., 2019).

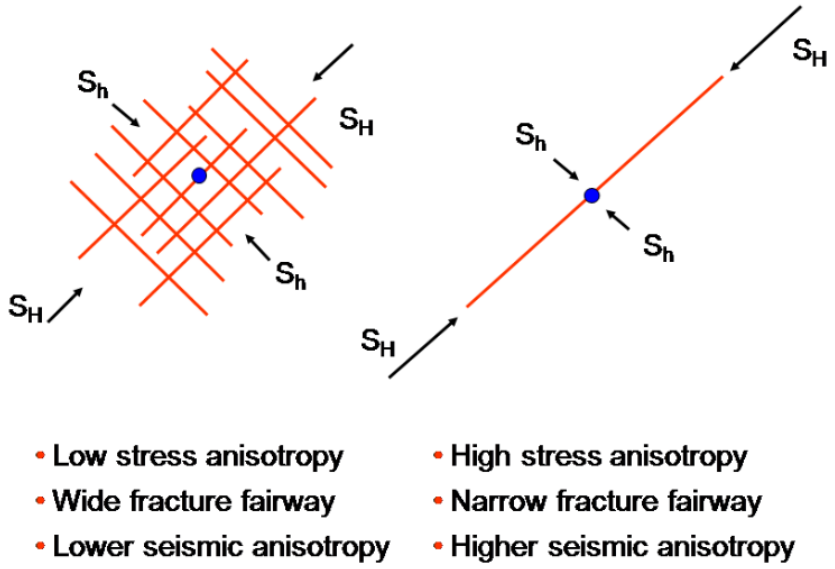

Figure 2.7 Fracture fairway affected by stress anisotropy (Sayers & Calvez, 2010).

2.3.1.2 Natural Interface Properties

The frictional properties of the natural interface may have a substantial impact on the type of interaction modes occurring. Slippage of an interface is attributed to the interface shear strength, which is determined by interface friction angle and cohesion. Once the interface experiences slippage, the fluid has more chance to enter the fracture plane and open it (Tang & Wu, 2018). The analytical models predict opening when there is no slippage occurring. For Middle Bakken, the formation is composed of 50% calcite, 40% quartz, and 10% clay (Schmidt et al., 2011). This results in friction coefficient of $\mu_f = 0.5$, which is an indication of relatively low interface friction leading to the large fracture fairway (see Figure 2.8) with large SRV (Dohmen et al., 2014).

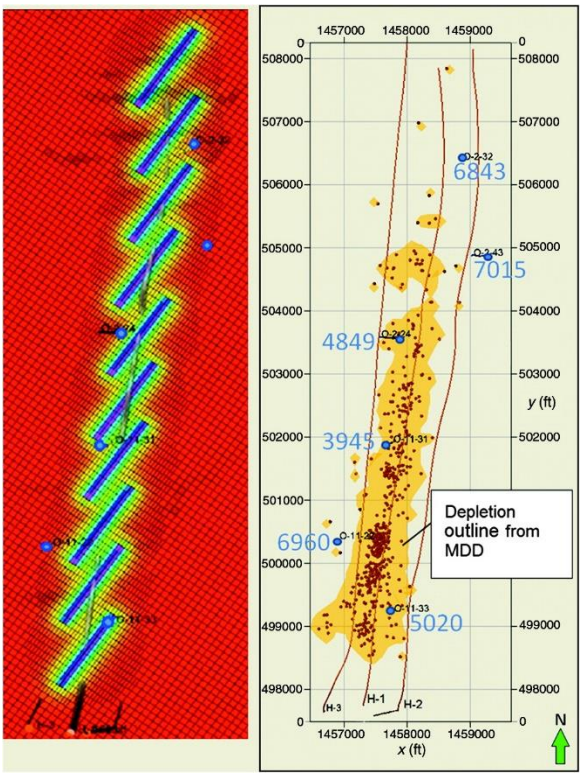

Figure 2.8 Comparison between the reservoir simulation model and actual measurement of depletion of a Bakken production well (Dohmen et al., 2014).

2.3.1.3 Injecting Fluid Properties

As discussed in the previous Section, the injection rate and fluid viscosity of the fracking fluid will affect the fracture pressures. Similarly, these parameters can influence the type of interaction modes. The results of both numerical simulations and lab experiments indicate that higher injection rates may increase the tendency of the crossing mode (Chuprakov et al., 2014). In this study, we will numerically simulate the effect of fluid properties on the interaction mode. The details will be presented in Chapter 3.

2.3.1.4 Angle of Approach

The relative angle between HF and natural interface, also referred to as the angle of approach, has a dominant effect on the interaction mode. This is because the change of this angle will result in different magnitude of normal and shear stresses to the natural fracture plane. Therefore, one can understand that the potential for crossing mode is increasing as the angle of approach get closer to 90°, as in this case the shear component of the stress on the natural interface becomes less. Figure 2.9 presents the results of analytical solutions of the crossing versus opening interaction modes as functions of stress anisotropy (σ_H/σ_h) and interface friction angle with respect to the angle of approach. The areas on the left side of each curve represent the combination of different parameters satisfying the opening mode as opposed to the areas on the right side of each curve representing the crossing mode (Sarmadivaleh, 2012). From this Figure, it is seen that as the stress anisotropy increases, the crossing can occur at a lower interface friction coefficient. Also, the larger the angle of approach, the easier the crossing mode.

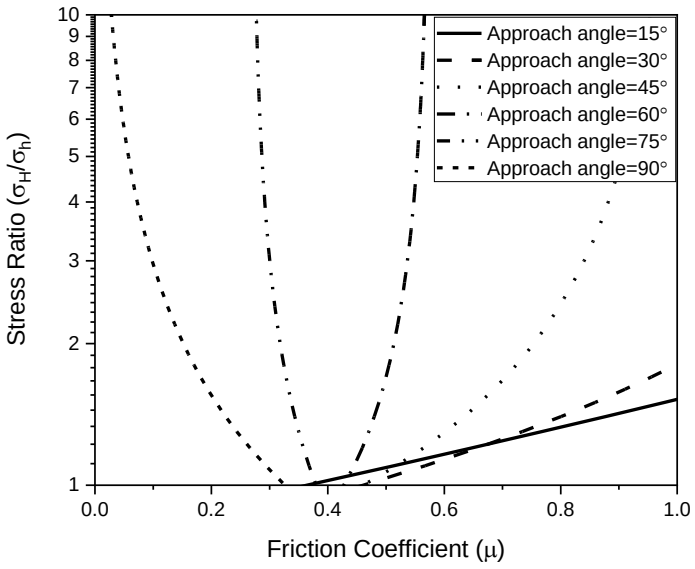

Figure 2.9 Crossing versus opening modes as a function of stress anisotropy, friction coefficient, and angle of approach with some real Bakken formation parameters (Sarmadivaleh, 2012).

2.3.2 Interaction Modes: Analytical Models

Different analytical models have been proposed by researchers to predict the interaction modes. Similar to any analytical solutions, these models are based on some simplified assumptions and may ignore the impact of some parameters. However, the use of analytical models is beneficial in terms of obtaining an understanding of the range of the parameters' values, do sensitivity analysis over different parameters, and use the results as a starting point for further analysis. In the following subsections, some of the important analytical models are presented.

2.3.2.1 Blanton's Criterion

Blanton (1986) proposed a criterion to explore the HF propagation modes when fracture intersects with a natural fracture. The pumping fluid at the intersection point may open or reinitiate on the other side of the natural fracture. Based on his criterion, the opening mode occurs when fluid pressure exceeds the normal stress on the natural interface and is less than the pressure for reinitiation on the other side of the interface. Crossing may happen when the reinitiation pressure

is less than opening pressure. A criterion was proposed to determine when fluid pressure exceeds the normal stress and tensile strength of the interface:

$$P > \sigma_T + T_0 \tag{2.1}$$

In this equation, T_0 is the rock's tensile strength, and σ_T is the superposition of the remote field stress and interaction induced stress related to natural fracture properties. Therefore, Blanton derived a crossing criterion in the form of:

$$\frac{(\sigma_{max} - \sigma_{min})}{T_0} > \frac{-1}{cos\ 2\theta - b\ sin\ 2\theta} \tag{2.2}$$

where:

$$b = \frac{1}{2c}\left[v(x_0) - \frac{(x_0 - l)}{\mu_f}\right] \tag{2.3}$$

and:

$$x_0 = \left[\frac{(1+c)^2 + e^{\frac{\pi}{2\mu_f}}}{1 + e^{\frac{\pi}{2\mu_f}}}\right]^{0.5} \tag{2.4}$$

$$v(x_0) = \frac{1}{\pi}\left[(x_0 + l)ln\left(\frac{x_0 + l + c}{x_0 + l}\right)^2 + (x_0 - l)ln\left(\frac{x_0 - l - c}{x_0 - l}\right)^2 + cln\left(\frac{x_0 + l + c}{x_0 - l - c}\right)^2\right] \tag{2.5}$$

In the above equations, c is the slippage zone of a natural interface, l is the half length of the opening zone (from $-l$ to $+l$) of natural fracture, μ_f is the friction coefficient of natural fracture, and x_0 is the point where reinitiation will occur. Figure 2.10 shows the slippage zone schematically as described by this criterion.

Although this criterion can determine the slippage on the natural interface, it lacks the capability to predict the new fracture reinitiation on the other side of the natural fracture. It is assumed crossing condition may subsequently occur if no slippage on the natural surface, whereas it is not matching the actual situation in a fracking job. Based on Equation (2.2), the crossing and opening

mode spaces can be graphically present as Figure 2.11. Here, The real tensile strength value of 6.2 MPa from the Bakken field was used for this plot.

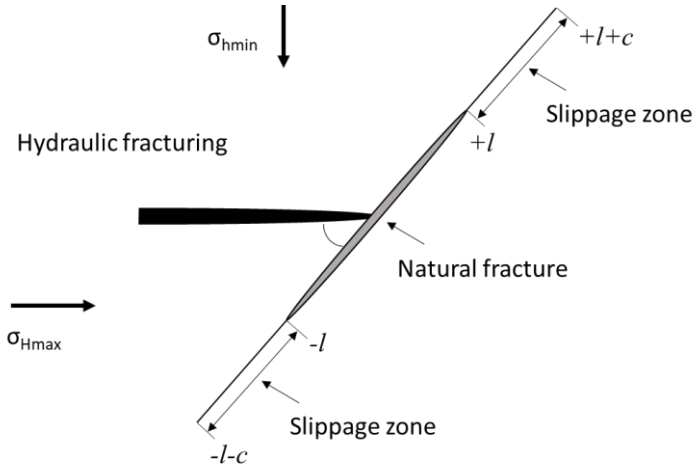

Figure 2.10 Slippage zone of natural fracture based on Blanton's Criterion (Blanton, 1986).

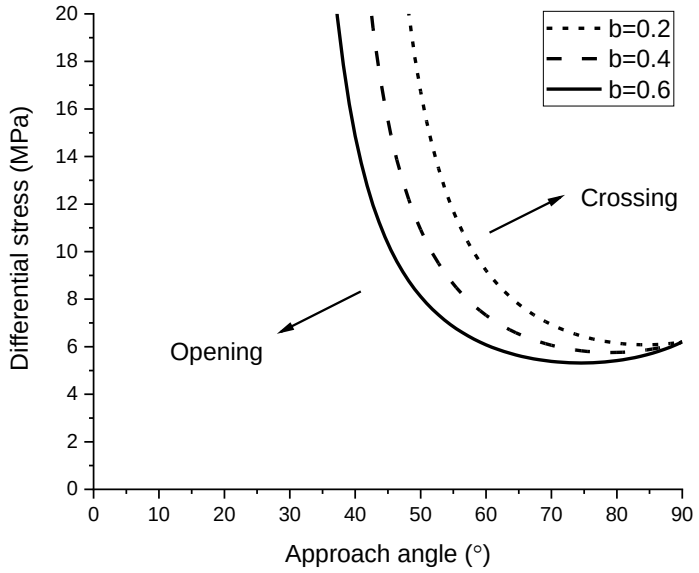

Figure 2.11 Prediction of interaction modes by Blanton's criterion with three different *b* values. The real tensile strength value of 6.2 MPa from the Bakken field was used for this plot.

2.3.2.2 Warpinski and Teufel's Criterion

Warpinski and Teufel (1987) derived their criteria based on the linear friction law and failure analysis of the natural interface (Warpinski & Teufel, 1987). Accordingly, the slippage on the natural interface occurs when:

$$|\tau| = \tau_0 + \mu_f \sigma_n \tag{2.6}$$

Here, σ_n and τ are the normal and shear stresses on the natural interface, respectively, τ_0 is the cohesion of the natural interface and μ_f is the interface friction coefficient.

When the angle of the natural interface with respect to the maximum stress is β, the slippage criteria can be rewritten in terms of the principal stress and the angle of approach as:

$$(\sigma_1 - \sigma_3)\big(sin\,2\beta + \mu_f\, cos\,2\beta\big) - \mu_f(\sigma_1 + \sigma_3 - 2P) = 2\tau_0 \tag{2.7}$$

Dilation of the natural interface will occur if the fluid pressure (p) exceeds:

$$p > \frac{1}{2}(\sigma_1 + \sigma_3) - \frac{1}{2}(\sigma_1 - \sigma_3)\, cos\,2\beta \tag{2.8}$$

When HF propagation is blunted by a natural interface, the singularity of the HF tip disappears, and the net fluid pressure (P_{net}) at the intersection point becomes:

$$P = \sigma_3 + P_{net} \tag{2.9}$$

Substituting Equation (2.9) into Equation (2.7), the critical condition for shearing of the natural interface is stated as:

$$\sigma_1 - \sigma_3 \geq \frac{2\tau_0 - 2p_{net}\mu_f}{sin\,2\beta + \mu_f\, cos\,2\beta - \mu_f} \tag{2.10}$$

Furthermore, the opening criterion can be expressed as:

$$P_{net} \geq \frac{1}{2}(\sigma_1 - \sigma_3)(1 - cos\,2\beta) \tag{2.11}$$

This criterion is generally used to estimate whether a joint is dilated or reactivated due to slippage by a HF. However, it cannot distinguish between the shear and opening mode of the natural interface. Based on Equation (2.10) and (2.11), slippage and opening of natural fracture as functions of stress difference and angle of approach is plotted in Figure 2.8. Solid lines are the thresholds of opening conditions of natural fracture. Above these lines the opening is more prone to happen. It is favorable to crossing while some specific points located below those dash lines whereas the area above dash lines may more likely arresting.

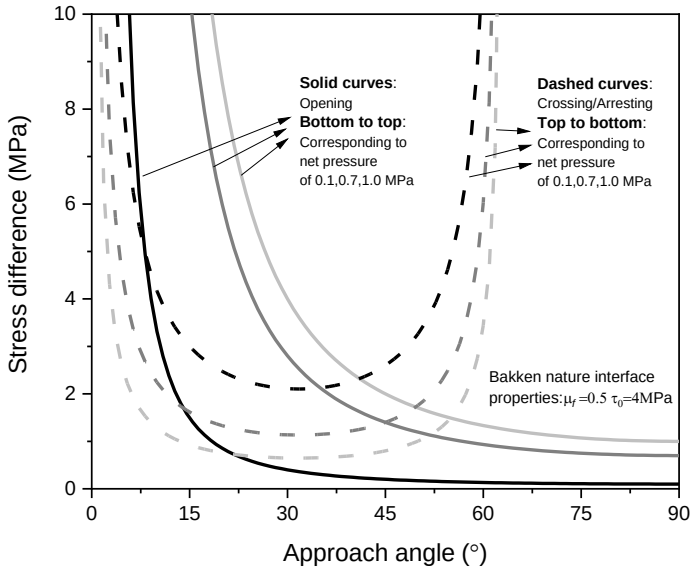

Figure 2.12 Interaction modes determination by W&T criterion with three assuming net pressure and Bakken formation parameters (Sarmadivaleh & Rasouli, 2014).

2.3.2.3 Renshaw and Pollard's Criterion

Renshaw and pollard (1995) presented their criterion based on linear elastic fracture mechanics (Renshaw & Pollard, 1995). This model implies that stresses near the tip can be calculated as:

$$\begin{Bmatrix}\sigma_{xx}\\ \sigma_{yy}\\ \sigma_{xy}\end{Bmatrix} = \begin{Bmatrix}\sigma'_{xx}\\ \sigma'_{yy}\\ \sigma'_{xy}\end{Bmatrix} + \begin{Bmatrix}\sigma^{c}_{xx}(r,\theta)\\ \sigma^{c}_{yy}(r,\theta)\\ \sigma^{c}_{xy}(r,\theta)\end{Bmatrix} = \begin{Bmatrix}\sigma'_{xx}\\ \sigma'_{yy}\\ \sigma'_{xy}\end{Bmatrix} + \left\{\frac{K_I}{\sqrt{r}}\right\} \begin{Bmatrix} cos\frac{\theta}{2}\left[1 - sin\frac{\theta}{2}sin\frac{3\theta}{2}\right] \\ cos\frac{\theta}{2}\left[1 + sin\frac{\theta}{2}sin\frac{3\theta}{2}\right] \\ sin\frac{\theta}{2}cos\frac{\theta}{2}cos\frac{3\theta}{2} \end{Bmatrix} \quad (2.12)$$

where (r, θ) are polar coordinated with the origin at the fracture tip. σ^r_{ij} is the remotely applied stress and K_I is the stress intensity factor for opening. The reinitiation of the fracture on the opposite side of the interface occurs when the induced stresses at the fracture tip exceed the tensile stress of the material, or mathematically when:

$$\sigma_{yy}(max) = T_0 \tag{2.13}$$

Slippage will not occur along the interface if:

$$\left|\sigma_{xy}(max)\right| < -\mu\sigma_{xx}(max) \tag{2.14}$$

Therefore, the crossing occurs when fracture reinitiation on the other side of the interface happens together with the non-slip condition at the interface. The superposition function to determine the interaction modes can be expressed as (Renshaw & Pollard, 1995):

$$\frac{-\sigma'_{xx}}{T_0 - \sigma^r_{yy}} > \frac{0.35 + \frac{0.35}{\mu}}{1.06} \tag{2.15}$$

This criterion assumes that crossing may not occur if the interface slips, however, this contradicts with some observations from experimental studies. A possible explanation may be that this criterion overestimates the reinitiation stress. A limitation of this criterion is that it is applicable when the angle of approach is only 90°.

Table 2.1 Comparison among three classical criteria.

Classical criterion	**Crossing**	**Opening**	**Shear**
Blanton	$P > \sigma_T + T_0$	$\frac{(\sigma_{max} - \sigma_{min})}{T_0} > \frac{-1}{cos\,2\theta - b\,sin\,2\theta}$	-
W&T	-	$P_{net} \geq \frac{1}{2}(\sigma_1 - \sigma_3)(1 - cos\,2\beta)$	$\|\tau\| = \tau_0 + \mu_f\sigma_n$
R&P	$\frac{-\sigma'_{xx}}{T_0 - \sigma^r_{yy}} > \frac{0.35 + \frac{0.35}{\mu}}{1.06}$	-	$\left\|\sigma_{xy}(max)\right\| < -\mu\sigma_{xx}(max)$

2.3.2.4 Modified Models

As mentioned above, the R&P criterion is limited in use to the angle of approach of 90°. Gu (2010) developed a new model including natural fracture properties, which can be applied to non-orthogonal interaction and is presented as (Gu & Weng, 2010):

$$\frac{\frac{S_0}{\mu} - \sigma_H}{T_0 - \sigma_h} > \frac{0.35 + \frac{0.35}{\mu}}{1.06} \tag{2.16}$$

Here, S_0 is the interface cohesion. In case of no cohesion and zero tensile strength for the interface, this criterion reduces to Renshaw and Pollard criteria. However, natural interface cohesion plays an irreplaceable role in the interface shear. Sarmadivaleh (2014) improved the R&P model with an imaginary coefficient of friction to calculate the interface cohesion (Sarmadivaleh et al., 2014). He calculated a general form of interaction criterion corresponding to a cohesive natural fracture intersecting with a non-orthogonal fracture as:

$$\frac{-\sigma_n}{T_0 - \sigma_T} > \frac{\left(1 - sin\frac{\theta}{2} sin\frac{3\theta}{2}\right) + \frac{1}{\mu_f'' \, cos\frac{\theta}{2}}\left(\left|sin\frac{\theta}{2} cos\frac{\theta}{2} cos\frac{3\theta}{2} + \alpha\right|\right)}{\left(1 + sin\frac{\theta}{2} sin\frac{3\theta}{2}\right)} \tag{2.17}$$

In this equation $\mu_f'' = \mu_f + \mu_f'$, and μ_f' can be calculated as:

$$\mu_f' = \frac{\frac{\tau_0}{\sigma_n}}{\left(\frac{1 - sin\frac{\theta}{2} sin\frac{3\theta}{2}}{\left(1 - sin\frac{\theta}{2} sin\frac{3\theta}{2}\right) + \frac{1}{\mu_f \, cos\frac{\theta}{2}}\left|sin\frac{\theta}{2} cos\frac{\theta}{2} cos\frac{3\theta}{2} + \alpha\right|} - 1\right)} \tag{2.18}$$

More realistic representation of the interaction mode requires 3D modeling, considering NFs are fully or partially cemented. Fu (2018) proposed a new model based on linear elastic fracture mechanics to quantitively assess the influence of NF heterogeneity on interaction mode when NF

height coinciding with reservoir height. Crossing may occur when the following three conditions are met (Fu et al., 2018):

Condition 1 – fracture initiation: The maximum stress induced by interaction exceeds the tensile strength of the rock on the other side of the natural interface is favorable to initiate a new fracture:

$$\sigma_{yy}(\theta) + \sigma_{yy}^{r} = T_0, \exists\theta = \theta_{crossing} \in (-90^{\circ}, 90^{\circ}) \tag{2.19}$$

Condition 2 – No tensile failure for the interface: the tensile strength of the natural interface is assumed strong enough to prevent the opening of natural fracture:

$$A_0 > \sigma_{xx}(\theta) + \sigma_{xx}^{r}, \forall\theta \in \left[-\left|\theta_{crossing}\right|, \left|\theta_{crossing}\right|\right] \tag{2.20}$$

Condition 3 – No shear failure for the interface: the shear strength of the natural interface is strong enough to prevent slippage along the natural fracture:

$$C_0 - \mu[\sigma_{xx}(\theta) + \sigma_{xx}^{r}] > \left|\tau_{xy}(\theta) + \tau_{xy}^{r}\right|, \forall\theta \in \left[-\left|\theta_{crossing}\right|, \left|\theta_{crossing}\right|\right] \tag{2.21}$$

2.3.3 Interaction Modes: Experimental Studies

Lab experiments provide great knowledge regarding the physics of the processes happening in the real world. The ability to control and change the parameters affecting the process and run a number of repeatable sensitivity analyses to assess the impact of each parameter on the whole process as well as the ability for visual inspection of the samples after the testing, are the advantages of the lab experiments. However, running representative lab experiments requires a deep understanding of the process and choosing properly scaled parameters to represent the real scale operation.

In order to perform representative HF experiments in the lab, the sample shape should be cubical to allow applying three independent stresses similar to the in-situ stresses. This will enable us to check the propagation direction of the fracture and the impact of the intermediate stress as well as stress anisotropy on fracture geometry. However, the field parameters need to be scaled in order

to propagate the fracture in the same manner as the field. For example, using the field used fluid viscosity and flow rate, in the lab the sample will break in a fraction of a second avoiding tracking the fracture propagation and collecting any data. Therefore, using the existing scaling law, we should change the fluid viscosity and flow rate as well as the wellbore size in order to run the lab experiment in the same propagation mode as in the field. Several scaling laws and dimensionless numbers have been proposed by different researchers, which is not the topic of this thesis (Sarmadivaleh & Rasouli, 2015). In this section, a brief overview of some of the lab experimental HF work done by researchers is presented to highlight the findings.

Zhou (2008) studied the horizontal stress difference and angle of approach on hydraulic fracturing propagation and compared the lab results with the W&T criterion (Zhou et al., 2008). The results are shown in Figure 2.13.

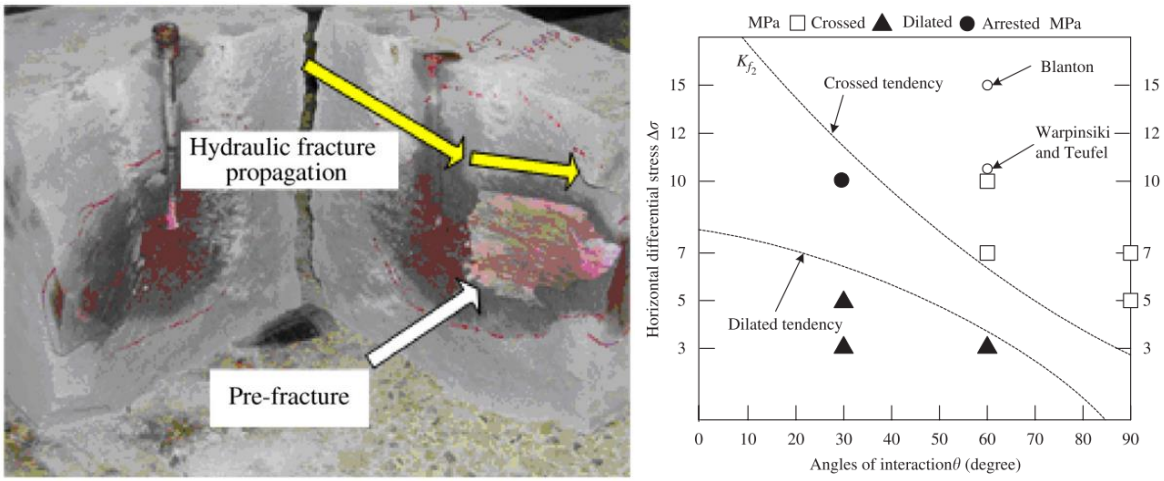

Figure 2.13 Laboratory results showing HF propagation modes in a normal stress regime. W&T was plotted as two tendency lines to separate two dominating interaction modes (Zhou et al., 2008).

Sarmadivaleh & Rasouli (2017) conducted a number of true triaxial testing on cubic samples of 10 cm with two artificially made natural interfaces filled with different bonding materials (Sarmadivaleh, 2012). They investigated the impact of the interface frictional properties as well as the angle of approach on the interaction modes. The results of their findings are shown in Table

2.2. In this Table, the results of Blanton, W&T, and modified R&P criterion are also presented for comparison purposes. In general, they observed good agreements between the experimental data and analytical models.

Table 2.2 Comparison between experimental and analytical results (Sarmadivaleh, 2012).

Sample	Experiment result	Blanton	Modified R&P	W&T 400 psi net pressure	W&T 700 psi net pressure	W&T 1000 psi net pressure
15cmCement90	Crossing	Crossing	Crossing	Crossing	Crossing	Crossing or Opening (marginal)
15cmCement90-2	Arresting	Crossing	Crossing	Crossing	Crossing	Crossing or Opening (marginal)
10cmCement90	Test failure	Crossing	Crossing	Crossing	Crossing	Crossing or Opening (marginal)
10cmCement90-2	Crossing	Crossing	Crossing	Crossing	Crossing	Crossing or Opening (marginal)
10cmCement60	Opening	Crossing	Crossing	Crossing	Crossing	Opening
10cmCement60-2	Crossing	Crossing	Crossing	Crossing	Crossing	Opening
15cmCement60	Arresting + Crossing	Crossing	Crossing	Crossing	Crossing	Opening
15cmCement60-2	Opening	Crossing	Crossing	Crossing	Crossing	Opening
10cmCement30	Opening	Opening	Not Crossing	Arresting or Opening	Arresting or Opening	Arresting or Opening
15cmCement30	Arresting	Opening	Not Crossing	Arresting or Opening	Arresting or Opening	Arresting or Opening
10cmWhite90	Arresting + Crossing	Crossing	Crossing	Crossing	Crossing	Crossing or Opening (marginal)
10cmWhite60	Arresting + Crossing	Crossing	Crossing	Crossing	Crossing	Opening
10cmWhite30*	Arresting + Opening	Opening	Not Crossing	Crossing	Opening	Opening
10cmWhite30-2*	Opening	Opening	Not Crossing	Crossing	Crossing	Opening
10cmBrown90	Arresting + Opening	Crossing	Crossing	Crossing	Crossing	Opening + Arresting (marginal)
10cmBrown60	Arresting + Opening	Crossing	Crossing	Crossing	Crossing	Opening
10cmBrown30*	Opening	Opening	Not Crossing	Arresting or Crossing	Opening or Arresting	Opening or Arresting
10cmBlack90	Opening	Crossing	Crossing	Crossing	Crossing	Opening + Arresting (marginal)
10cmBlack90-2	Arresting + Opening	Crossing	Crossing	Crossing	Crossing	Opening + Arresting (marginal)
10cmBlack60	Arresting	Crossing	Crossing	Crossing	Crossing	Opening
10cmBlack60-2*	Arresting	Crossing	Crossing	Crossing	Crossing	Crossing

Although the lab experiments provide a great insight into the problem, they are time-consuming and costly to perform, difficult to scale the results directly to the field scale and require great

experiences to run them correctly. Therefore, they are mostly used for calibration of numerical modeling, which is easier to perform.

2.3.4 Interaction Modes: Numerical Simulations

Numerical simulation is a widely used approach in many engineering and science disciplines and its application is growing with the new generation of fast speed computers. The numerical modeling can be classified as continuum and discontinuum methods based on their treatment of displacement compatibility. The selection of an appropriate model depends on the problem complexity. Typically, continuum models (such as Finite Element Method, FEM) are used in large-scale problems where the effect of natural fractures is not critical. The discontinuum models (such as Distinct Element Method, DEM) are more applicable to simulate fracture networks and modeling multi-fracturing and fragmentation processes.

In this research, the XSite, a particle-based simulator, will be used for numerical simulation of the interaction modes. Detail explanation of the lattice formulation which is used in XSite and some features of this software will be presented in the next Chapter. In the following subsection, a brief overview of the three commonly used numerical models for HF will be presented.

2.3.4.1 Finite Element Method (FEM)

The Finite Element Method (FEM) is the most widely used method for solving engineering problems, especially in rock mechanics and hydraulic fracturing applications. While this method may not be the best for HF simulations, as it is a continuum model, some researchers have used it for this purpose with some justifications (Mohammadnejad & Khoei, 2013; Wangen, 2013). In order to model hydraulic fracture propagation, a very fine mesh is required to calculate the fracture tip stress intensity factor, as shown in Figure 2.14. Adaptive meshing technique is necessary for

modeling hydraulic fracture propagation to avoid applying very fine mesh for the whole model to improve calculation efficiency (Wong, 2017).

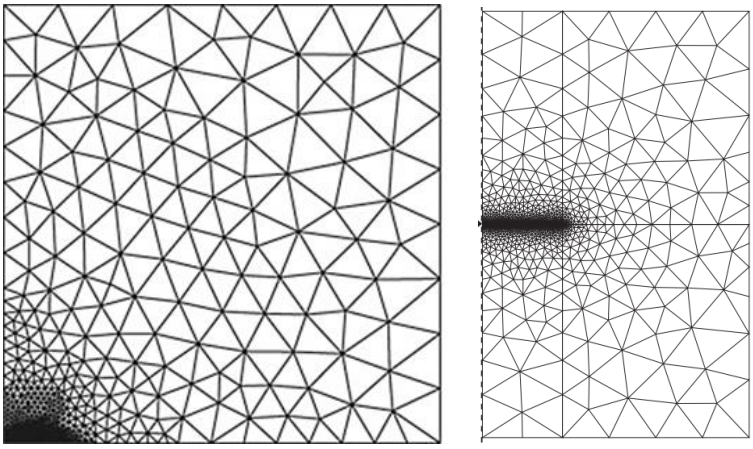

(a) **(b)**

Figure 2.14 Meshes of hydraulic fracturing simulation with FEM. Very fine mesh is required for the modeling of fracture tip for stress intensity factor calculation (Carrier & Granet, 2012; Hunsweek et al., 2006).

The main shortcoming of this method is that the fracture path has to be pre-defined before analysis which is not a realistic approach especially when we simulate the interaction mode.

2.3.4.2 Boundary Element Method (BEM)

The Boundary Element Method (BEM) was proposed by Jaswon (1963) and Symm (1963). BEM has been widely used for solving underground excavation problems. The advantages of the BEM to model fractures were summarized by Liu (Liu et al., 2012):

- Reduction of the dimensions of the problems to be solved, such as from 3D to 2D, from 2D to 1D, leading to easier mesh generation and more efficient calculation.
- Improving the accuracy of calculation on fracture stress concentration problem due to the nature of integrals applied in its calculation.

The main drawback of the BEM is the dense matrix compared to the sparse global stiffness matrix in FEM (Wong, 2017). A dense matrix lowers the efficiency in calculations which restricts the application prospective of BEM.

2.3.4.3 Discrete Element Method (DEM)

Modeling rock as particles were first proposed by Potyondy and Cundall(2004), which is referred to as Bonded Particle Model (BPM) (Potyondy & Cundall, 2004). Several commercial software, such as UDEC and PFC are evolved to solve the discontinue media based on this method. BPM provides no limitations on fracture propagation path and complexity of fracture patterns generated comparing to continuum models. The discontinuity can be modeled explicitly in BPM by the smooth joint model (SJM) (Ivars et al., 2011). Figure 2.15 shows SJM used in BPM, particle may overlap and slip against each other along a specified joint plane to avoid the inherent roughness of the joint. Therefore, it can be inserted into models to investigate the interaction between hydraulic fracture and pre-existing fractures.

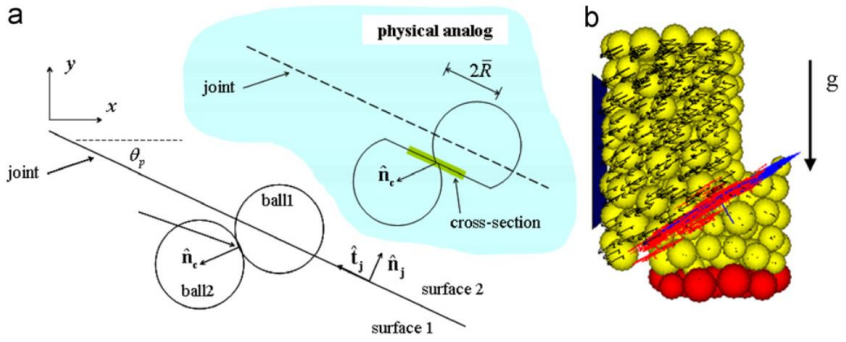

Figure 2.15 (a) Effective joint geometry and (b) 3D specimen with frictionless through-going joint loaded by gravity (Ivars et al., 2011).

Hassan (2017) conducted a numerical simulation based on DEM to investigate the interaction of natural fracture and propagated hydraulic fracture (Fatahi et al., 2017). The simulation results were validated through pre-finished experimental studies from Figure 2.16. Both of experimental and

numerical simulations showed that increasing the approaching angle between hydraulic fracture and natural fracture can increase the likelihood of crossing. In contrast, it is more likely to have the HF be arrested by the natural fracture at low interaction angles. The high agreement of BPM modeling and experimental results proved the reliability of this method.

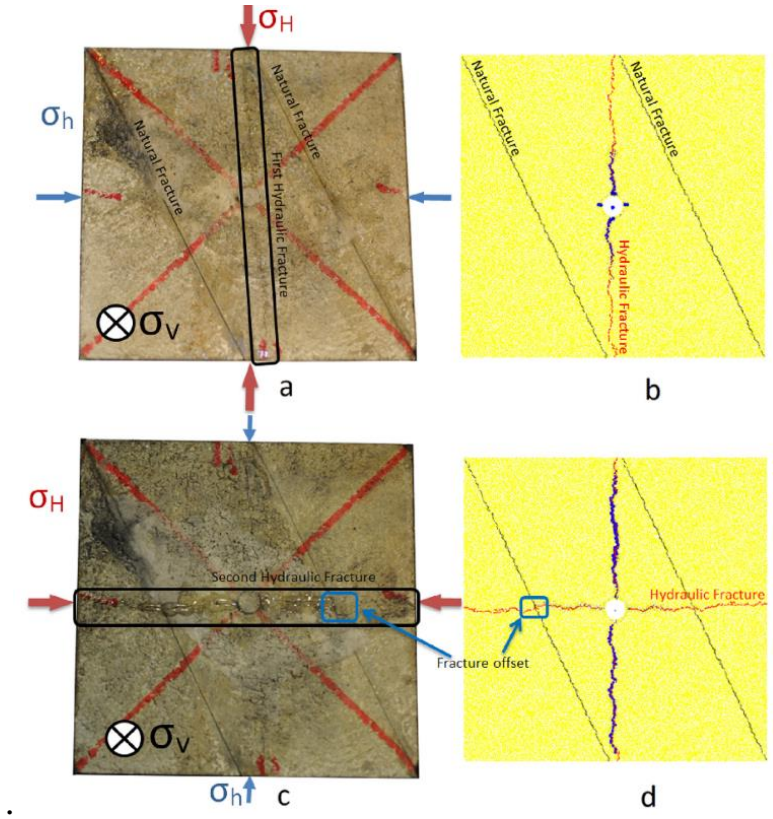

Figure 2.16 Comparison between experimental and PBM numerical simulation results (Fatahi et al., 2017).

2.4 HF Propagation in Laminated Reservoirs

In recent years, a large number of researchers have used numerical simulation, lab experiments, and theoretical analysis to investigate the HF extension pattern in laminated reservoirs (Lecampion & Desroches, 2015; Simonson et al., 1978; Tan et al., 2017). Due to the sedimentation process, the reservoirs and the over and underlying formations are formed in a laminated form, which is known as a transversely isotropic medium. In general, the sediments are horizontal layers with the

axis of symmetry being perpendicular to the lamination. Therefore, they are referred to as vertical TI medium (VTI or TIV). Figure 2.17 shows an example of fracture propagation from a stiff layer to another one, penetrating through a soft layer in between. Based on several published works, it is well known that the fracture geometry in laminated formations is a function of stress anisotropy, the contrast between the mechanical properties of the reservoir formation and caprocks, and to some extent, the operational aspects, such as the injection rate and fluid properties (Dou et al., 2019; Li et al., 2017). Understanding HF propagation in laminated reservoirs is important to predict the fracture geometry for the treatment design accurately.

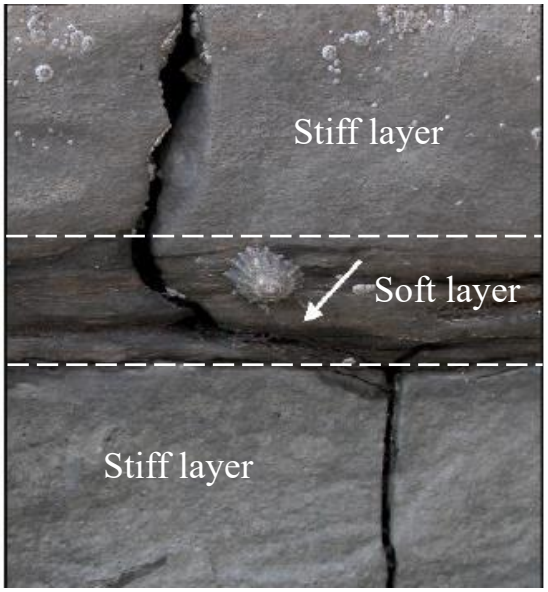

Figure 2.17 Hydraulic fracture propagation in the alternation of stiff and soft layers (Afsar, 2014).

The investigation of hydraulic fracturing propagation mode from a variety of perspectives, including formation properties and the mechanisms of interaction between HF and the interface. Based on the lab experiments and field data, some researchers concluded that the contrast in the mechanical properties of adjacent layers primarily determines the fracture height growth (Simonson et al., 1978). They outlined that HF would be contained if the stiffness of the pay zone were less than that of the adjacent caprock layers; otherwise, fracture penetration would occur.

However, some scholars claimed that the fracture containment was not only ascribed to stiffness between layers but also interface properties and interlayer stress difference (A. A. Daneshy, 2007; Hongren Gu & Siebrits, 2005; Smith et al., 2001; Teufel & Clark, 1984; Norman R. Warpinski et al., 1982). In addition, the interfacial shear strength and the angle of approach between HF and natural interface may play an important role in HF containment. Essentially, the effect of the angle of approach is also realized by affecting the shear strength of the interface. Some lab experiments performed to study the influence of interfacial shear strength effect on HF interactions with natural fractures showed a strong interface reduces the possibility of interfacial slippage but benefits the HF penetration (Sarmadivaleh, 2012; Sarmadivaleh & Rasouli, 2015;).

Although many studies have been done on the vertical extension of HFs in laminated reservoirs under the influence of barriers, most of these numerical models are simplified two-dimensional models and cannot simulate the fracture propagation under the influence of multiple bedding and barriers in three-dimension. The discrete element method (DEM), developed by Cundall (1971), is widely used to solve deformation, damage, fracture, and stability problems in a fractured rock mass (Eberhardt et al., 2004; Kang et al., 2018). Fracture extension in DEM is usually limited to a pre-defined geometric region. Mas et al. (2011) developed the Synthetic Rock Mass (SRM) method to overcome this limitation, which uses a bonded particle model to represent intact material and the Smooth Joint Model (SJM) to represent pre-existing joints or interfaces. XSite, an SRM-based 3D lattice model simulation method capable of simulating tension, shear damage, and slippage of hydraulic and natural fractures with higher computational efficiency than methods such as PFC, DEM, and XFEM, has recently been used in the industry to simulate HF geometry will be used in this research (Damjanac et al., 2013).

2.5 Summary

This Chapter presented a summary of the literature review with respect to the hydraulic fracture propagation, interaction modes with natural fractures, HF evolution in a laminated reservoir and the main parameters impacting the type of evolution. It was mentioned that the stress state, rock properties, and fluid parameters are the main elements required for consideration while operating fracture treatment. Also, a brief overview of the analytical models, lab experimental work, and numerical simulations to study the interaction modes were presented. It was also discussed that the previous studies about the hydraulic fracture geometry in the laminated reservoir from the perspective of experimental studies and numerical simulations.

In the next Chapter, a lattice-based predictive model for the interaction mode of hydraulic fracture with natural fractures will be presented.

Chapter 3

Interaction Modes between Hydraulic Fracture and Natural Fractures

3.1 Introduction

In this chapter, the lattice-based model was used to simulate the hydraulic fracture propagation and its interactions with natural fractures, considering the effects of varying natural fractures properties, injection parameters, and formation mechanical properties. Ideally, the hydraulic fracture is expected to communicate the existing natural fracture networks, known as sweet spots in tight formations, in order to create a continuous path for the flow to the lateral section of the wellbore. However, the interaction of the hydraulic fracture with the natural fracture is complex and may result in different mechanisms (modes) known as crossing, arresting, and opening. The formation properties, the state of the in-situ stresses, frictional properties of the natural interface, and the injection fluid properties all affect the interaction mechanism to some extent. Therefore, one of the challenges that hinder the improvement of production, is the prediction of hydraulic fracture propagation mode during the period of the hydraulic fracturing operation. In this study, we use the log-log plot of the bottom hole pressure versus time after fracture breakdown and during the fracture propagation stage to investigate the interaction modes. XSite, a lattice-based simulator, is used to model the interaction mechanism. A number of simulations were performed using the

Bakken Shale data in North Dakota with a wide range of input parameters to study the impact of the input parameters on the interaction mode. The results formed a database that was used to develop a predictive model to determine the interaction mode.

3.2 Fracture Propagation Diagnostic

The bottom hole pressure diagnostic approach has been proposed for predicting hydraulic fracture propagation during the fluid injection phase. Four typical propagation modes with the log-log plot can be interpreted as depicted in Figure 3.1 (Economides & Nolte, 2000). Type 1 plot indicates the increasing net pressure as the fracture propagates in the confined height formation. Type 2 plot is a constant pressure plateau that can result from unstable growth or fluid loss. Type 3 represents the restricted propagation of hydraulic fracturing. Type 4 shows the fracture crossing a barrier and encountering a lower stress zone.

From Figure 3.1, it is seen that Types 3 and 4 represent examples of the interaction modes between hydraulic fracture and natural fractures (NF), or, in general, natural interfaces (NI). The idea in this study is to expand on this approach and look at the change of the slope of the pressure-time plot during fracture propagation to diagnose different cases of interaction modes.

The opening of NF is due to either the dilation during slip or fluid pressure overcoming the normal stress acting on the NF plane. Under opening condition, sufficient pressure should be generated to overcome the in-situ normal traction on the NF plane. As long as the NF is not parallel to the maximum stress direction, the traction on the NF plane will be a restriction for opening, which leads to a relatively high slope in the log-log plot (type 3). The crossing of natural fractures can be plotted by type 4 or modified type 3, which depends on the natural fracture frictional properties. The crossing only happens when NF is strong enough to avoid slippage and the maximum stress

acting on the fracture tip reaches the rock tensile strength on the opposite side of the interface. If the natural fracture is cemented, there are no noticeable changes in bottom hole pressure. However, when the natural fracture is not cemented, the crossing requires a pressurization process of injecting fluid to initiate a hydraulic fracture on the other side of the natural fracture. In this condition, the crossing can be plotted similar to type 3.

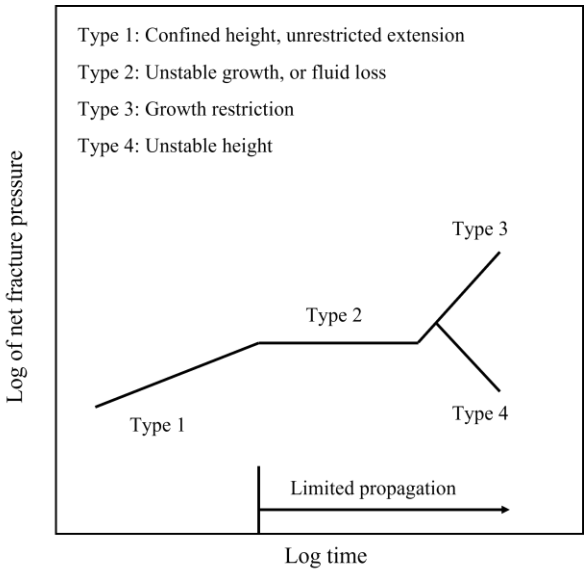

Figure 3.1 Schematic of net fracture pressure indicating the progress of fracture propagation (Economides & Nolte, 2000).

Table 3.1 Interpretation of log-log plot of fracture pressure slopes (Economides & Nolte, 2000).

Propagation Type	Log-Log Slope	Interpretation
Type 1	1/6 to 1/4	PKN
Type 2	0	Unstable growth (height growth) Fluid loss T-shaped fracture
Type 3	>=1	Growth restriction
Type 4	<0	Uncontrolled height growth

We define the interaction pressurization rate index (IPRI) as the slope of the log(p)-log(t) during the fracture propagation phase to quantify the fracture pressurization. When the induced fracture extends within an intact rock, the fluid pressure can maintain the fracture opening as long as it overcomes the magnitude of the minimum principal stress. So, a small IPRI is enough for maintaining the fracture open, like the Type 1 in Figure 3.1. However, when HF intersects a NF, regardless of the mode of interaction, the fluid pressure inevitably undergoes a pressurization process to accumulate enough energy to propagate along the natural fracture or initiate a new fracture on the other side of the natural fracture. This is depicted schematically in Figure 3.2. The IPRI is sensitive to the interlocking changes of the NF properties, the energy of HF itself, formation properties, and the state of stresses.

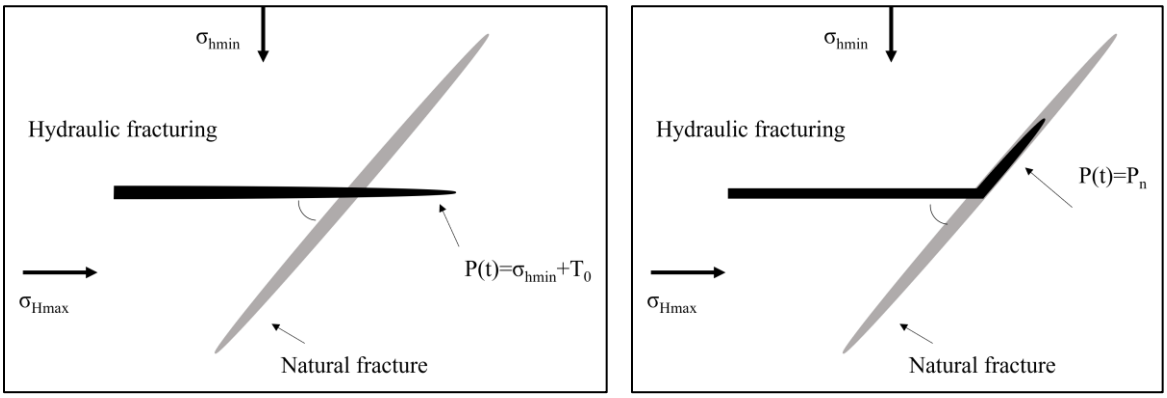

(a) **(b)**

Figure 3.2 Hydraulic fracture interaction mode: (a) crossing, and (b) fracture opening.

3.3 XSite Lattice Formulation

The XSite lattice simulator, which was used in this study for simulation purposes, was developed by the Itasca Consulting Group based on the application of synthetic rock mass (SRM) (Damjanac & Cundall, 2016). It is able to simulate the interaction between the HF and NI without predefining

propagation path and mechanism of interaction. In the simulator, the propagation of the fracture in the rock is simulated by lattice, while the pre-existing joints are presented by the smooth joint model (SJM).

3.3.1 Mechanical Model

The rock mass in the simulator is represented by randomly distributed lattice nodes connected by normal and shear springs. The following central difference formulas of linear momentum equilibrium and displacement-velocity relation are used for each node (Damjanac & Cundall, 2016) to simulated the translational motion of each node

$$\dot{u}_i^{(t+\Delta t/2)} = \dot{u}_i^{(t-\Delta t/2)} + \sum F_i^{(t)}\,\Delta t/m \tag{3.1}$$

$$u_i^{(t+\Delta t)} = u_i^{(t)} + \dot{u}_i^{(t+\Delta t/2)}\Delta t \tag{3.2}$$

where $\dot{u}_i^{(t)}$and $u_i^{(t)}$are the velocity and position of component i (i=1, 3) at time t, $\sum F_i$ is the sum of all force-components acting on mass within the time step of Δt. Likewise, the angular velocities, ω_i, of component can be calculated as:

$$\omega_i^{(t+\Delta t/2)} = \omega_i^{(t-\Delta t/2)} + \frac{\sum M_i^{(t)}}{I}\Delta t \tag{3.3}$$

where $\sum M_i$ is the sum of all moment-components acting on the node of moment of inertia I. The relative displacement and spring force variations are determined using the node velocities as:

$$F^N \leftarrow F^N + \dot{u}^N k^N \Delta t \tag{3.4}$$

$$F_i^S \leftarrow F_i^S + \dot{u}_i^S k^S \Delta t \tag{3.5}$$

Here, "N" denotes "Normal", "S" denotes "shear"; k^N and k^S are the spring normal and shear stiffnesses, respectively. An unbonded joint's sliding and opening behavior are modeled on the joint plane following the relationships.

$$If\ F^n - pA < 0, then\ F^n = 0, F_i^S = 0; else, F_i^S \leftarrow \frac{F_i^S}{\left|F_i^S\right|} min\{(F^n - pA)tan\emptyset, \left|F_i^S\right|\} \quad (3.6)$$

$$If\ F^n - pA + \sigma_c A < 0\ or\ \left|F_i^S\right| > \tau_c A \quad (3.7)$$

where F^n is the normal force (compression positive), F_i^S is the shear force vector, p is the fluid pressure, A is the apparent area of the joint segment, and $\emptyset$ is the interface friction angle.

3.3.2 Flow Model

Transient fluid flow is simulated within both the intact rock matrix and the joints. To account for the permeability, fluid storage and leak-off, the rock matrix flow utilizes pore pressures contained in the matrix springs. The flow in the joints, including pre-existing joints and newly formed fractures, is modelled on a network of pipe-connected fluid nodes (one-dimensional flow elements). During hydraulic fracture propagation, the XSite code automatically generates pipe-connected fluid elements when springs break, or predefined joints are intersected. New pipes are created and linked continuously, forming complex fracture network systems. Lubrication equation is used to approximate the flow in a fracture. This flow from node A to node B along the pipe can be calculated as (Damjanac & Cundall, 2016):

$$q = \beta k_r \frac{a^3}{12\mu_f}[P^A - P^B + \rho_w g(Z^A - Z^B)] \quad (3.8)$$

Here, a is hydraulic aperture. M_f is viscosity of the fluid, P^A and P^B are fluid pressures at node "*A*" and "*B*", respectively. Z represents elevations of nodes, ρ_w is fluid density, and g is the acceleration due to gravity. Meanwhile, k_r is the relative permeability, and β is a dimensionless calibrated parameter, which is a calibrated function of model resolution (Damjanac et al., 2016).

3.3.3 Flow Mechanical Coupling

In XSite, hydraulic fracture propagation is simulated as fully coupled mechanical processes and fluid flow. The permeability of the fracture is controlled by the fracture aperture and the

deformation mechanism of the model. The deformation and damage of the mechanical model are calculated based on the change in fluid pressure. Conversely, the fluid pressure varies with the deformation (Damjanac & Cundall, 2016).

3.4 Model Setup and Validation

3.4.1 Model Setup

A field-scale model was built in XSite to study hydraulic fracture propagation and its interaction with natural fractures. The data corresponding to the Bakken Shale formation in North Dakota, USA, as listed in Table 3.2 were used for the simulation purposes (Ling & Zeng, 2013). Figure 3.3 shows the 3D model geometry with dimensions. The length (along the Y-axis), width (along the X-axis), and height (along the Z-axis) of the model are 350m, 300 m, and 50m, respectively. The fracture is initiated from the middle of a horizontal wellbore which is drilled along X direction, i.e., the direction of minimum horizontal stress (σ_h). The spherical cluster at this point is the point of fracturing fluid injection and the small starter crack is placed perpendicular to σ_h in order to facilitate the initiation of the induced fracture. The magnitude of the principal stresses is shown in Table 3.1. However, here we use the reduced stress values while the stress differences kept constants, i.e., σ_h=4MPa, σ_H =10.8MPa, and σ_v =17.6 MPa, in X, Y, and Z directions, respectively. This is to speed up the calculations, while the differential stress which is the key in HF modeling is kept the same. Two vertical NFs parallel to the wellbore direction are placed symmetrically at 70m distance on both sides of the wellbore. Slick water was selected as the fracturing fluid and injected at a rate of 0.08 m^3/s (30 bbl/min). In simulations, the Voronoi tessellation model was implemented. In XSite, the model is run for about 0.1s for mechanical equilibrium before the step with fracturing fluid injection starts.

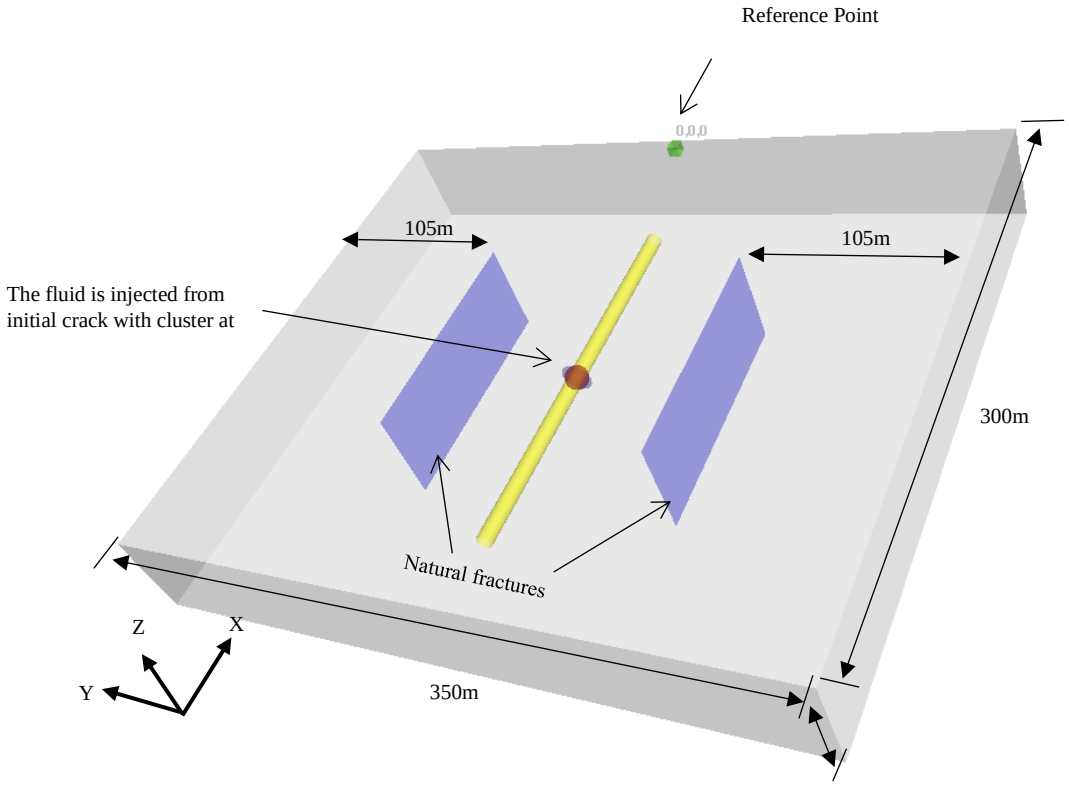

Figure 3.3 The model geometry in XSite simulations.

Table 3.2 The hydro-mechanical properties of the Bakken formation used for XSite simulations.

Hydro-mechanical property	Value
Maximum Horizontal stress, σ_H, psi (MPa)	1566 (10.8)
Minimum Horizontal stress, σ_h, psi (MPa)	580 (4)
Vertical stress, σ_v, psi (MPa)	2553 (17.6)
Uni-axial compressive strength, UCS, psi (MPa)	7251 (50)
Uni-axial Poisson's ratio, ν	0.25
Young's modulus, E, Mpsi (Gpa)	8.702 (60)
Internal friction angle, ϕ (°)	30
Tensile strength, T_0, psi (MPa)	725 (5)
Fracture toughness, K_{IC}, psi(in)$^{0.5}$ (MPa(m)$^{0.5}$)	1820.1 (2)
Porosity, ϕ (%)	2
Permeability, K(m^2)	9.869×10^{-14}

3.4.2 Numerical Simulation versus Analytical Solutions

Here, the results of the interaction mode of the model presented in the previous section are presented. The results of the numerical simulation will be compared with the two classical

analytical criteria of Blanton (1986) and Renshaw and Pollard, R&P, (1995), or the more generalized criteria of Gu and Weng (Gu & Weng, 2010).

Blanton interaction criteria is defined as (Blanton, 1986):

$$\frac{(\sigma_H - \sigma_h)}{T_0} > \frac{-1}{cos\,2\theta - b\,sin\,2\theta} \tag{3.9}$$

where σ_H and σ_h are principal stresses of formation, θ is the angle of approach between hydraulic fracture and natural fracture, T_0 is the rock's tensile strength, and b is a complex coefficient regarding the frictional coefficient of the NF, the length of the slippage zone on NF, and the position of the point at which interaction will take place. This criterion distinguishes the opening from the crossing mode as a function of the differential stress and the angle of approach.

In Figure 3.4 the Blanton criteria envelop is plotted for b=0.6. The friction coefficient of the NF in this example is 0.4. The area to the right of the envelop shown in this figure corresponds to the crossing mode, whereas the area to the left of the envelop presents the opening mode. In this plot, also the results of XSite numerical simulation are presented at angle of approaches from 30° to 90° and for two differential stresses of 6.9 MPa and 10.3 MPa, respectively. The results show good agreements between the numerical simulations and Blanton Criteria, except for slight overprediction of opening mode at 60° angle of approach.

R&P criterion is an orthogonal case of the Gu and Weng criterion (Renshaw & Pollard, 1995), so here, we compare the numerical simulation results with Gu and Weng criterion. The criterion defined as:

$$\frac{\frac{S_0}{\mu} - \sigma_H}{T_0 - \sigma_h} > \frac{0.35 + \frac{0.35}{\mu}}{1.06} \tag{3.10}$$

Here, S_0 is the interface cohesion, and μ is the interface friction coefficient.

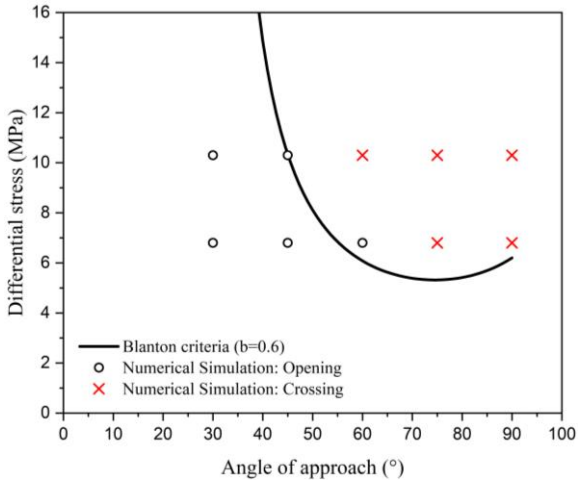

Figure 3.4 Numerical simulation versus Blanton's criterion for interaction mode prediction.

The results of the Gu and Wang criteria corresponding to the Bakken data for different stress ratios as function of friction coefficient are plotted with respect to different angles of approach in Figure 3.5(a). Here, we considered the tensile strength of the rock to be 5 MPa to be consistent with the results of the numerical simulations. In Figure 3.5(b) the results of numerical simulations at an angle of approach of 75° are compared with the Gu and Wang envelop. Total of 16 numerical simulation cases were run and plotted in this figure. Good agreement is observed between the results of the two methods in this example.

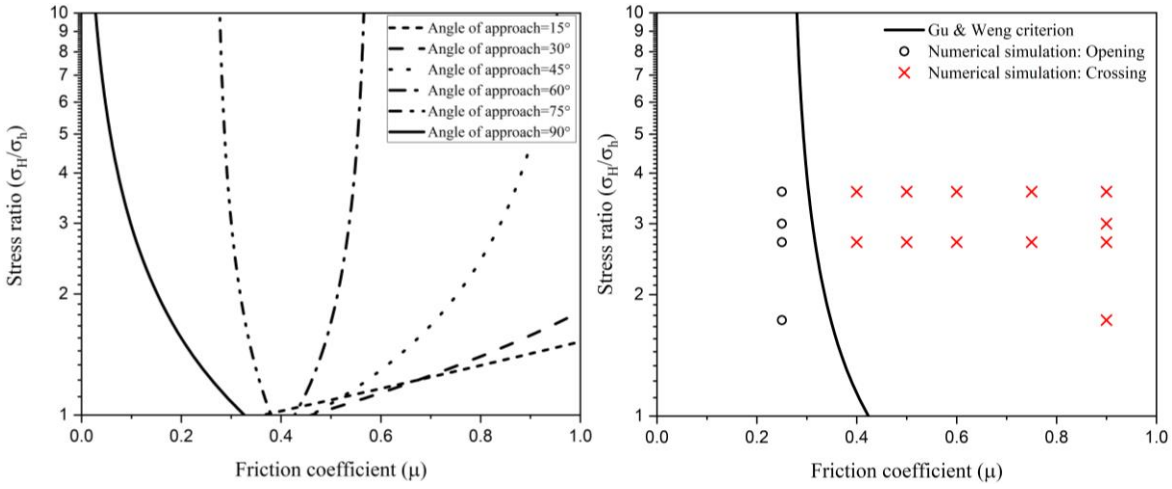

(a) **(b)**

Figure 3.5 (a) Gu and Wang (2010) interaction mode envelop for Bakken data and, (b) comparison with numerical simulation results.

3.5 Numerical Stimulations

In order to investigate the impact of the NFs on the propagation of a HF, we first build a model without any NFs and use the log(p)-log(t) corresponding to this case as the base model for comparison purposes. After that, a number of models will be simulated to analyze the effects of the angle of approach, friction coefficient, stress state, and fracturing fluid viscosity on IPRI and analyze the relationship between IPRI and interaction mechanisms.

3.5.1 Base Model

Here, we simulate a PKN HF model propagating in an intact rock. In this model, it is assumed that the fracture height is constant (e.g. contained within a reservoir layer) and the length of the fracture is much larger than its height (Martins, 1989). Figure 3.6 shows an example of the PKN XSite simulation considering the Bakken data. The plot represents the aperture of the fracture at a certain time of the simulation. It is seen that the fracture has propagated as a straight plane perpendicular to the direction of σ_h, as a result of relatively large stress anisotropy in the horizontal plane. Corresponding pressure-time plots for this model are presented in Figure 3.7 in both normal and log-log space. It is observed that the slope of the pressure curve during the propagation phase is on average 0.197. This value falls within the expected range for a PKN model reported in Table 3.1 (i.e., 1/6~1/4). This base model is used for later comparison with cases where HF intersects NFs.

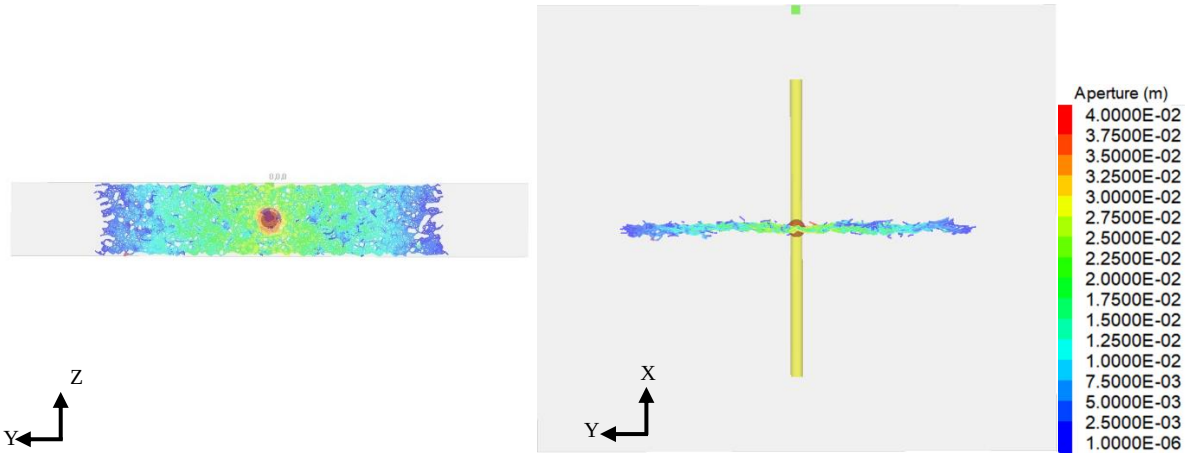

(a) **(b)**

Figure 3.6 PKN hydraulic fracture simulation: (a) front view, (b) top view.

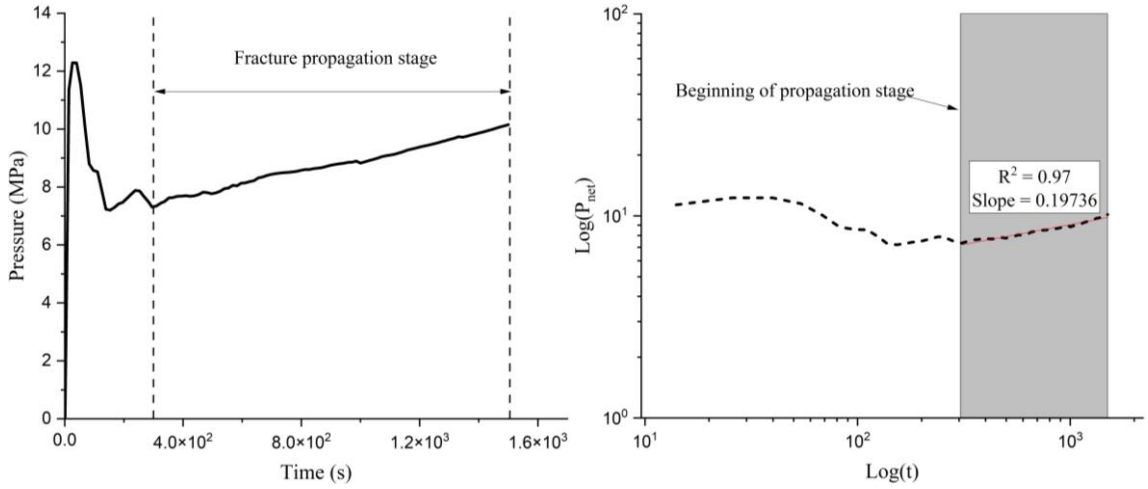

(a) **(b)**

Figure 3.7 PKN hydraulic fracture pressures: (a) pressure-time plot, (b) log-log plot.

3.5.2 Interaction Modes

Opening, partial crossing, and crossing are the three typical interaction modes. For demonstration purposes, here, we present the simulation results corresponding to opening and crossing interaction modes in Figures 3.8 to 3.12, respectively. The only parameter that has been changed in these three models resulting in different interaction mechanisms is the angle of approach between the HF and NFs. As it is seen from these figures, the pressure corresponding to the propagation phase can be

divided into two stages, before and after the time when the HF intersects the NFs. In general, before a HF hits a NF, the propagation continues at a steady state. At the time of the intersection, the pressure response depends on the characteristics of the NF. If the NF is relatively permeable insitu, the pressure may experience a sudden drop, whereas, in relatively impermeable or nearly cemented NFs, the pressure starts to build up immediately. In either case, the changes in the fluid pressure are recorded from the moment of intersection and the average slope is reported as the IPRI.

The IPRI values corresponding to Figures 3.8 to 3.10 are 0.485, 0.527, and 0.819, respectively. The trend of the results illustrates that IPRI monotonically increases with the angle of approach. The IPRI values in Figure 3.11 and 3.12 are 1.237 and 1.029, indicating that opening has relatively larger values compared to crossing in large angle of approach. These represent the IPRI value with angle of approach in opening and crossing interaction modes. The interpretation of the results is given in the following sections where the sensitivity analyses of the input parameters are performed.

The results of experimental and analytical models suggest that the crossing mode is more likely to happen in presence of large angle of approaches (i.e., 90°), high interface friction, high fluid viscosity and flow rate, and high differential stresses.

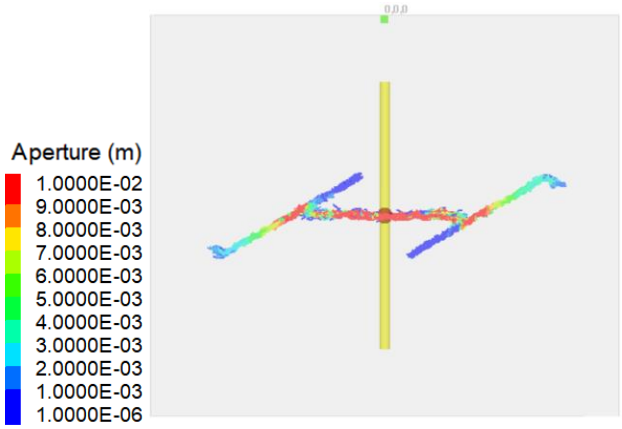

(a)

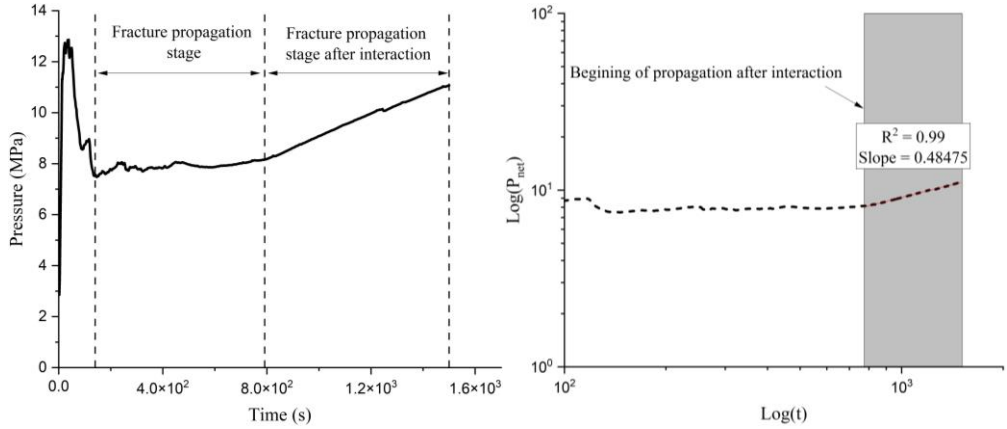

(b) **(c)**

Figure 3.8 Opening mode when angle of approach is 30°: (a) model geometry, (b) pressure-time plot, (c) log(p)-log(t) plot.

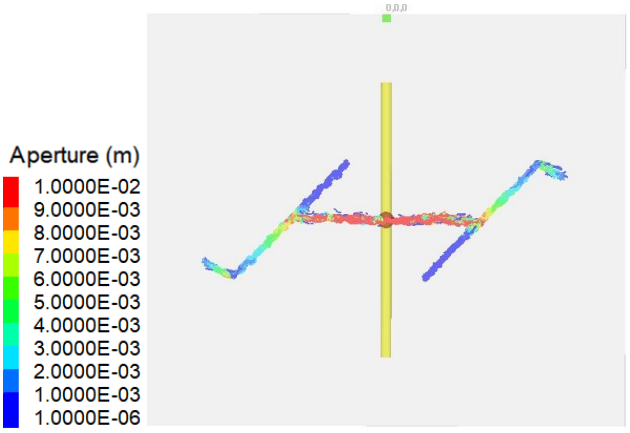

(a)

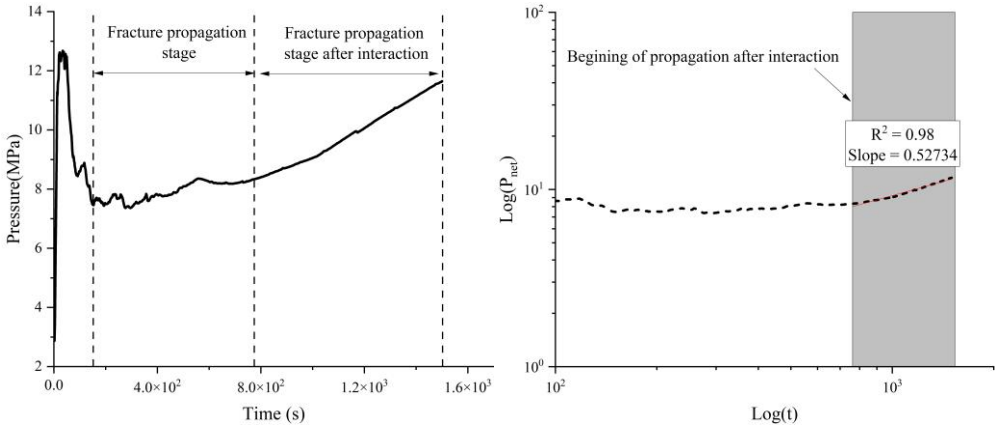

(b) **(c)**

Figure 3.9 Opening mode when angle of approach is 45°: (a) model geometry, (b) pressure-time plot, (c) log(p)-log(t) plot.

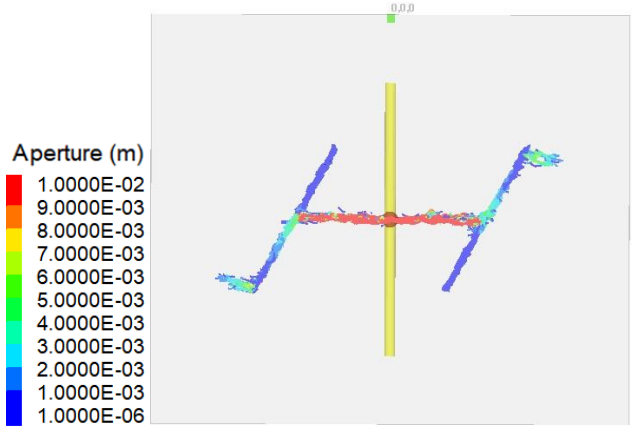

(a)

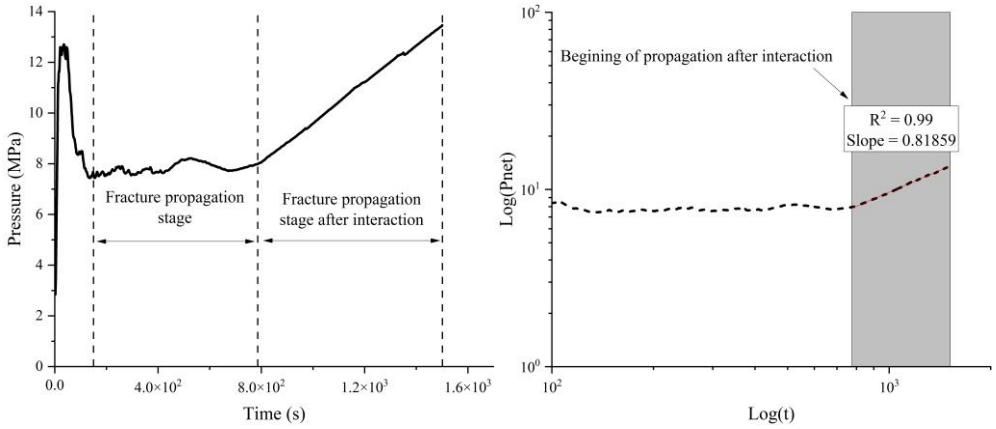

(b) **(c)**

Figure 3.10 Opening mode when angle of approach is 60°: (a) model geometry, (b) pressure-time plot, (c) log(p)-log(t) plot.

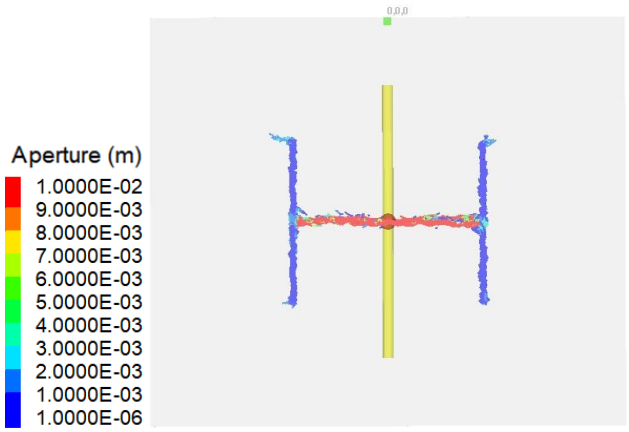

(a)

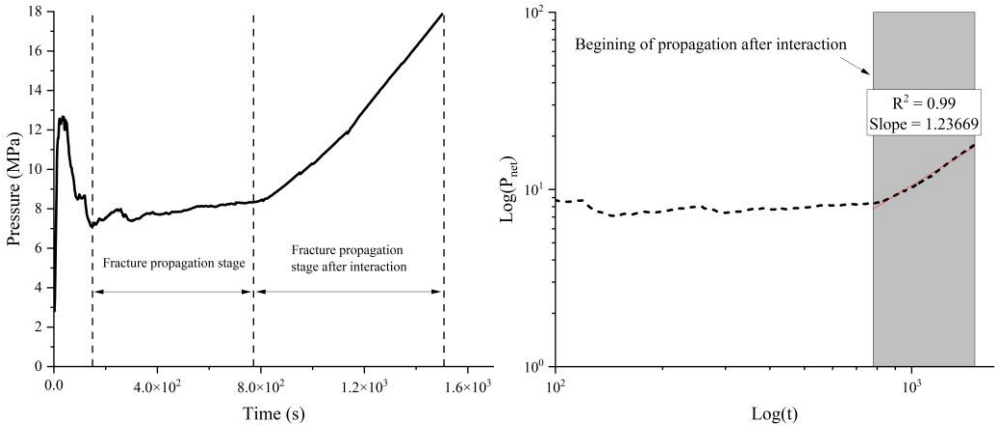

(b) **(c)**

Figure 3.11 Opening mode when angle of approach is 90°: (a) model geometry, (b) pressure-time plot, (c) log(p)-log(t) plot.

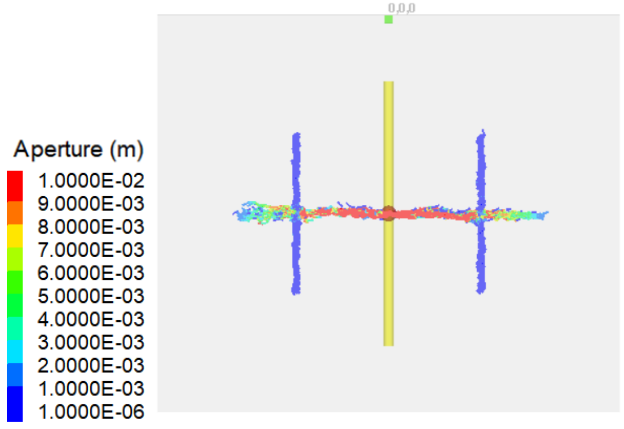

(a)

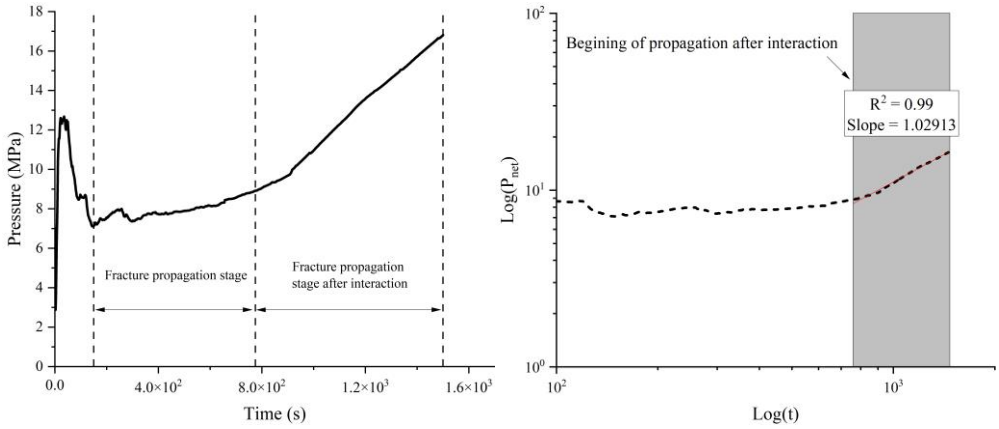

(b) **(c)**

Figure 3.12 Crossing mode when angle of approach is 90°: (a) model geometry, (b) pressure-time plot, (c) log(p)-log(t) plot.

3.5.2.1 Effect of the Angle of Approach and Interface Friction

Several simulations were performed using the Bakken data, where the angle of approaches was changed from 30° to 90°, and the interface friction coefficient were varied from 0.25 to 0.9. The simulation results of the interaction modes are shown in Figure 3.13 as the angle of approach versus the coefficient of friction of the NF. In this figure, the opening and crossing modes are illustrated as blue and black dots, respectively. At the low angle of approaches (mainly below 60°), HF tends to shear and reactivate the NF plane and result in opening mode. In contrast, at high angle of approaches (above 60°) the crossing mode dominates. Similarly, opening and crossing modes are observed at low and high interface friction, respectively. For cases with low interface friction (below 0.4), even at high angle of approaches near 90°, the HF is unable to cross the NF due to the weak shear resistance of the NF which makes it more prone to the slippage. The red dashed curve in Figure 3.13 defines the transition from the crossing to the opening mode in this example. It is seen that the partial crossing cases are clustered around this transition curve.

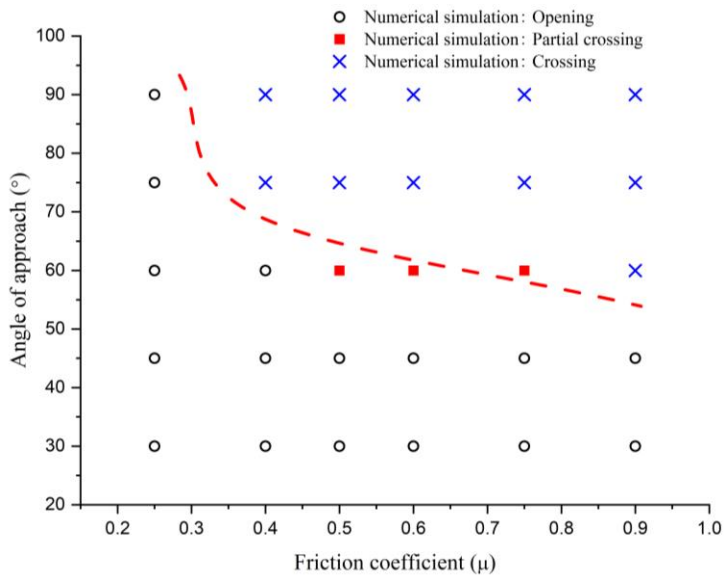

Figure 3.13 Influence of angle of approach and interface friction on hydraulic fracture interaction modes.

The influence of the angle of approach and the interface friction on IPRI is shown in Figure 3.14. In general, the results illustrate that crossing probability increases with the larger IPRIs. A noticeable increment in IPRI is observed when the angle of approach exceeds 60°. Increasing the angle of approach while keeping other parameters constant increases the normal stress on the NF surface requiring more energy to open the fracture surface, hence opening consistently have greater IPRI with greater value for greater angle. The results also show a relatively stable IPRIs for crossing cases regardless of the magnitude of the friction coefficient and the angle of approach. This observation may suggest that when the NF interface does not satisfy the slip condition, only a fraction of additional energy is required to initiate a new fracture on the other side of the natural interface.

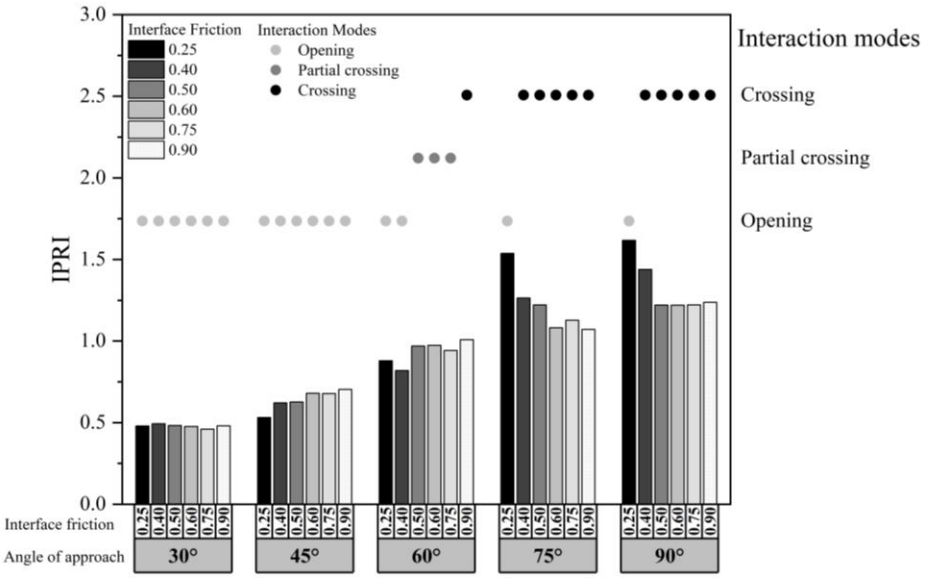

Figure 3.14 Influence of the angle of approach and interface friction on IPRI.

3.5.2.2 Effect of Differential Stress

Simulations were done for different horizontal stress anisotropy. To do this, we kept the value of σ_h constant and changed the magnitude of σ_H. Simulations with differential stresses of 2.93, 6.8, 8.03, and 10.3 MPa were carried out. In Figure 3.15, as an example, the results corresponding to differential stress of 10.3MPa are presented. The red dashed curve in this figure is the envelop showing the transition from crossing to the opening mode. From this figure, more crossing modes are observed compared to black dashed curve, which is from Figure 3.13, showing that the effect of stress anisotropy is more manifest than those of the friction coefficient and the angle of approach.

Figures 3.16 and 3.17 show the impact of the differential stress on IPRI corresponding to the friction coefficients of 0.25 and 0.9, respectively. The results show that in case of low friction coefficients (Figure 3.16) the opening is the dominant interaction mode as the fracture has less ability to resist the interface slippage and the values of the IPRI show a slightly ascent with the increasing the differential stresses. However, in this case, the angle of approach greatly affects the IPRI when the differential stress change, which is due to the fact that changing the angle of

approach will change the normal stress acting on the natural interface. For the case of friction coefficient of 0.9 (Figure 3.17) the results show all three interaction modes, while larger angle of approaches and friction coefficients tend to dominate the crossing mode.

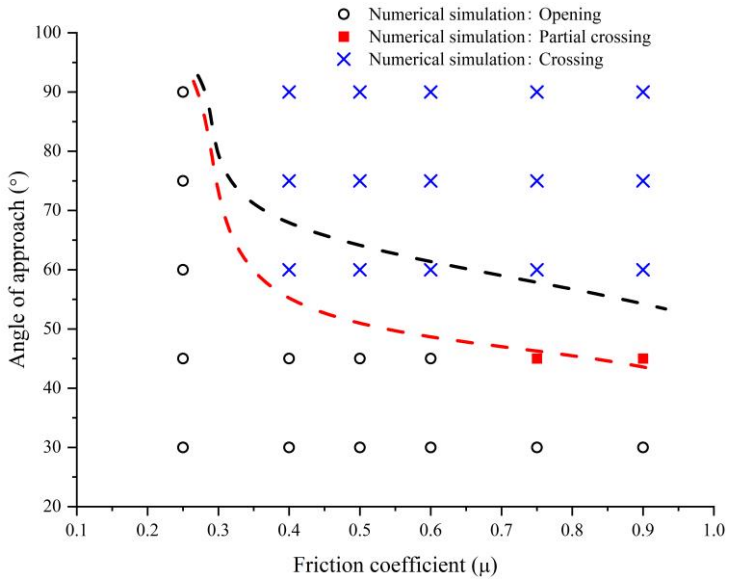

Figure 3.15 Simulation results corresponding to differential stresses of 10.3 MPa.

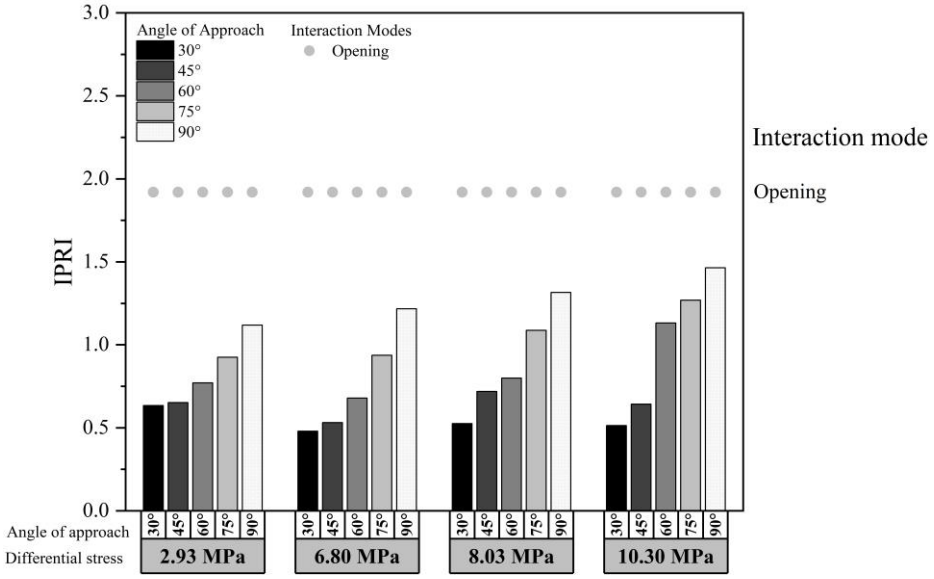

Figure 3.16 Numerical simulations of IPRI changes as a function of differential stress and angle of approach (friction coefficient is 0.25).

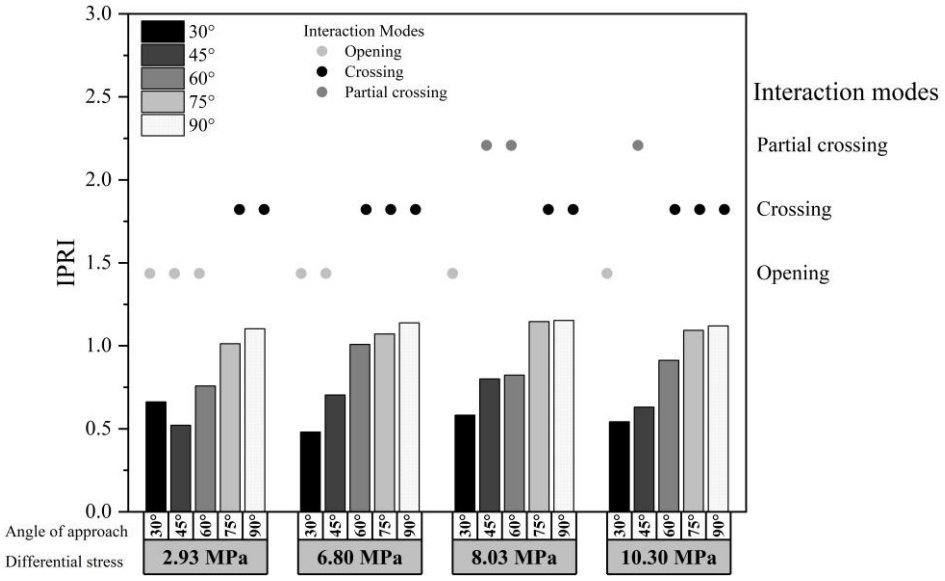

Figure 3.17 Numerical simulations of IPRI changes as a function of differential stress and angle of approach (friction coefficient is 0.90).

3.5.2.3 Effect of Fluid Viscosity

The fluid viscosity is an operational parameter that can be controlled in the design. Change of the fluid viscosity can increase the HF aperture and provide more energy for increasing the stimulated fracture complexity to increase ultimate production. Figure 3.18 presents the results of numerical simulations with different fluid viscosities on the interaction mode. It is seen that the more viscous the injecting fluid the more likely to observe the crossing mode. Comparing to the black dashed line from Figure 3.13, this suggests that a viscous injection fluid prone to crossing NFs.

Figure 3.19 shows the influence of the injecting fluid viscosity and interface friction on IPRI for an angle of approach of 60°. In these simulations, we changed the fluid viscosity from 0.002 Pa.s (slickwater) to 0.025 Pa.s (Linear gel). From this figure, one can see no noticeable changes when fluid viscosity increases from 0.002 to 0.004 Pa.s, however, when the viscosity reaches nearly 0.025 Pa.s, crossing becomes the dominant interaction mode associated with low IPRIs. This indicates that the high viscosity fluid requires a large amount of energy to propagate the fracture

into the formation, so when the high viscous fracture intersects a natural fracture, the crossing occurs at a small energy increase (or IPRI).

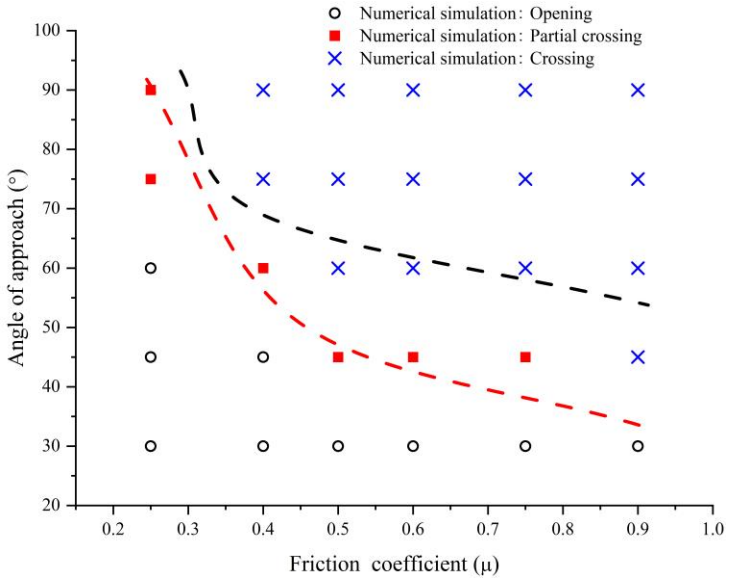

Figure 3.18 Numerical simulation results of the interaction mode for fluid viscosity of 0.025 Pa.s.

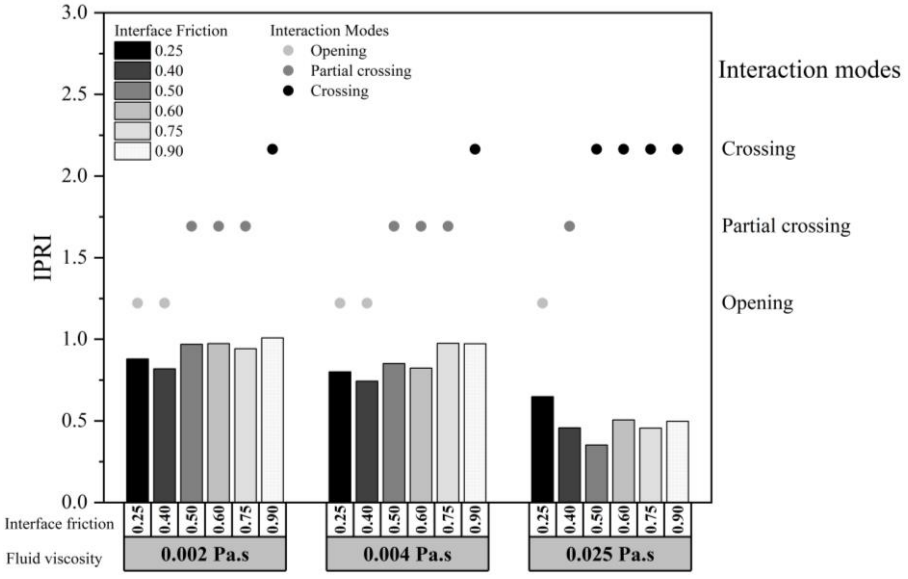

Figure 3.19 Simulation results of the interaction mode on IPRI (interface friction is 0.9).

3.6 Predictive Model

We ran 140 numerical simulations with range of varying input parameters including the stress difference, angle of approach, friction coefficient, and injecting fluid viscosity in order to build a large database with many interaction prediction cases. Table 3.3 shows the range of parameters considered in this practice.

Table 3.3 Range of the parameters used in simulation cases.

Parameter	Minimum	Maximum
Horizontal differential stress (MPa)	2.93	10.3
Angle of approach (°)	30	90
Interfacial coefficient of friction	0.25	0.9
Viscosity of fracturing fluid (Pa*s)	0.002	0.025

Commonly used classification models, including linear discriminant analysis (LDA), Naive Bayes classifier, Support vector machine (SVM), K-nearest neighbors (KNN), and Decision Trees (Morozov et al., 2020), were used to analyze the data and compare the results. Table 3.4 shows the accuracy of different models, which suggests that in this case the SVM presents the best overall accuracy of 65.7% with respects to other models. The use of the confusion matrix plot helps to evaluate the performance of different classifiers and to identify the areas where the classifiers performed poorly (Beale et al., 2020). The True positive rates (TPR) are the proportion of correctly classified observations per true class. The False negative rates (FNR) is the proportion of incorrectly classified observations per true class (Beale et al., 2020). Figure 3.20 shows the confusion matrix of SVM prediction results, where 0, 1, 2 binary numbers represent the opening, partial crossing, and crossing modes, respectively. The bi-column plot on the right side of the matrix shows summaries per true class. From this matrix it is seen that the model predicts crossing and opening modes with accuracies up to 76.8% and 80.7%, respectively. However, the partial

crossing is predicted with a low accuracy of only 11.1%. Figure 3.21 illustrates the distribution of IPRI for the three interaction modes using a box plot. Boxes are graphically depicting data through quartiles. Lines extend from the boxes indicate variability outside the upper and lower quartiles. Outliers are plotted as individual points. Opening and crossing can be easily distinguished by the box plot, but partial crossing has a significant overlap with other modes. It is understandable that partial crossing often occurs in some relatively complicated conditions and the box plot analysis can explain the reason for the low accuracy of predicting the partial crossing.

Table 3.4 Prediction accuracy with different developed prediction models.

Prediction model	Prediction accuracy
LDA	59.3%
Naive Bayes classifier	62.9%
SVM	**65.7%**
KNN	62.9%
Decision Tree	63.6%

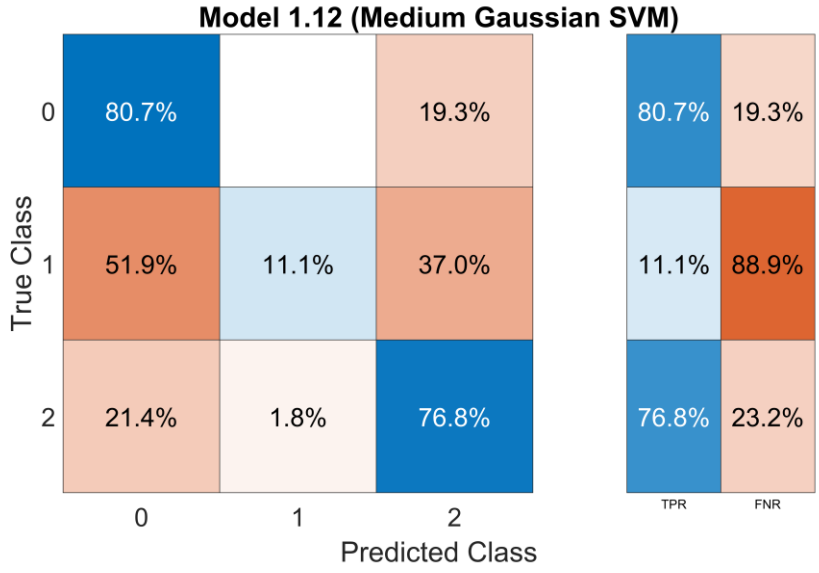

Figure 3.20 SVM Confusion matrix to evaluate the performance of the classifier in predicting the interaction modes.

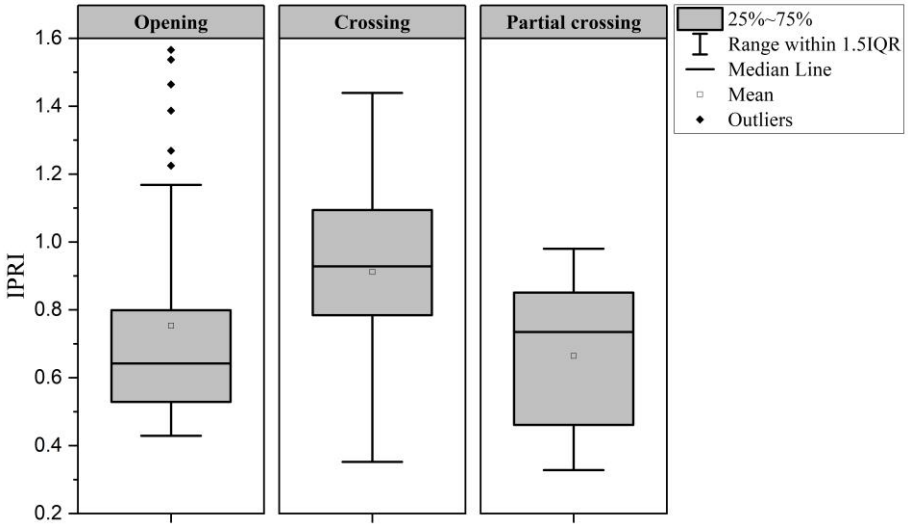

Figure 3.21 Illustration of IPRI distribution for the three interaction modes.

3.7 Lab Scale Case Study

In this section, the IPRI was applied to some lab experimental data to analyze the interaction modes. To prepare the testing rock, water was added to the mixture after the cement and sand were adequately mixed. Tested rocks are cut to create pre-existing natural fractures for testing. The testing parameters used in this study are listed in Table 3.5. The data was made available to us through personal communications (Jun Zhang).

Table 3.5 Experimental parameters of the lab test (Jun Zhang).

Case	**Angle of approach /°**	**Vertical stress/MPa**	**Minimum Principal stress/MPa**	**Principal stress difference/MPa**	**Fluid viscosity/Pa.s**	**Fluid injection rate/mL.min-1**	**Interface friction**
#3	45	30	18	6	0.001	5	0.540
#5	45	30	18	12	0.001	5	0.417
#8	60	30	18	6	0.001	5	0.582
#10	60	30	18	12	0.001	5	0.446
#14	90	30	18	6	0.001	5	0.540
#15	90	30	18	12	0.001	5	0.415

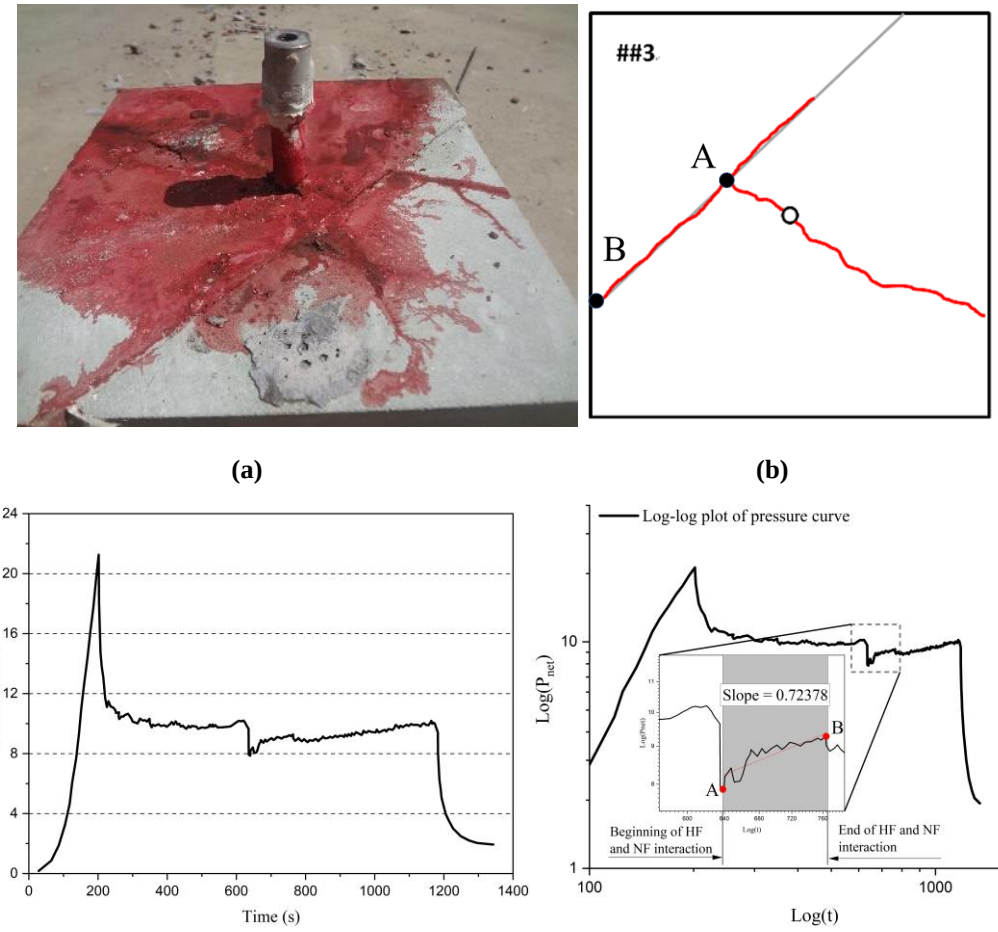

Figure 3.22 Case #3: (a) Sample view, NFs at of 45° with respect to HF, (b) model geometry, (c) recorded injection pressure, (d) log-log plot of pressure curve and slope of the pressurization zone right after the interaction (Jun Zhang).

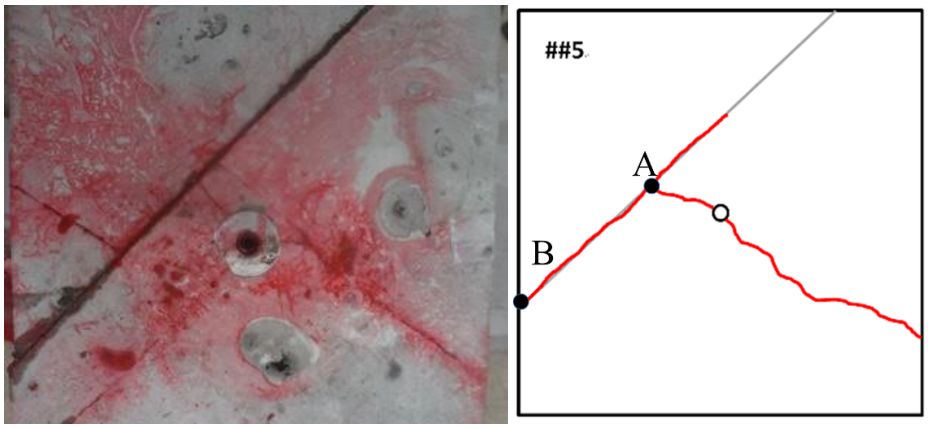

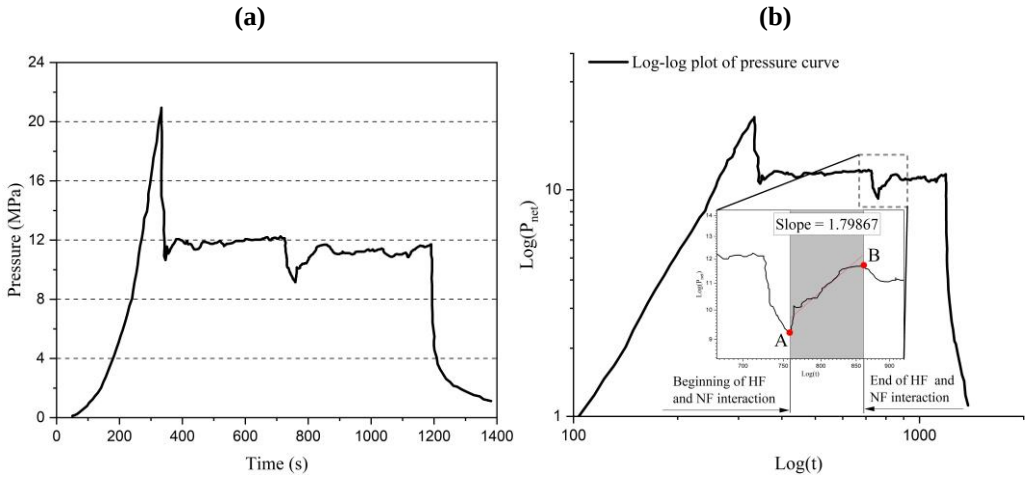

Figure 3.23 Case #5: (a) Sample view, NFs at of 45° with respect to HF, (b) model geometry, (c) recorded injection pressure, (d) log-log plot of pressure curve and slope of the pressurization zone right after the interaction (Jun Zhang).

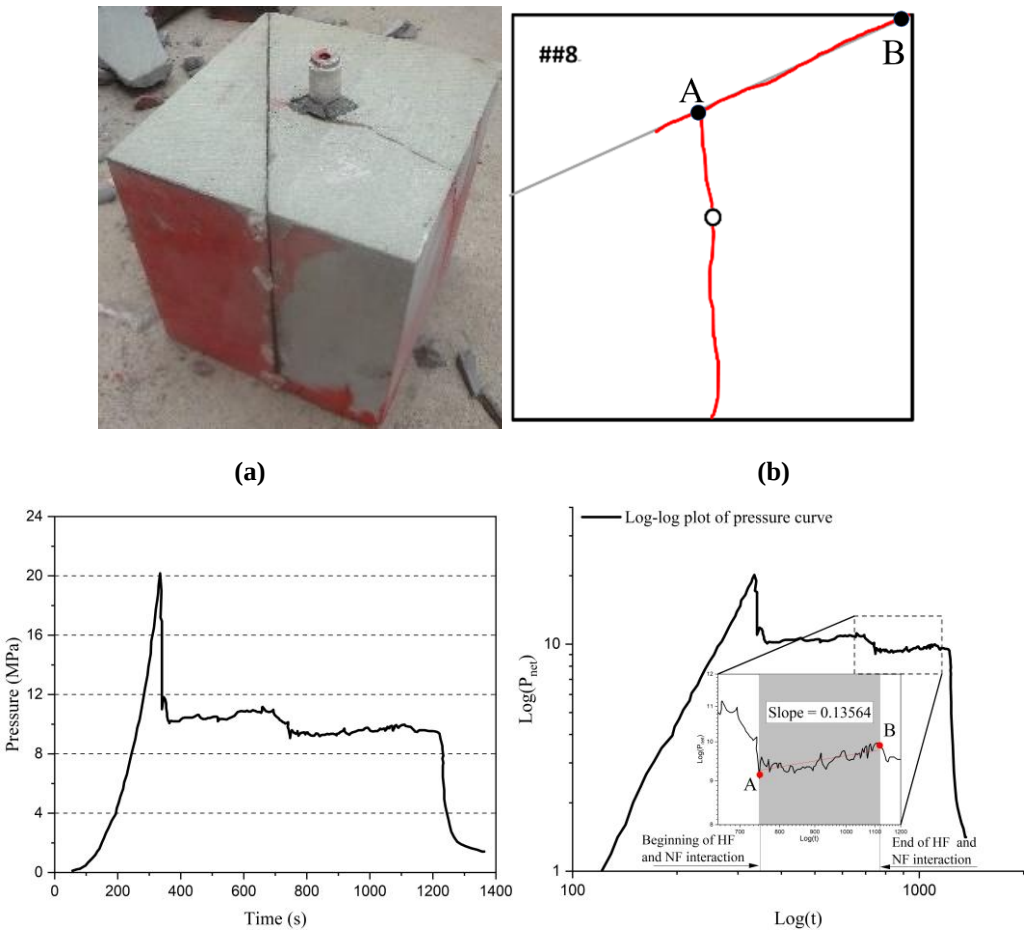

(c) **(d)**

Figure 3.24 Case #8: (a) Sample view, NFs at of 60° with respect to HF, (b) model geometry, (c) recorded injection pressure, (d) log-log plot of pressure curve and slope of the pressurization zone right after the interaction (Jun Zhang).

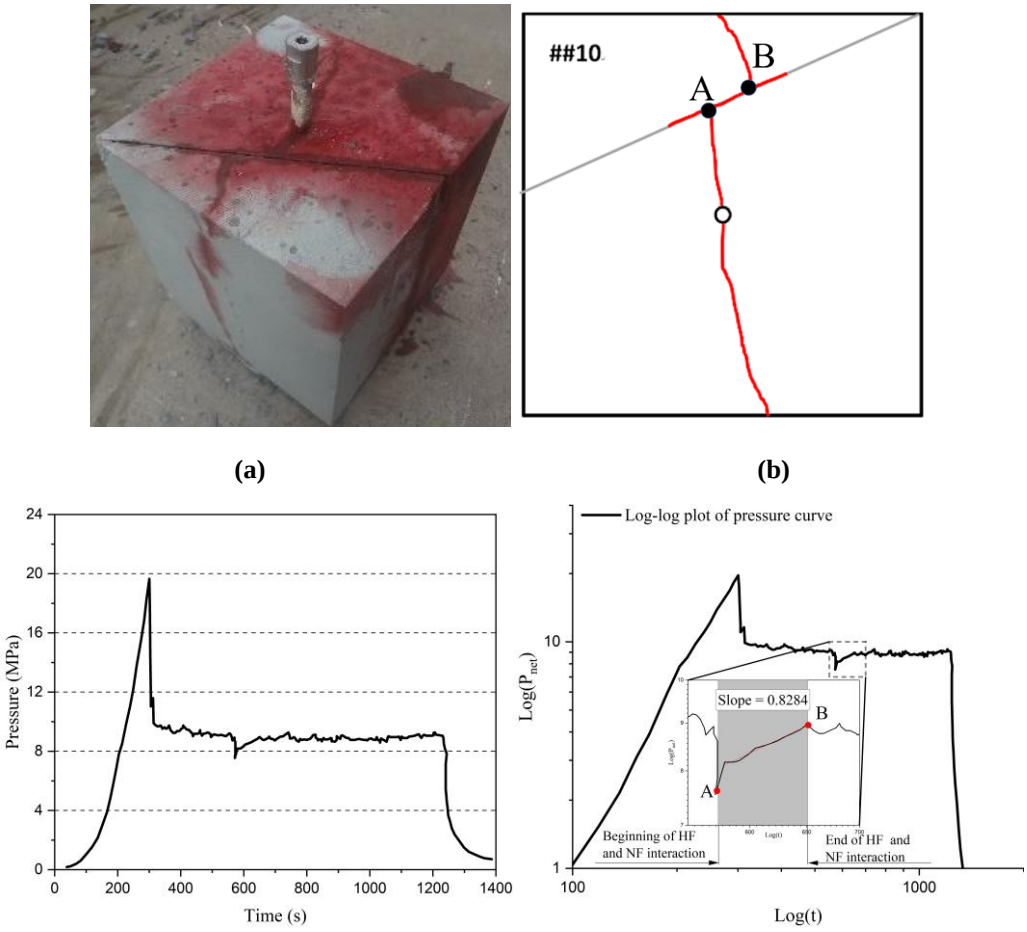

(a) **(b)**

(c) **(d)**

Figure 3.25 Case #10: (a) Sample view, NFs at of 60° with respect to HF, (b) model geometry, (c) recorded injection pressure, (d) log-log plot of pressure curve and slope of the pressurization zone right after the interaction (Jun Zhang).

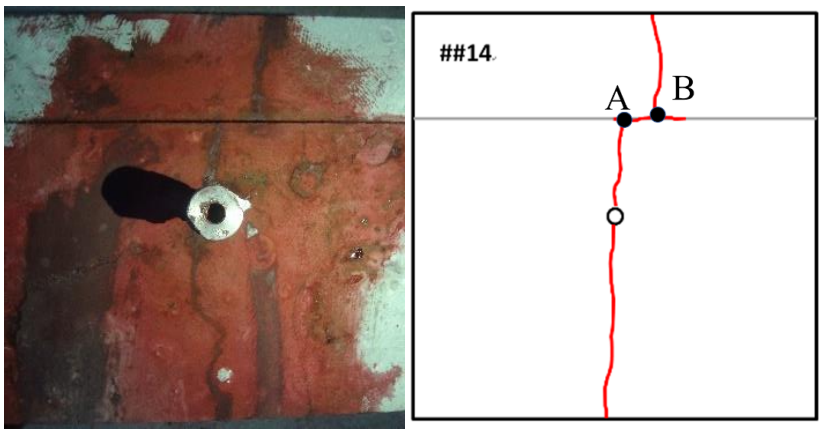

(a) **(b)**

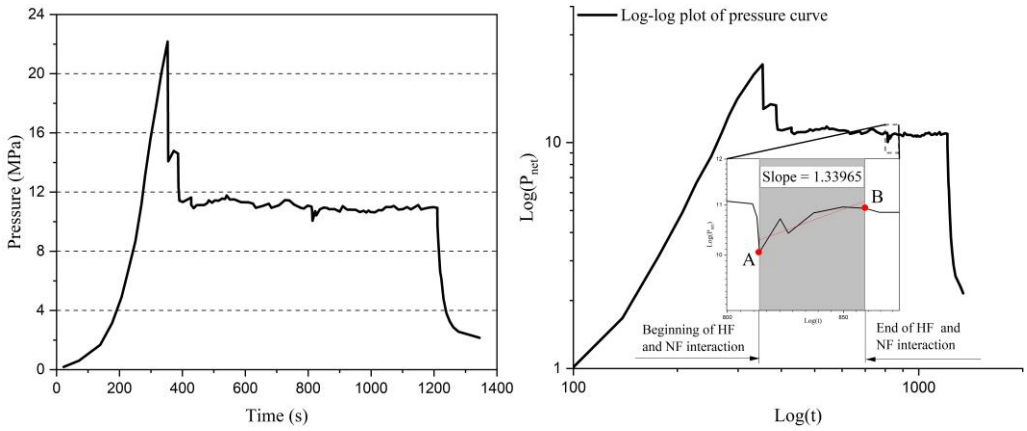

(c) **(d)**

Figure 3.26 Case #14: (a) Sample view, NFs at of 90° with respect to HF, (b) model geometry, (c) recorded injection pressure, (d) log-log plot of pressure curve and slope of the pressurization zone right after the interaction (Jun Zhang).

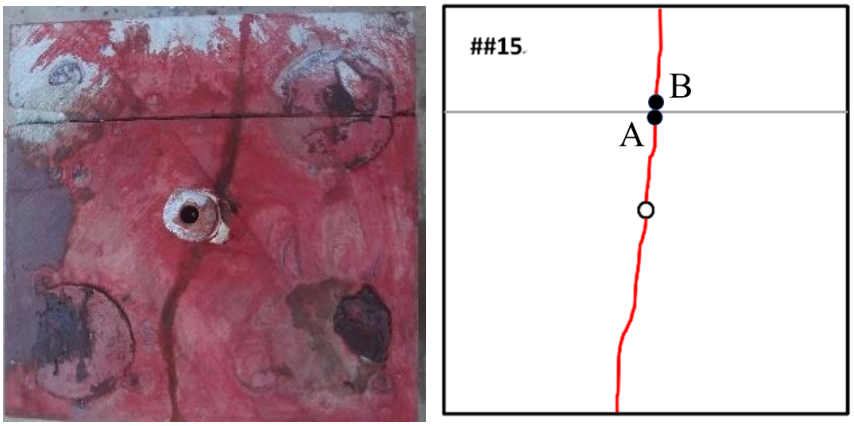

(a) **(b)**

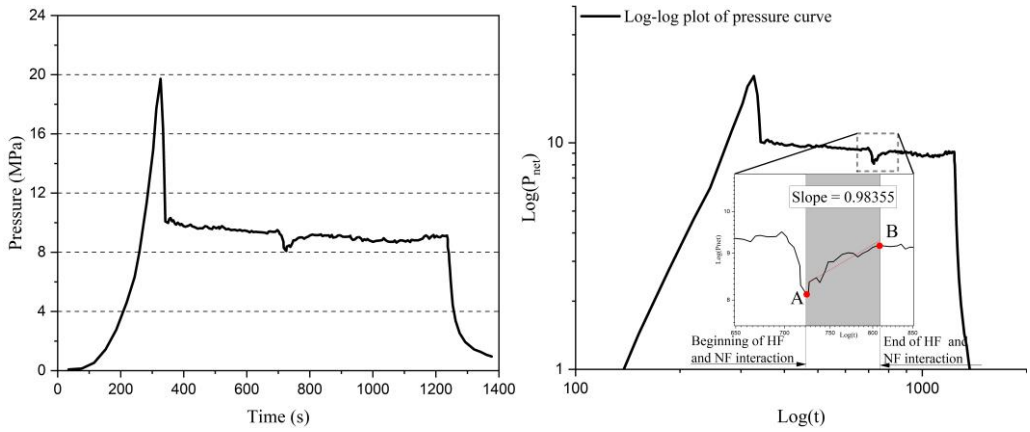

(c) **(d)**

Figure 3.27 Case #15: (a) Sample view, NFs at of 90° with respect to HF, (b) model geometry, (c) recorded injection pressure, (d) log-log plot of pressure curve and slope of the pressurization zone right after the interaction (Jun Zhang).

The sample geometry and pressure plots corresponding to the data of 6 lab experiments (Table 3.5) that were used in this study are shown in Figures 3.22 to 3.27. Point A corresponds to the sudden drop in the pressure curve in all 6 cases, the time when the HF intersects with NF. In Figure 3.22 to 3.24 after the intersection of the HF and NF (i.e., point A) the NF is opened resulting in an increase in pressure. However, in these three cases it is seen that the HF penetrates into the NF until it reaches the boundary of the sample from one side, which causes the release of the fluid and the pressure to drop. This moment is shown as point B in the pressure-time plot in these figures. The experiments shown in Figure 3.25 and 3.26 present offsetting and Figure 3.27 represents a crossing interaction mode. In these three cases, point B corresponds to the initiation of the HF on the other side of the NF. In these cases, the pressure between points A and B was used to obtain the IPRI. Table 3.6 summarizes the IPRIs corresponding to the 6 experiments. In this Table also the observed interaction modes from the experiments as well as what was predicted by the model are displayed. The results present good agreements between predictive model and actual interaction observed from the experiment for all cases except #8. For case #8, the pressure curve

did not return back to the pressure corresponding to the normal propagation after the first pressure drop that symbolizes the beginning of the interaction. A reason for this may be due to the fact that in these experiments, only one NF plane existed so while one HF wing intersected the NF, the second HF wing reached the boundary of the sample, which resulted in inadequate pressurization to support the HF propagation along the NF.

Table 3.6 Comparison between experimental test results and predicted results.

Case	IPRI	Predicted interaction modes	Actual interaction modes
#3	0.723	Opening	Opening
#5	1.798	Opening	Opening
#8	0.139	Partial crossing	Opening
#10	0.8284	Crossing	Crossing
#14	1.340	Crossing	Crossing
#15	0.984	Crossing	Crossing

3.8 Summary

This chapter presented a new approach to predict the interaction mechanism between a hydraulic fracture and a natural fracture. The method is based on the analysis of the slope of the log-log pressure time curve during fracture propagation phase, referred to as interaction pressurization rate index (IPRI). The IPRIs were extracted for several numerical simulations performed using a lattice-based simulator. The results compared reasonably well with the Blanton and Gu and Wang models. Also, sensitivity analyses of the angle of approach, interface friction, injecting fluid viscosity and differential stresses were done to investigate their impact on IPRI. The results showed that a noticeable increment in IPRI is observed when the angle of approach exceeds 60°. Interface friction owns a relatively stable IPRIs for crossing cases but an obvious trend of increase in opening mode. Differential stress is unlikely to affect the opening cases with low interface

friction but tends to dominate the crossing mode in a larger angle of approach and friction coefficient and maintain the IPRI within a small range of variation. High viscous fluid requires a large amount of energy to propagate the fracture into the formation, so a small IPRI is able to trigger the crossing. Finally, a predictive model was developed based on 140 simulation cases with varying input parameters. The results of the model showed a good ability to predict the interaction modes corresponding to some lab experimental data.

In the next Chapter, a detailed analysis of hydraulic fracture propagation path under the effect of mechanical properties and injection parameters will be conducted.

Chapter 4

Hydraulic Fracture Geometry Evolvement in Transversely Isotropic Formations

4.1 Introduction

Accurate prediction of the fracture geometry before operation of a HF job is important for the treatment design. The simplified planar fracture models, which may be applicable to predict the fracture geometry in homogeneous and continuous formations fail in case of fractured reservoirs and laminated formations such as shales. To gain a better understanding of the fracture propagation mechanism in laminated formations and its vertical geometry in specific, a series of numerical models was run using XSite, a lattice-based simulator. The results were studied to understand the impact of the mechanical properties of caprock and injection parameters on HF propagation. The tensile and shear stimulated areas were used to determine the ability of HF to propagate vertically and horizontally. The results indicated that larger caprock's Young's modulus increases the stimulated area (SA) in in both vertical and horizontal directions, whereas reduces the fracture aperture. Also, larger vertical stress anisotropy and tensile strength of caprock and natural interfaces inhibits the horizontal fracture propagation with inconsiderable effect in vertical propagation, which collectively reduces the total SA. It was also observed that increased fluid injection rate suppresses vertical fracture propagation with insignificant effect on horizontal

propagation. The dimensionless parameters defined in this study were used to characterize the transition of HF propagation behavior between horizontal and vertical HF.

4.2 Model Setup

In this study, a two-caprock layer model with laminations in a horizontal direction was established for simulation purposes. The model, as shown in Figure 4.1(a), has a length (along the X-axis), width (along the Z-axis), and height (along the Y-axis) of 10m, 8m, and 8m, respectively. The reservoir layer of 2m height is located in the middle of the model. The caprocks are homogenous material with 1m thickness placed above and below the reservoir formation. The six zero-thickness interfaces 1mapart from each other, as labeled from 1 to 6 in Figure 4.1(b) were used to characterize the cemented natural interface between layers. The principal stresses were considered as σ_h=5MPa, σ_v =10MPa, and σ_H =8MPa, in X, Y, and Z directions, respectively. It is important to note that, in order to speed up the simulations, the stress differences were applied to the model rather than the total stresses. This will have no impact on the fracture geometry but only fracture pressures. The fracture is initiated from a cluster in the middle of a horizontal wellbore which is placed along the X-axis (or σ_h) direction. The spherical cluster is the point of fracturing fluid injection and a small starter crack (notch) is placed perpendicular to σ_h in order to facilitate fracture initiation.

The mechanical properties of this model, which are typical values of a tight unconventional formation, are listed in Table 4.1. The injection fluid is Slick water with a viscosity of 0.001Pa.s. The simulation was run in a mechanical step for 0.1s to achieve an initial model equilibrium and continued in the fluid-solid coupling mode after starting the fluid step.

Table 4.1. Input parameters of the simulation models.

Parameters	Reservoir	Caprocks	Interfaces
Tensile strength, T_0, (MPa)	3.5	3.5	2.1
Friction angle, θ, (°)	26.565	26.565	30
Uni-axial compressive strength, UCS, (MPa)	79.5	79.5	-
Young's modulus, E, (Gpa)	27.2	60	-
Uni-axial Poisson's ratio, v	0.221	0.221	-
Density, (kg/m^3)	2600	2600	-
Porosity, ϕ, (%)	14.7	14.7	-
Permeability, K, (m^2)	1.7×10^{-15}	1.7×10^{-15}	-
Cohesion, S_0, (MPa)	-	-	6

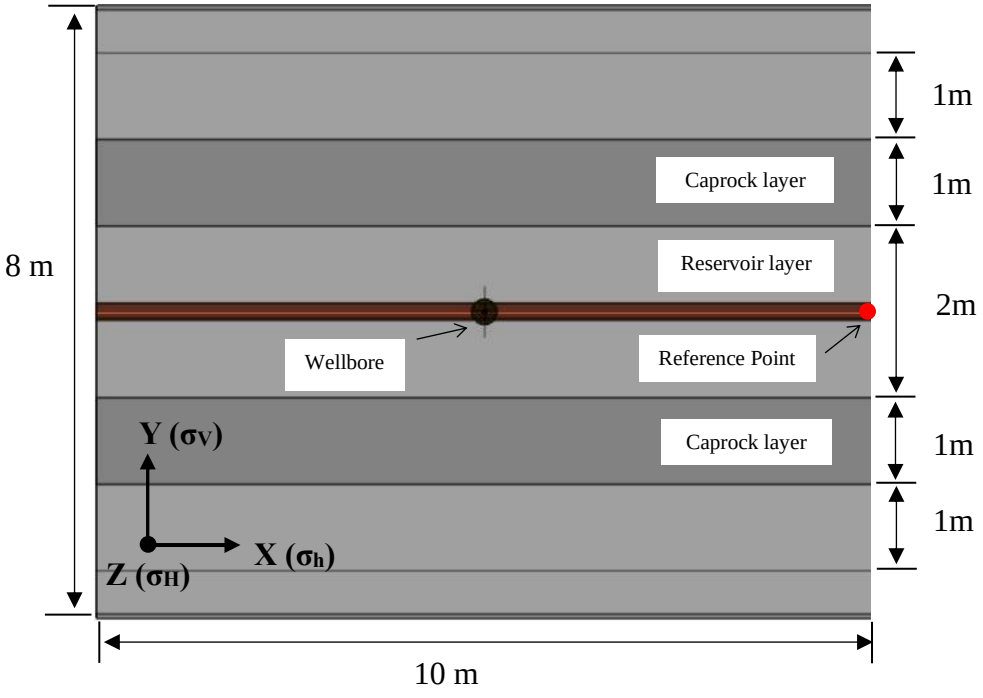

(a) Front view of the model.

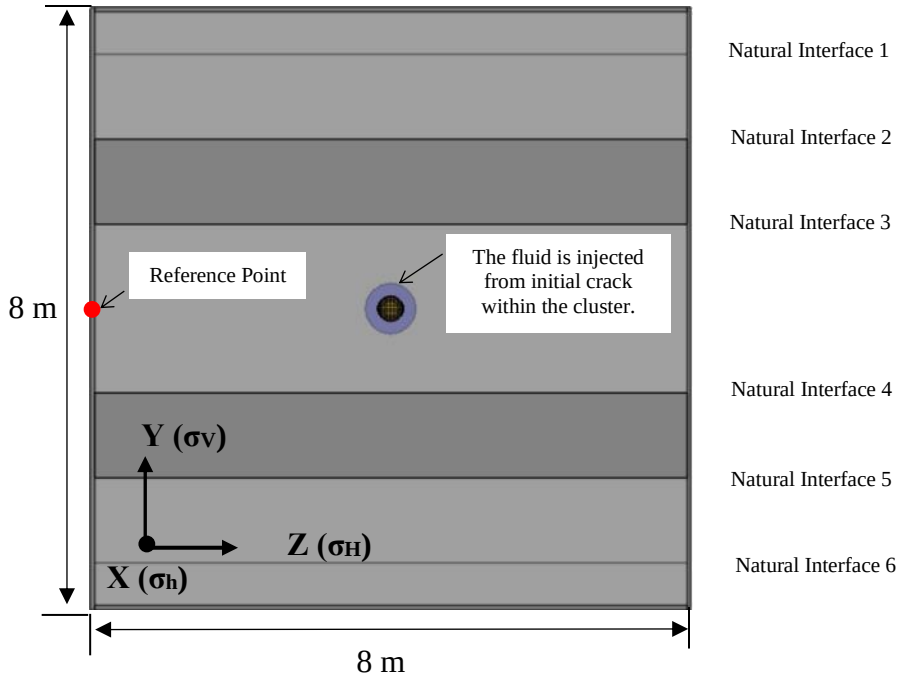

(b) Side view of the model.

Figure 4.1 Sketch of the numerical model: (a) Front view (X-Y plane), (b) Side view(Y-Z plane).

4.3 Results and Analysis

Complex fracture geometries consist of tensile and shear fractures (Settgast et al., 2017). To quantify the simulation results of HF propagation in a laminated reservoir, the concept of stimulated area (SA) is proposed to evaluate the fracture area generated by HF. The shear stimulated area (SSA) is defined as the region containing natural discontinuities that are subjected to shear slippage. By contrast, the tensile stimulated area (TSA) refers to the area where tension fractures form. These two parameters are used to describe the HF extensional patterns in laminated formations. The SSA may represent the area along the natural interface that is stimulated by HF. The higher SSA along an interface means larger fracture connectivity. On the other hand, the TSA may be more representative of the vertical extension of HF (i.e., fracture height). The greater the TSA in the vertical direction, the larger fracture penetration. In the following sections the effect of Caprock's Young's modulus, stress anisotropy, interface properties, and injecting fluid rate on SSA and STA and hence fracture geometry will be modeled, and the results are discussed.

4.3.1 Young's Modulus

The effect of Young's modulus on HF geometry is presented here. The caprocks Young's modulus was varied from 20MPa to 27.7MPa, 40MPa, 50MPa, and 60MPa, while the reservoir formation Young's modulus was kept unchanged at 27.7MPa. The front view (X-Y plane) and side view (Y-Z plane) of the simulation results are shown in Figures 4.2 and 4.3, respectively. The results illustrate that the caprock inhibits HF vertical propagation but promotes its extension along the interfaces between adjacent layers, particularly the inner interfaces near the injection point. In order to examine the effect of angle of approach, the models were run at inclinations of 0°, 10°, and 20°. The results show the greater the inclination, the larger the slippage area. This is in agreement with previously published results (Goldstein & Osipenko, 2015).

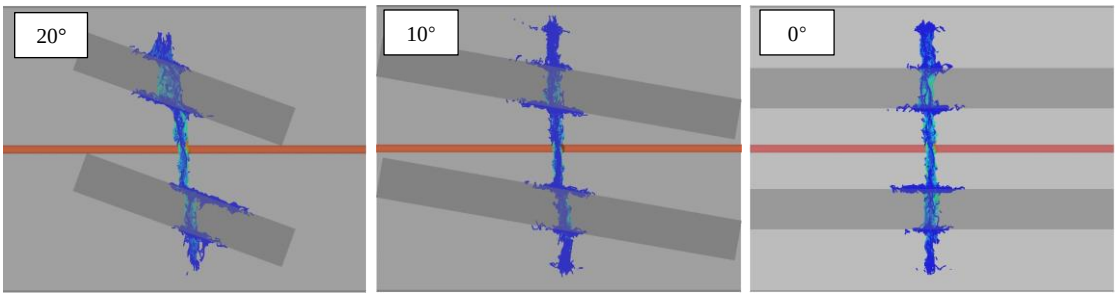

(a) *E*=20MPa

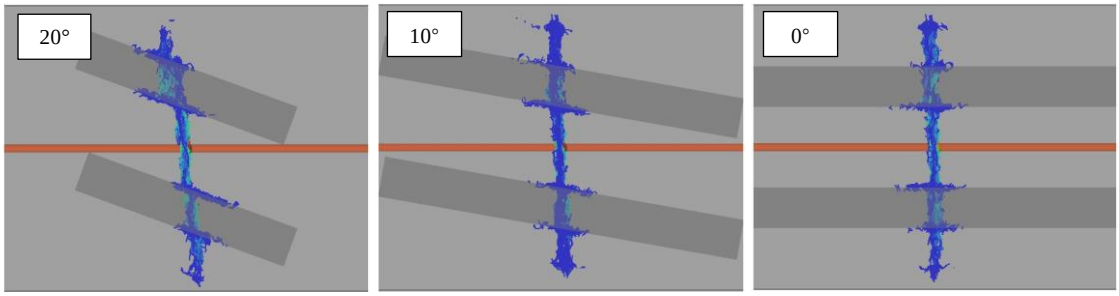

(b) *E*=27.7 MPa

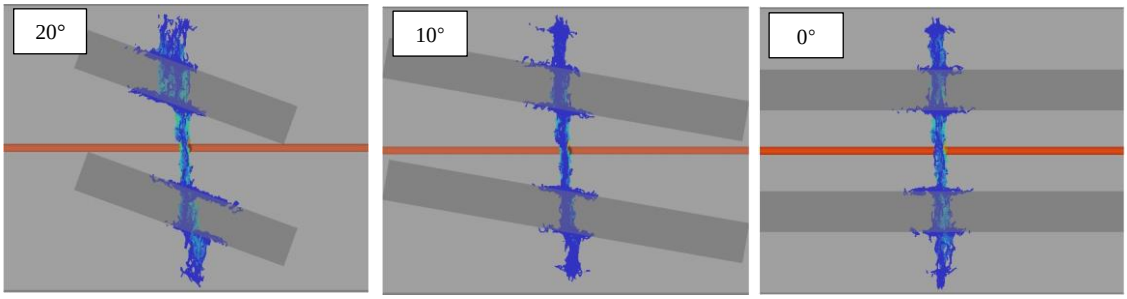

(c) E=40 MPa

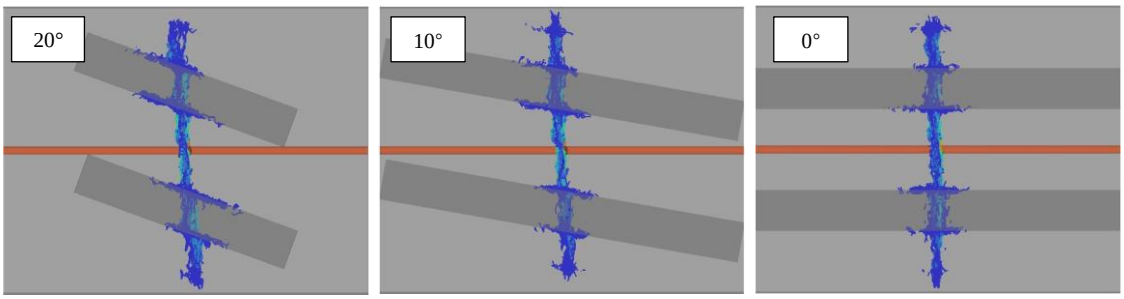

(d) *E*=50 MPa

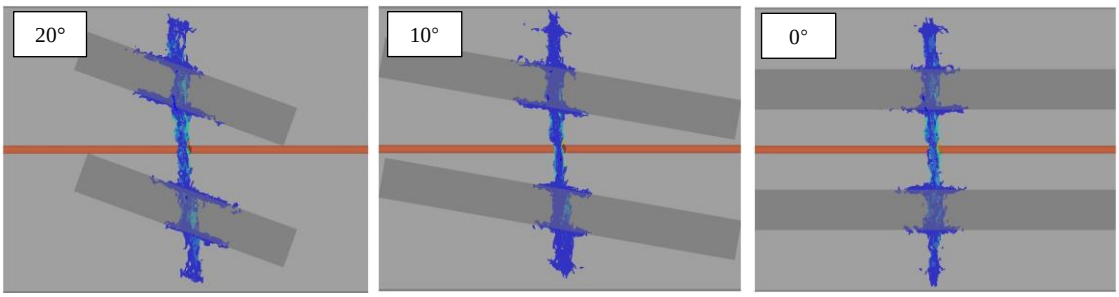

(e) *E*=60 MPa

Figure 4.2 The effects of caprock's inclination and Young's modulus on fracture propagation in a laminated reservoir. The images show the model front view with Young's modulus of (a) 20 MPa, (b) 27.7 MPa, (c) 40 MPa, (d) 50 MPa, and (e) 60 MPa.

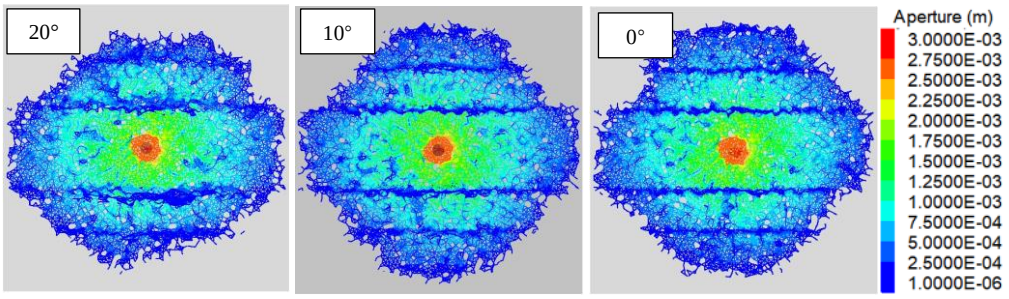

(a) *E*=20MPa

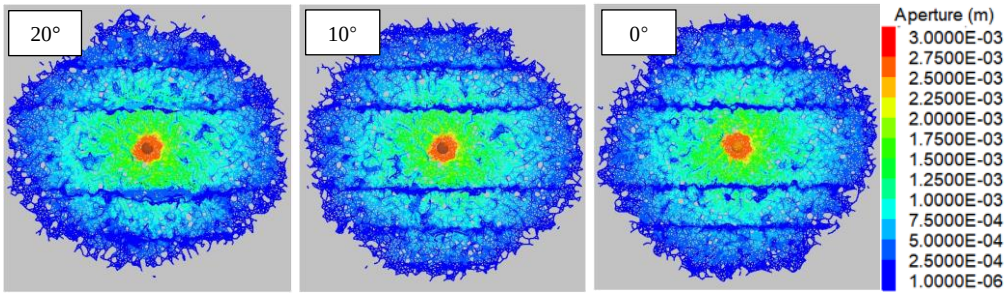

(b) *E*=27.7MPa

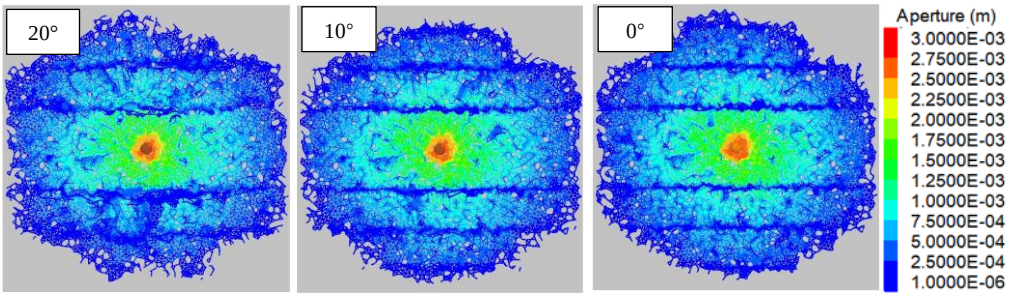

(c) *E*=40MPa

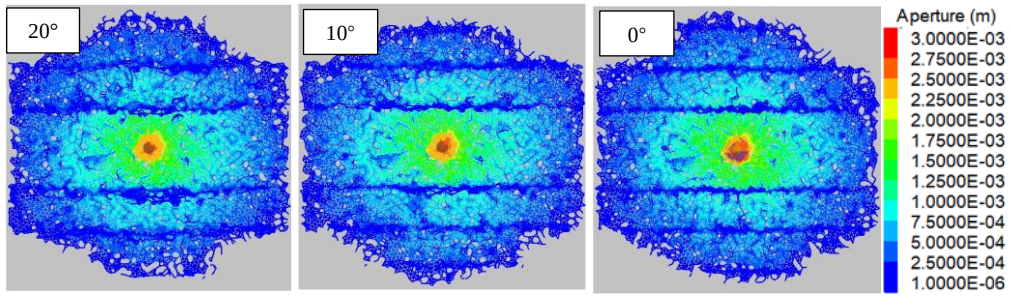

(d) *E*=50MPa

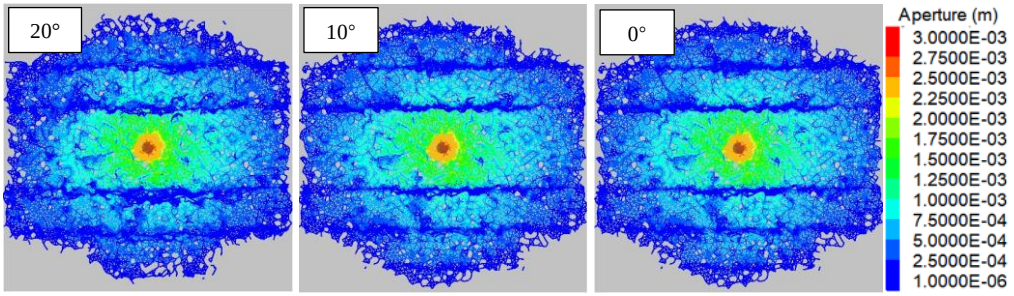

(e) *E*=60MPa

Figure 4.3 The effect of caprock's inclination and Young's modulus on fracture propagation in a laminated reservoir. The images show the model side view with Young's modulus of (a) 20 MPa, (b) 27.7 MPa, (c) 40 MPa, (d) 50 MPa, and (e) 60 MPa.

Figure 4.4 presents the TSA and SSA corresponding to the results of Figures 4.2 and 4.3. The Total-SA is the sum of the TSA and SSA. The results of this Figure show that TSA and SSA values are increasing in lockstep as the caprock's Young's modulus increases. However, the change in inclination for TSA and SSA shows the opposite trend. Larger inclinations correspond to higher SSAs but lower TSAs. This is due to the fact that when the HF intersects the natural interface orthogonally (i.e., the layers inclination is 0°), as opposed to lower angle of approaches, the crossing interaction mode is more favorable to occur. This finding agrees with previous research works (Gu & Weng, 2010).

When the caprock's stiffness is increased, an increase in TSA and SSA is observed. To elucidate this conclusion further, a detailed analysis of the HF aperture was performed, and the corresponding results are shown in Figure 4.5. The aperture profiles in the Y-Z plane for cases

involving caprocks with a Young's Modulus of 20 MPa and 60 MPa are shown in this figure. Figure 4.5(a) shows a smooth decline of the aperture along the Y axis, whereas an obvious drop occurs at the interface between the reservoir and caprock layer. This is because Young's modulus is a mechanical property that quantifies the relationship between tensile stress and axial strain; thus, when a fracturing fluid with uniform fluid pressure transits from a high to lower Young's modulus layer, the high modulus rock will exhibit a relatively small strain. Additionally, to illustrate the increase in SSA, or the natural interface slippage area, profiles of natural fractures aperture are shown in Figure 4.6(a) and (b) for Young's modulus values of 20 MPa and 60 MPa in the Y-Z plane. When natural interfaces in the same position are compared, the lower stiffness case exhibits a larger aperture value. Additionally, for a single case, one can observe that the interfaces between the reservoir and caprock layer exhibit a greater aperture than those farther from the injection point, particularly in the area contacted by HF interfaces.

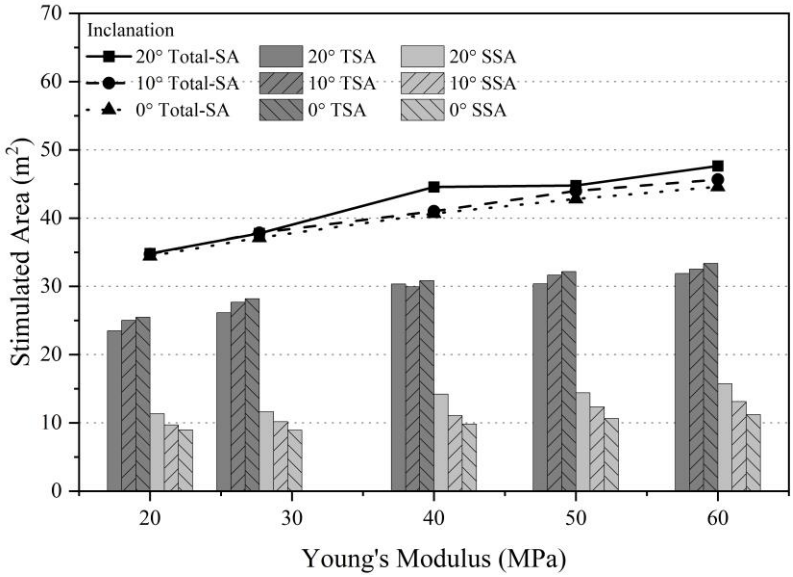

Figure 4.4 The effect of caprock's Young's modulus and inclination on tension and shear stimulated area (TSA and SSA).

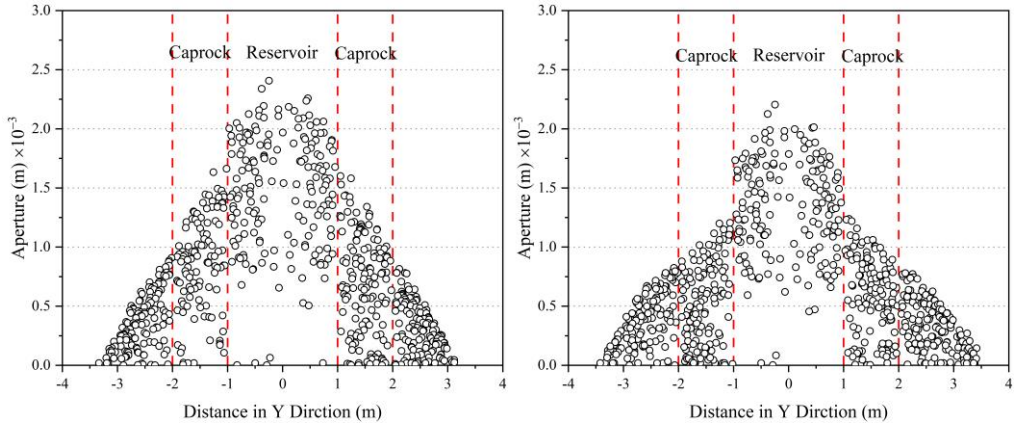

(a) *E*=20MPa **(b) *E*=60MPa**

Figure 4.5 Profiles of HF aperture in YZ plane at X=-5m for caprock's Young' s modulus of (a) 20 MPa, and (b) 60 MPa. Wellbore injection point is at Y=0 m.

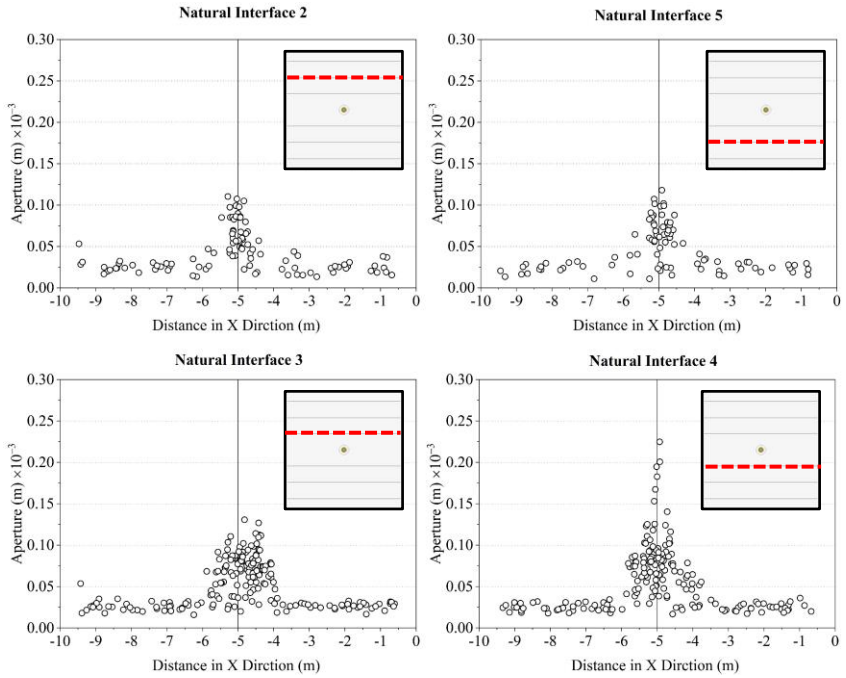

(a) *E*=20MPa

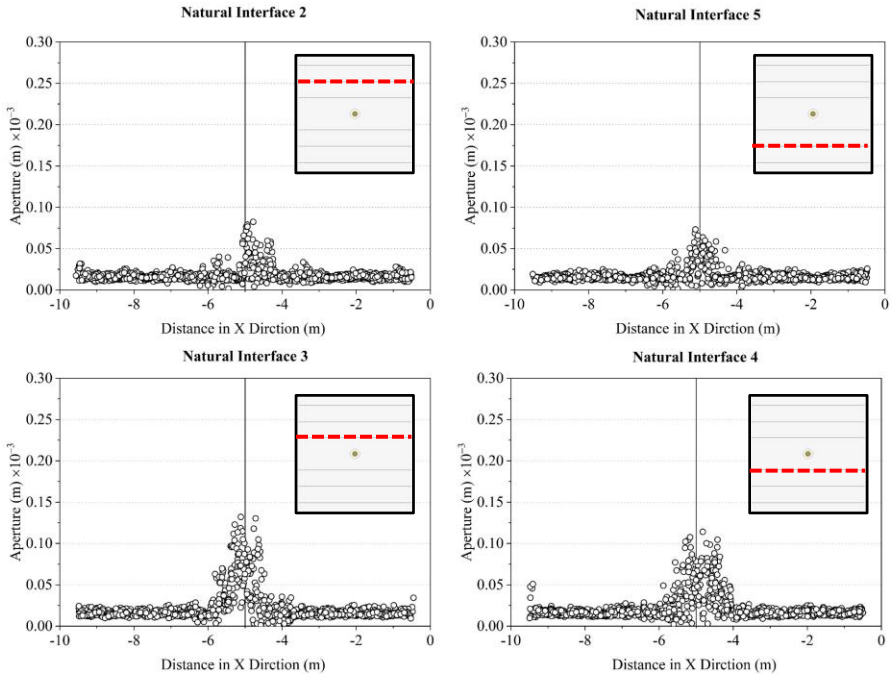

(b) *E*=60MPa

Figure 4.6 Profiles of natural interface aperture in XZ plane at Z=4m for caprock's Young' s modulus of (a) 20 MPa, and (b) 60 MPa. HF cross section appears at X=-5 m.

4.3.2 Vertical Stress Anisotropy

To investigate the effect of vertical stress anisotropy (or differential stresses), the vertical stress (σ_v) was changed from 8MPa to 10MPa, 12MPa, and 14MPa, while the minimum horizontal stress remained constant at σ_h =5MPa. The front (X-Y plane) and side view (Y-Z plane) of the simulation results are shown in Figures 4.7 and 4.8, respectively.

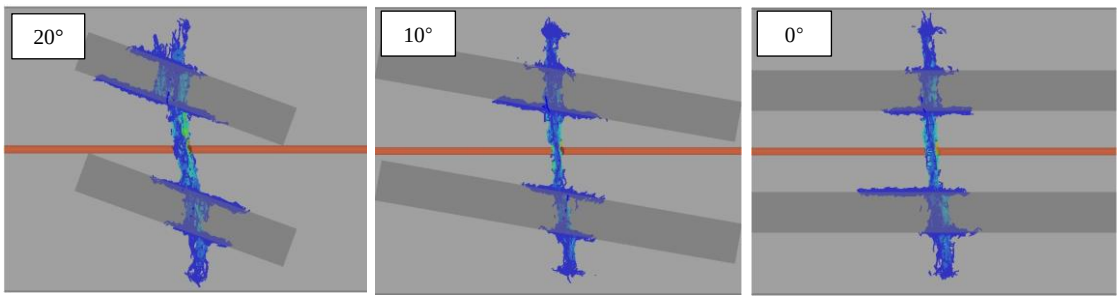

(a) *σv*=8MPa

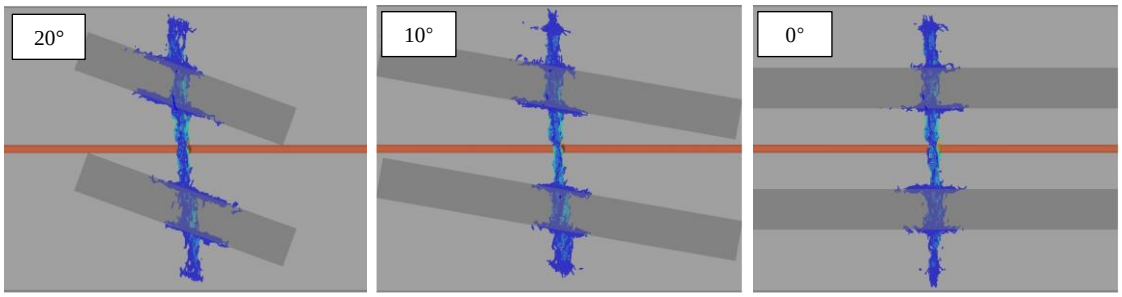

(b) σ_v=10MPa

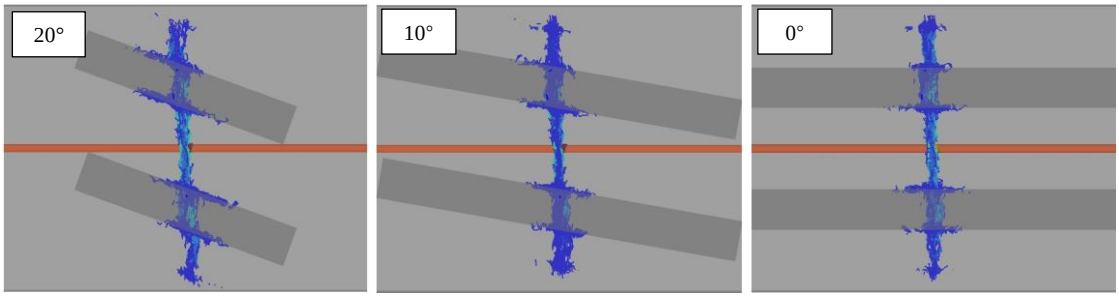

(c) σv=12MPa

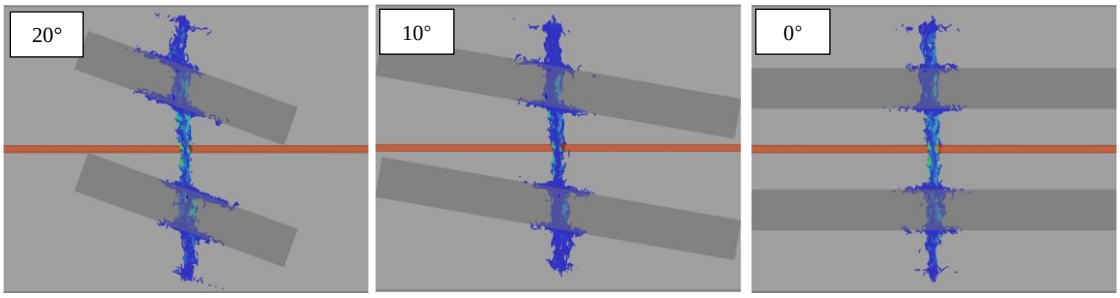

(d) σv=14MPa

Figure 4.7. The effects of caprock's inclination and stress anisotropy on fracture propagation for vertical stresses of (a) 8 MPa, (b) 10 MPa, (c) 12MPa, and (d) 14 MPa. The images show the model front view.

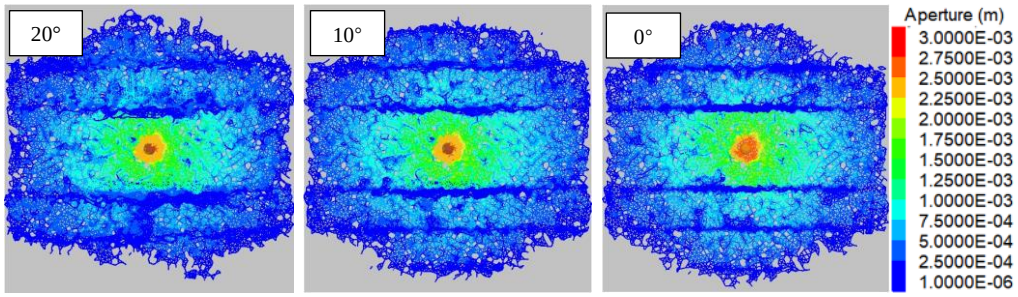

(a) σv=8MPa

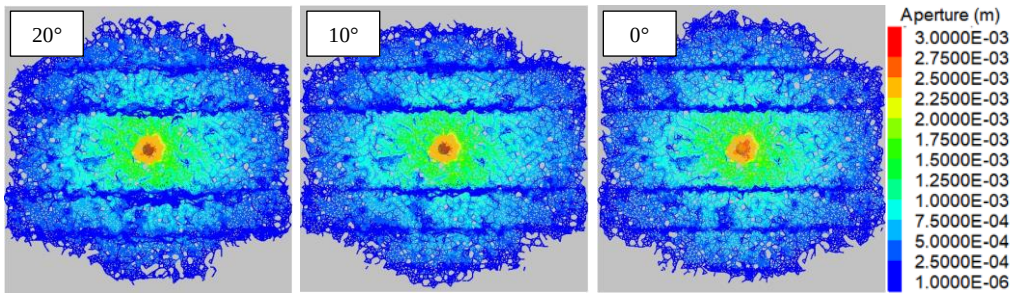

(b) σ_v=10MPa

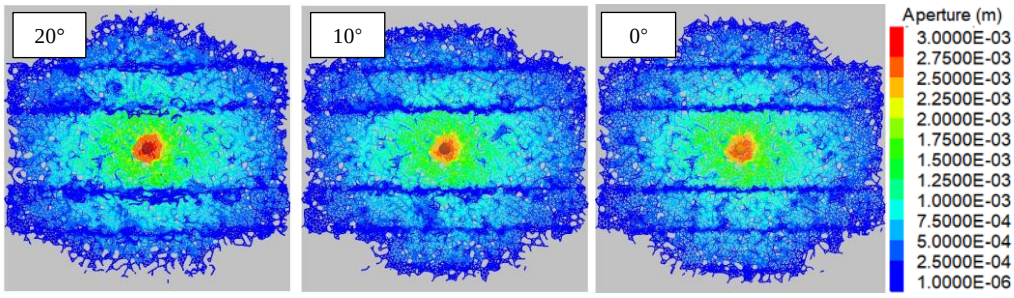

(c) σv=12MPa

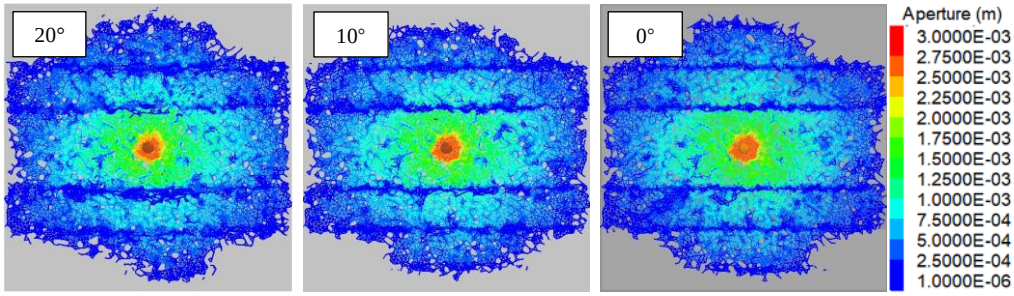

(d) σv=14MPa

Figure 4.8 The effects of caprock's inclination and stress anisotropy on fracture propagation for vertical stresses of (a) 8 MPa, (b) 10 MPa, (c) 12MPa, and (d) 14 MPa. The images show the model side view.

Figure 4.9 presents the TSA and SSA corresponding to Figures 4.7 and 4.8. From these figures, it is seen that as σ_v increases, the total-SA decreases. Specifically, the SSA has the largest proportion of the contribution to the total-SA decline compared to TSA, implying that high stress anisotropy results in less stimulation of the interface during HF operation. This finding is also reported by previous research, which claimed a higher differential stress cause a shorter offset in the interfaces (D. A. Chuprakov et al., 2010).

Figure 4.10 compares the HF apertures for two cases of σ_v=8 MPa and σ_v=14 MPa. From this figure, which shows the distribution of the apertures in the YZ plane, it is seen that the corresponding apertures increase from 1.1×10^{-3}m to 1.4×10^{-3}m level. This means that higher stress anisotropy increases the aperture of the fracture that has penetrated the caprock. This is a reasonable result, as when the stress anisotropy increases, it results in less chance for the fluid to penetrate into natural interfaces, so its energy is spent on fracture penetration in the caprock. In the case of higher stiffness for the caprock than the reservoir formation, the fluid energy will create larger width than length, as discussed before. Figure 4.11 shows the plot of the apertures in the XZ plane and the results demonstrate that low stress anisotropy favors penetration of the fluid into the interface with larger likelihood of aperture slippage.

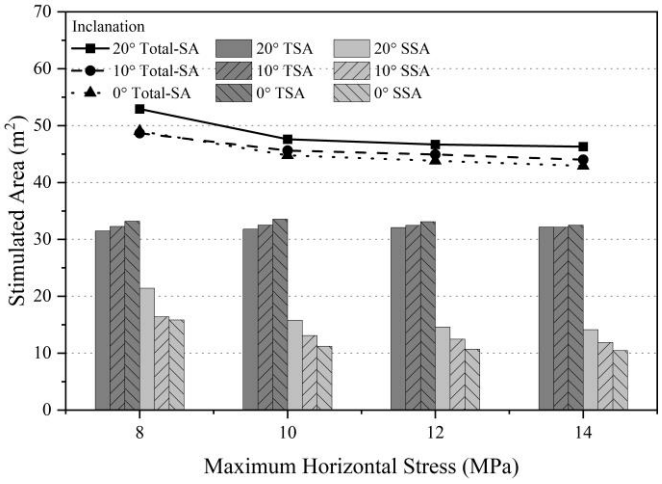

Figure 4.9 Effect of caprock vertical differential stress and inclination on tension and shear stimulated area.

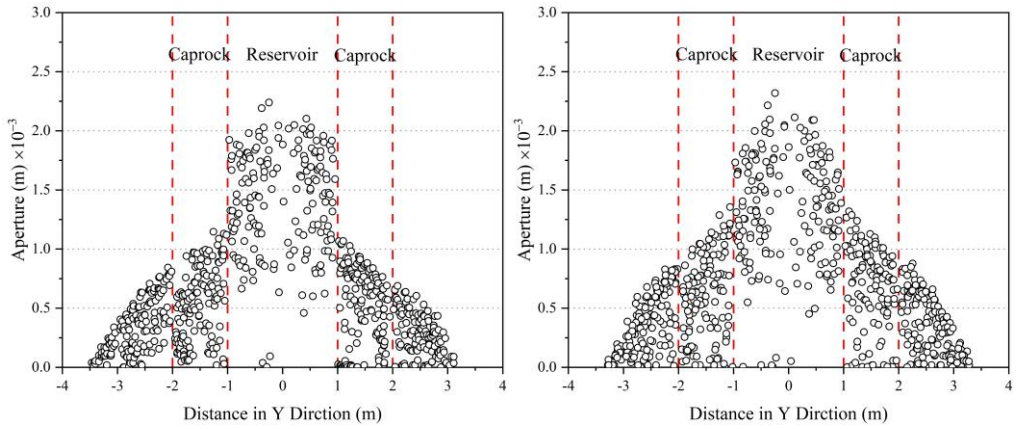

(a) σ_v=8MPa **(b) σ_v=14MPa**

Figure 4.10 Profiles of HF aperture in YZ plane at X=-5m for vertical stress of (a) 8MPa, and (b) 14MPa. Wellbore injection point is at Y=0 m.

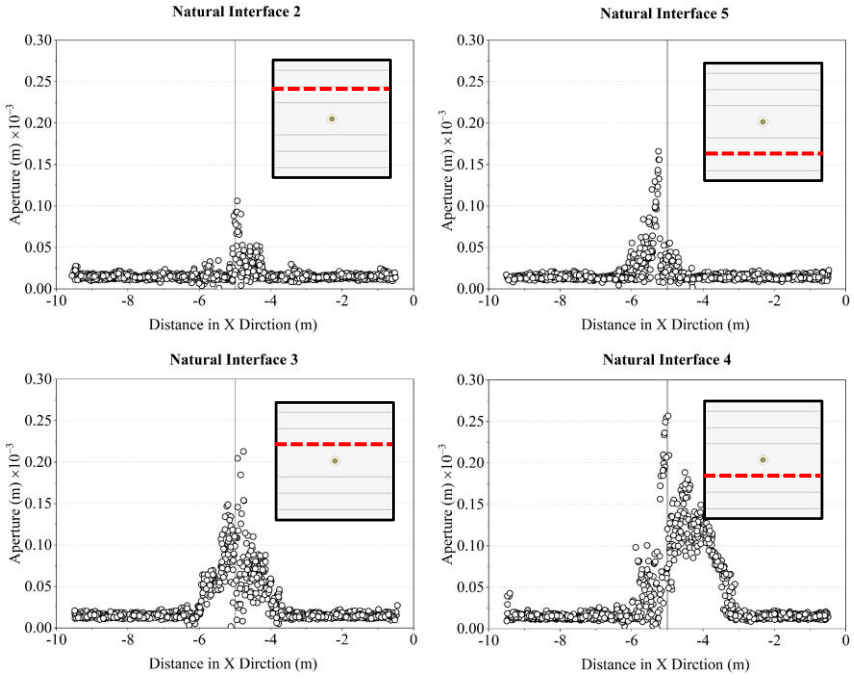

(a) σv=8MPa

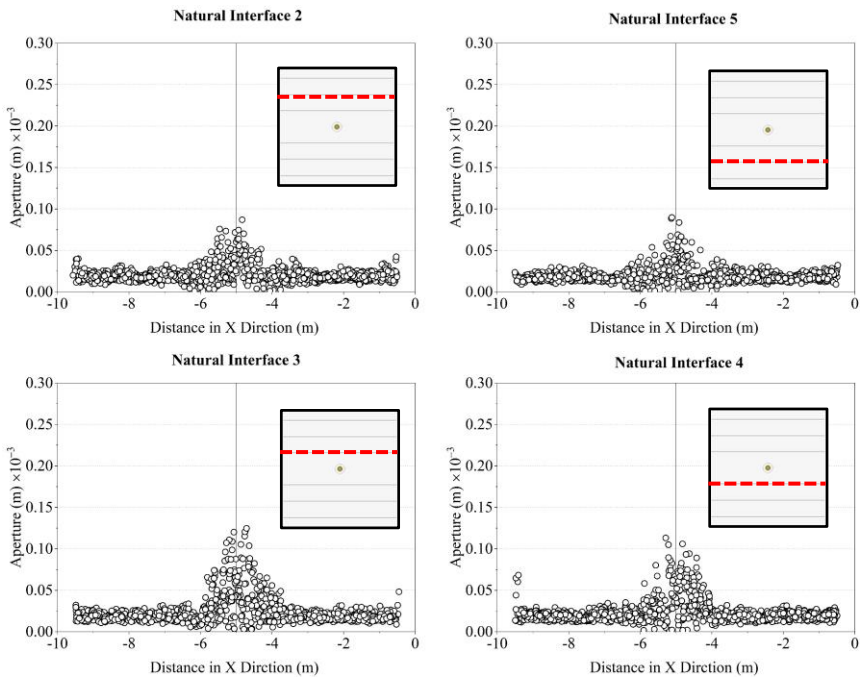

(b) σ_v=14MPa

Figure 4.11 Profiles of natural interface aperture in XZ plane at Z=4m for vertical stress of (a) 8MPa, and (b) 14MPa. HF in this plane is at X=-5 m.

4.3.3 Tensile Strength

Hao and Arash (2019) performed a numerical simulation of hydraulic fracture propagation in a complex fracture network (Figure 4.12). In this study, the E-W fractures (σ_H direction) and N-S fractures (σ_h direction) own 2.48 MPa and 0.62 MPa maximum tensile strength, respectively. Results showed HF grown along two N-S natural fractures (in σ_h direction) resembles classic double wing symmetric fractures, revealing the natural fractures can be re-open in low tensile strength even they perpendicular to the maximum principal stress. Therefore, the pressure required to reactivate natural fractures in reservoir is a function of the natural fractures plane normal stress and their tensile strength.

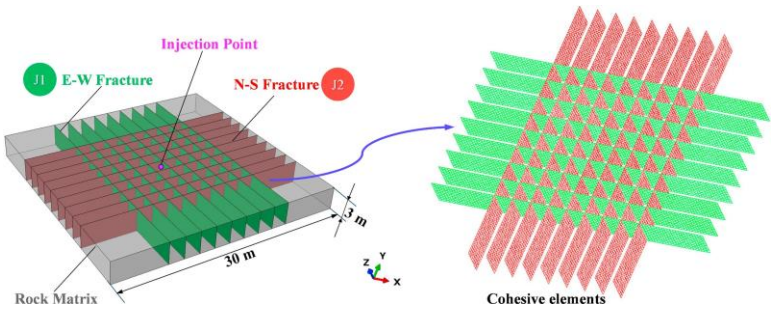

(a)

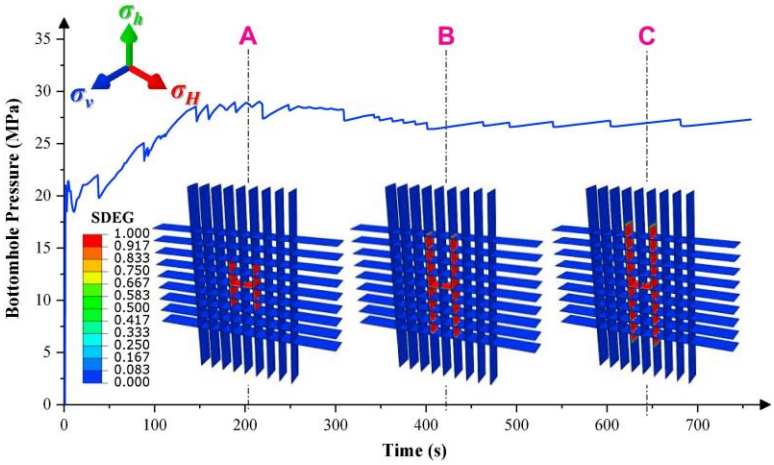

(b)

Figure 4.12 Hydraulic fracture propagation path in natural fracture networks: (a) The Finite element model geometry, (b) Hydraulic Fracture propagation along the weak tensile strength natural fractures.

In this section, the impact of the tensile strength (*T*) of both caprock and interface on HF propagation are studied by synchronize change the *T* values from 0.5 MPa to 3.5MPA and 5.0 MPa. The front and side views of the models are depicted in Figures 4.13 and 4.14.

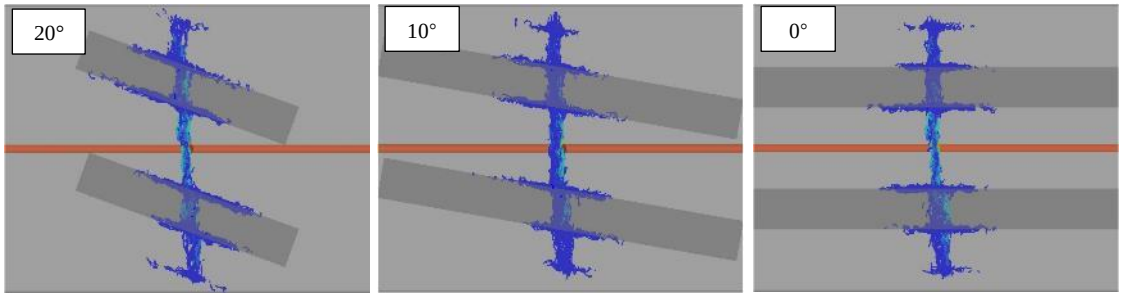

(a) *T*=0.5 MPa

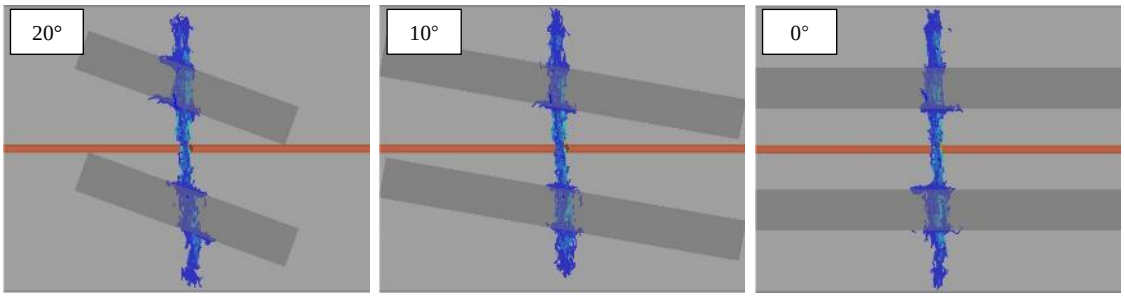

(b) *T*=3.5 MPa

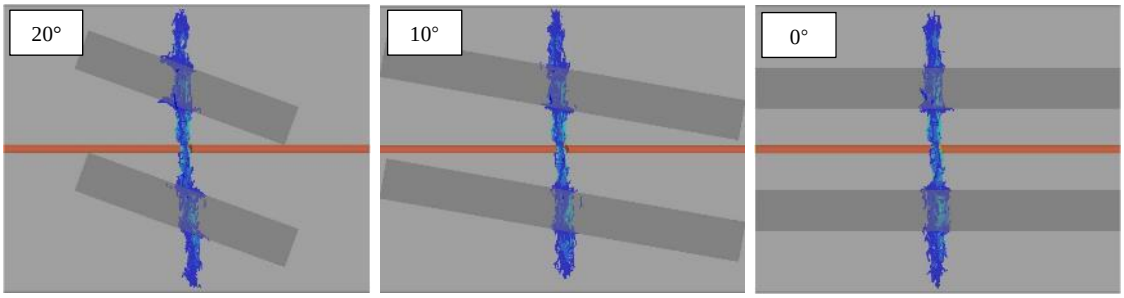

(c) *T*=5.0 MPa

Figure 4.13 The effects of caprock's inclination and Tensile strength on fracture propagation for tensile strengths of (a) 0.5 MPa, (b) 3.5 MPa, and (c) 5.0 MPa. The images show the model front view.

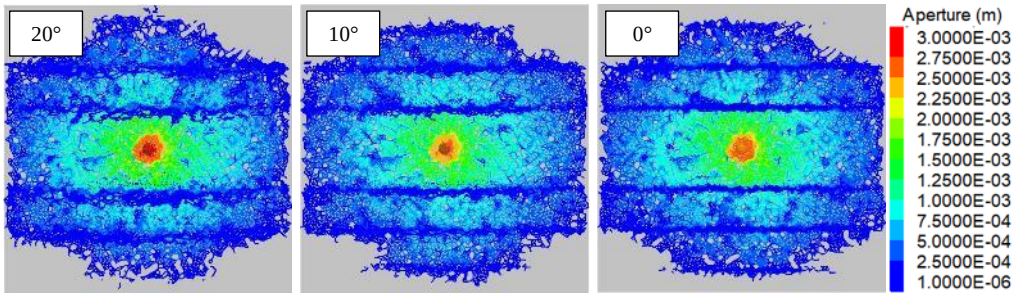

(a) *T*=0.5 MPa

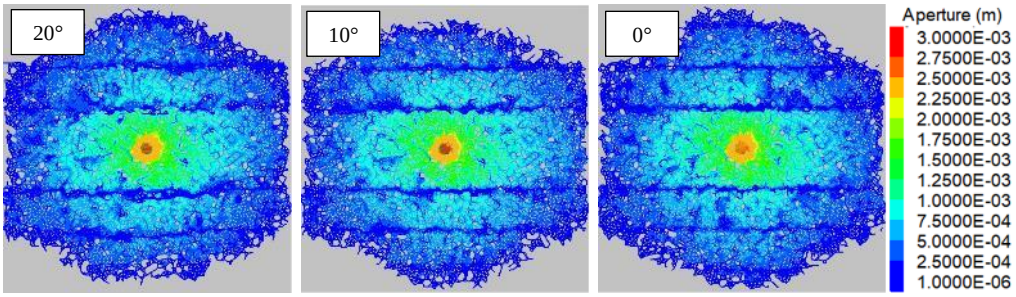

(b) *T*=3.5 MPa

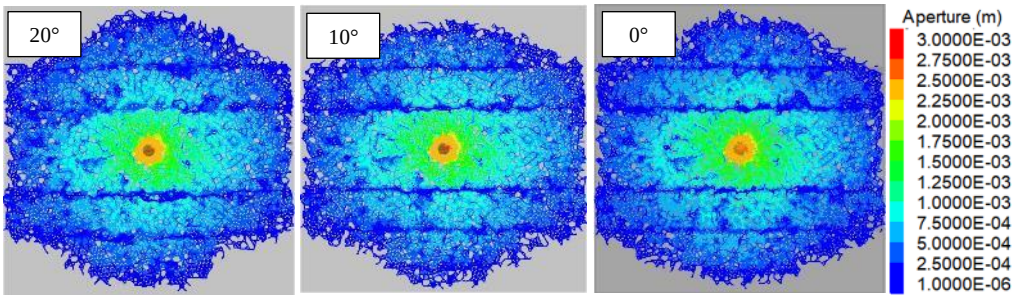

(c) *T*=5.0 MPa

Figure 4.14 The effects of caprock's inclination and Tensile strength on fracture propagation for tensile strengths of (a) 0.5 MPa, (b) 3.5 MPa, and (c) 5.0 MPa. The images show the model side view.

Figure 4.15 presents the TSA and SSA corresponding to Figures 4.13 and 4.14. A noticeable reduction in Total-SA is observed when the tensile strength increases from 0.5 MPa to 5.0 MPa. This is contributed largely by reduction of the SSA from approximately 25m^2 to 5m^2, while little change in TSA. The induced stress of the fractures in the reservoir and the weak cementation of the natural fractures make the natural fracture faces susceptible to shear slip, thus creating a so-called hydraulic aperture to facilitate fluid leakage into the natural interfaces. Therefore, the magnitude of natural interface tensile strength lower than the main formation, tensile normal stress on the natural fracture may cause its opening and activation in preference to local growth along its original path (Daneshy, 2019). Figure 4.16 shows that the aperture of the HF experiences little changes when the tensile strength increases from 0.5 MPa to 5.0 MPa. However, Figure 4.17 suggests that the fluid can flow more easily along the interface (i.e., X direction) at lower tensile strengths compared to higher values.

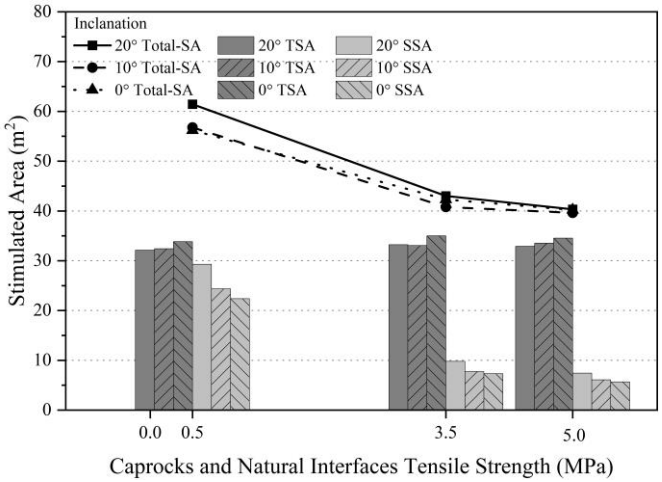

Figure 4.15 The effect of tensile strength and inclination on tension and shear stimulated area (TSA, SSA).

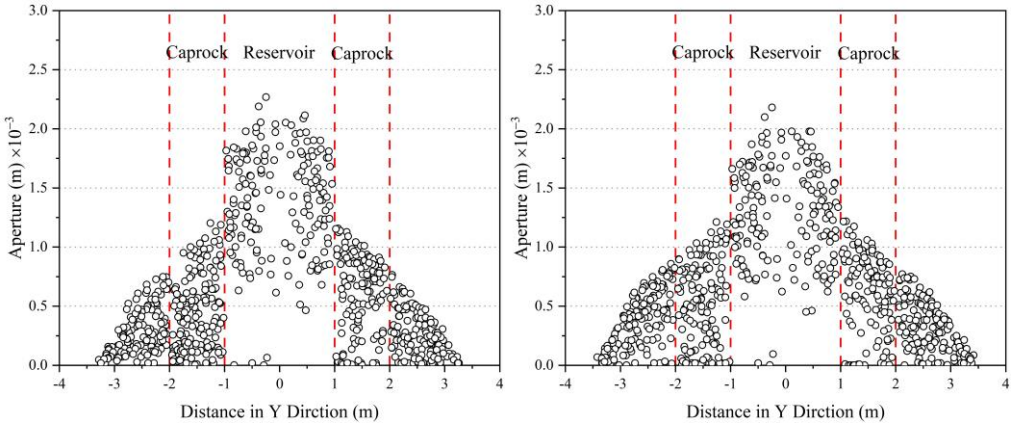

(a) *T*=0.5 MPa **(b) *T*=5 MPa**

Figure 4.16 Profiles of HF aperture in YZ plane at X=-5m for caprock and interfaces' tensile strength of (a) 0.5 MPa, and (b) 5.0 MPa. Wellbore injection point is at Y=0 m.

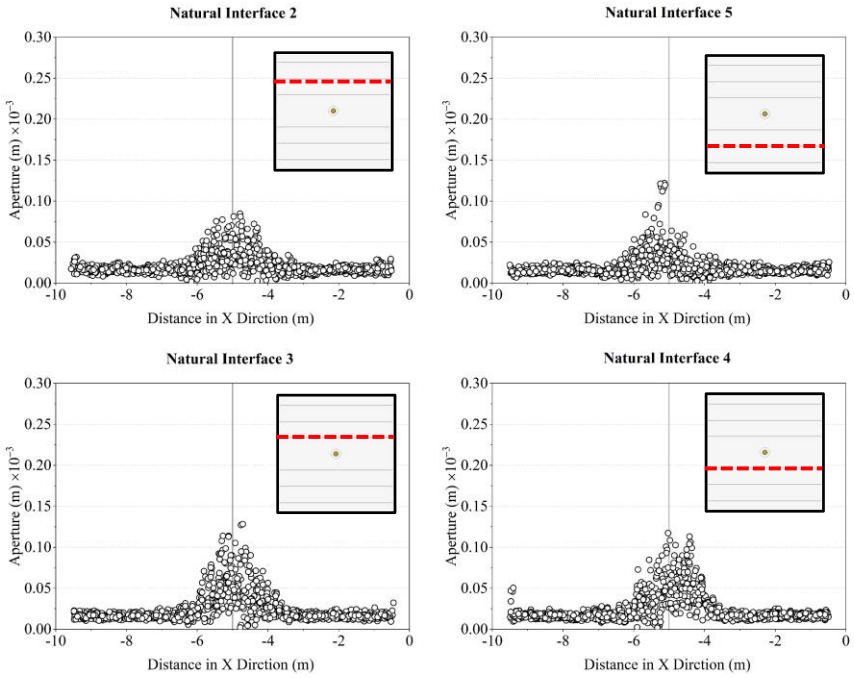

(a) *T*=0.5 MPa

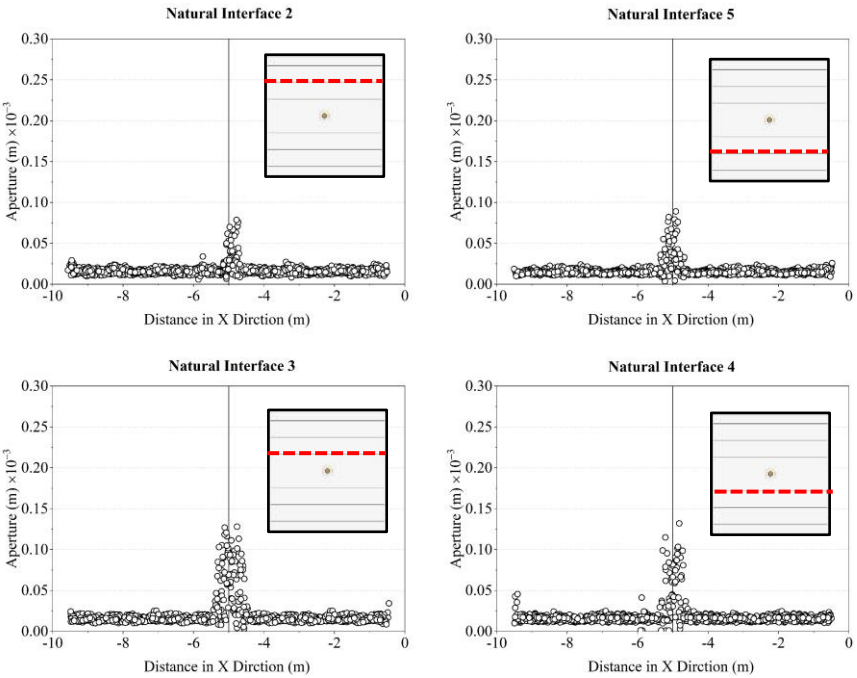

(b) *T*=5 MPa

Figure 4.17 Profiles of natural interface aperture in XZ plane at Z=4m for caprock and natural interfaces' tensile strength of (a) 0.5 MPa, and (b) 5.0 MPa. HF in this plane is at X=-5 m.

4.3.4 Injection Rate

The injection rate (Q) is one of the controllable operational parameters during the HF operation, therefore, it is important to understand its impact on fracture propagation. Five different models with variable injection rates of 0.02 m^3/s, 0.04 m^3/s, 0.06 m^3/s, 0.08 m^3/s, and 0.1m^3/s were considered for simulation purposes. Figures 4.18 and 4.19 shows the results of the aperture as a function of the injection rate. It is seen that as the injection rate increases, the HF aperture in the reservoir increases but the TSA decreases.

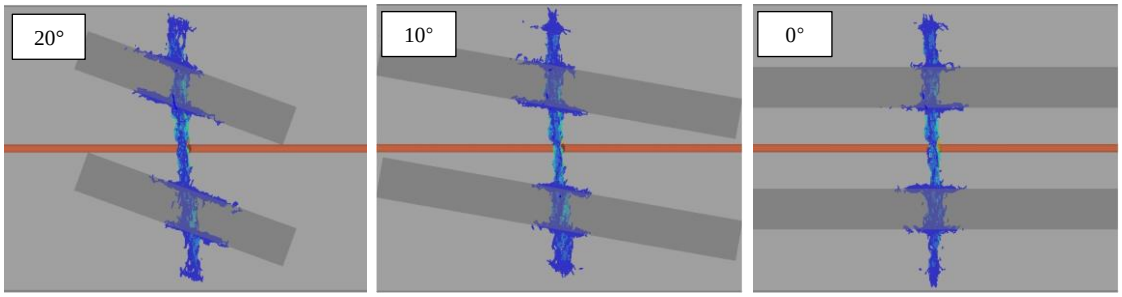

(a) Q=0.02m^3/s

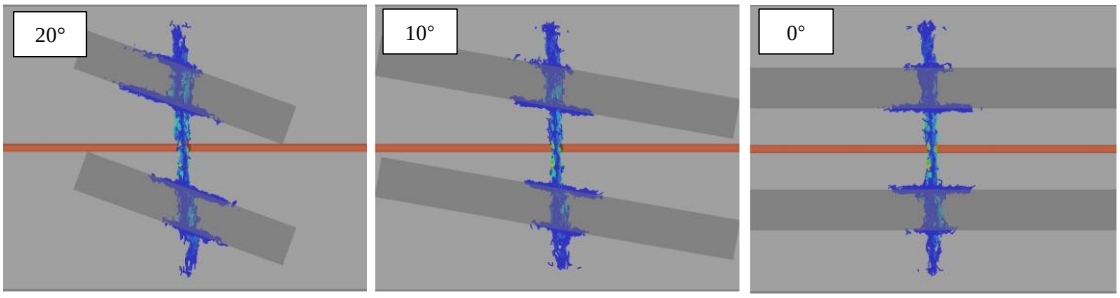

(b) Q=0.04m^3/s

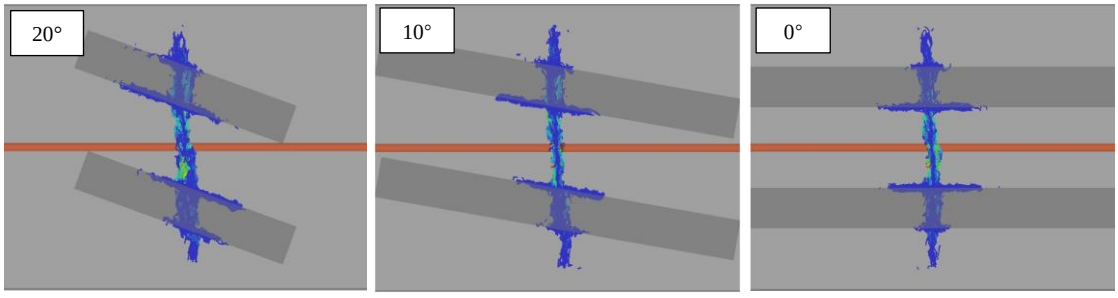

(c) Q=0.06m^3/s

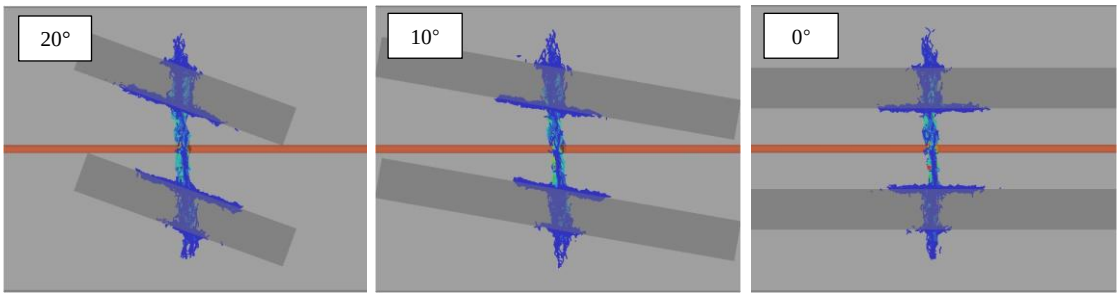

(d) Q=0.08m^3/s

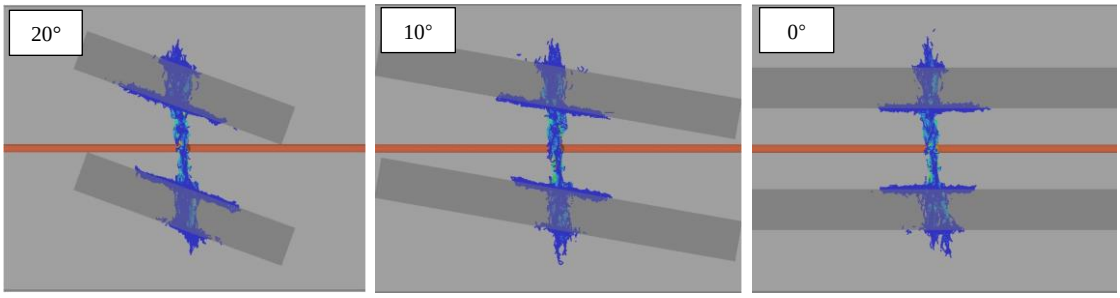

(e) Q=0.1m^3/s

Figure 4.18 The effects of caprock's inclination and fluid injection rate for injection rates of (a) 0.02 m^3/s, (b) 0.04 m^3/s, (c) 0.06 m^3/s, (d) 0.08 m^3/s, and (e) 0.1 m^3/s. The images show the model's front view.

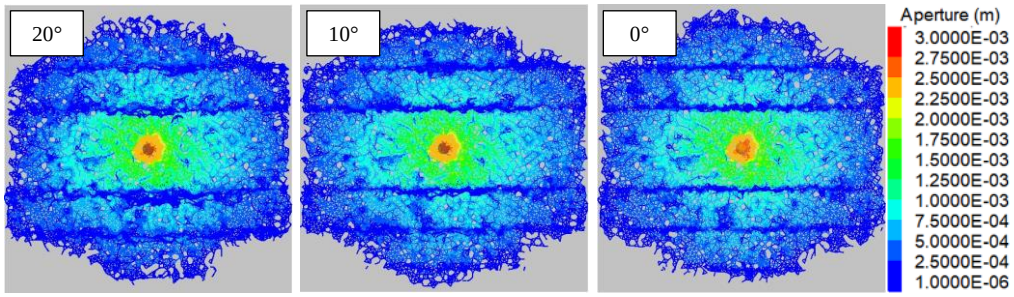

(a) Q=0.02m3/s

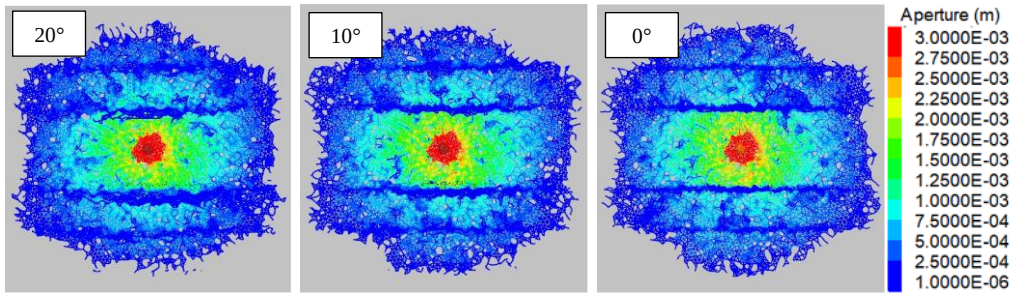

(b) Q=0.04m^3/s

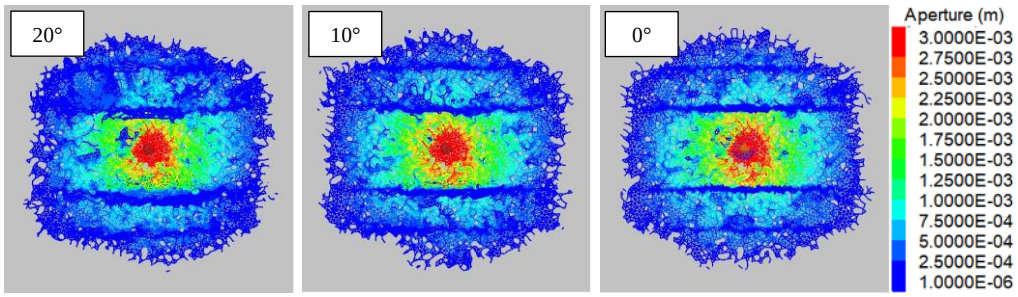

(c) Q=0.06m^3/s

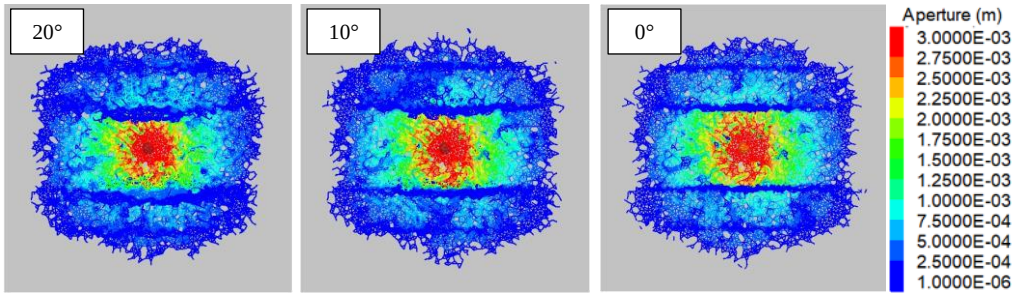

(d) Q=0.08m^3/s

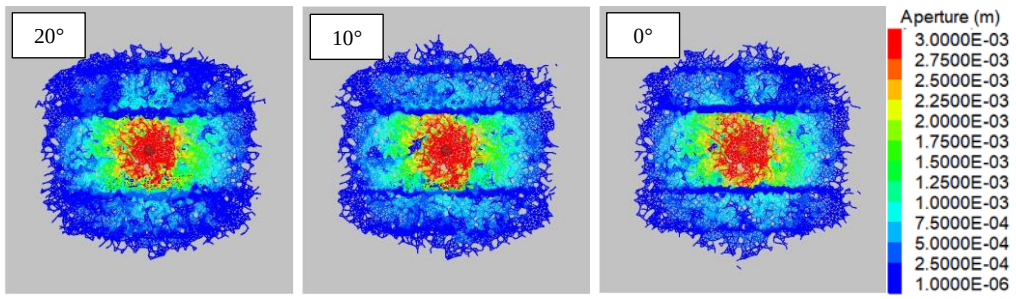

(e) Q=0.1m^3/s

Figure 4.19 The effects of caprock's inclination and fluid injection rate for injection rates of (a) 0.02 m^3/s, (b) 0.04 m^3/s, (c) 0.06 m^3/s, (d) 0.08 m^3/s, and (e) 0.1 m^3/s. The images show the model's side view.

The results in Figure 4.20 indicates that the Total-SA decreases as the fluid injection rate increases and it is seen that this reduction is more contributed by TSA and little impact by SSA. However, the general consensus regarding the effect of injection rate is that an increase in the injection rate contribute to the tensile failure and result in more tensile fracture, whereas a low injection rate favors the formation of natural interfaces shear failure and act as a lubricant to reduce friction and accommodate shearing (Beugelsdijk et al., 2000; Yu et al., 2019; Zou et al., 2016). This can be

explained by Figure 4.21, which illustrates a high injection rate case forms high pressure zone, with a breakdown pressure of 87.6 MPa compared to 27.5MPa, in a short time around the injection point, has a larger aperture in the reservoir layer, resulting in less fluid energy being available to pressurize and extend the fracture in the vertical direction. Also, from the results of Figure 4.22 one can observe that high injection rate results in a greater interfacial extension and wider fractures as compared to the case of lower injection rates. This because the high flow rate HF owns higher hydraulic pressure at the intersection point (x=-5m in Figure 4.22) when it contacts with natural interfaces compare to the lower rate case, hence the HF prefers to propagate along the interface.

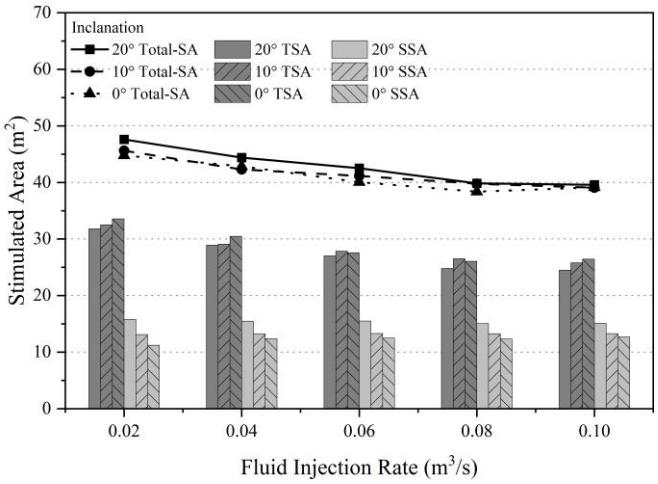

Figure 4.20 The effect of fluid injection rate and inclination on tension and shear stimulated area (TSA, SSA).

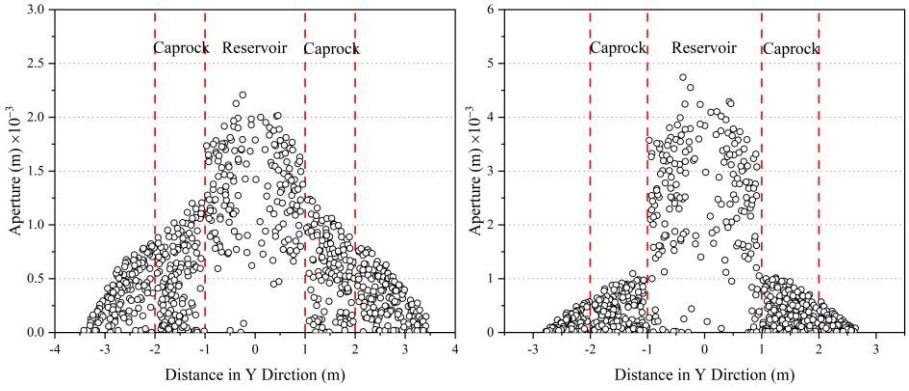

(a) Q=0.02m³/s **(b) Q=0.1m³/s**

Figure 4.21 Profiles of HF aperture in YZ plane at X=-5m for injections rates of (a) 0.02 m³/s, and (b) 0.1 m³/s. Wellbore injection point is at Y=0 m.

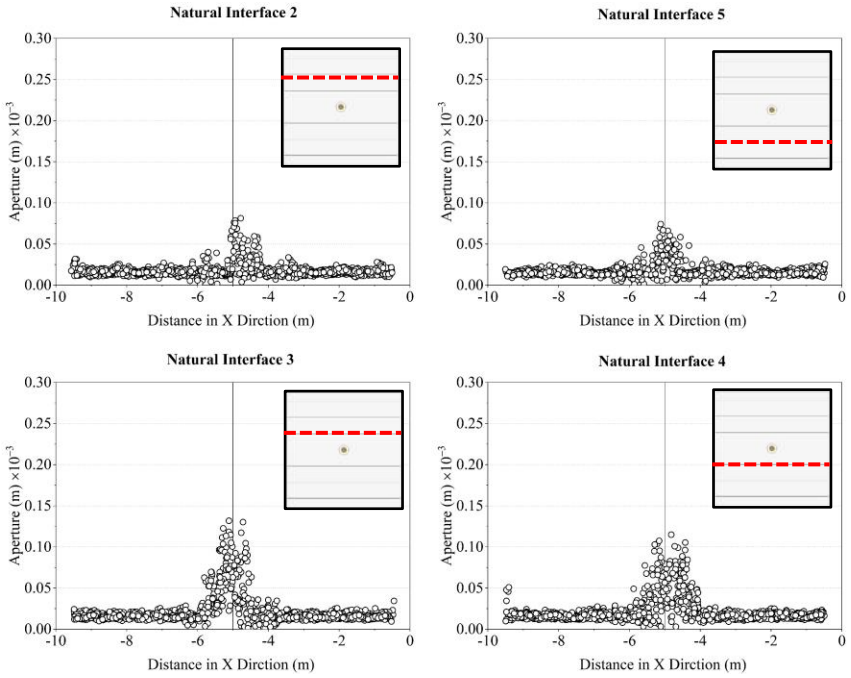

(a) Q=0.02 m^3/s

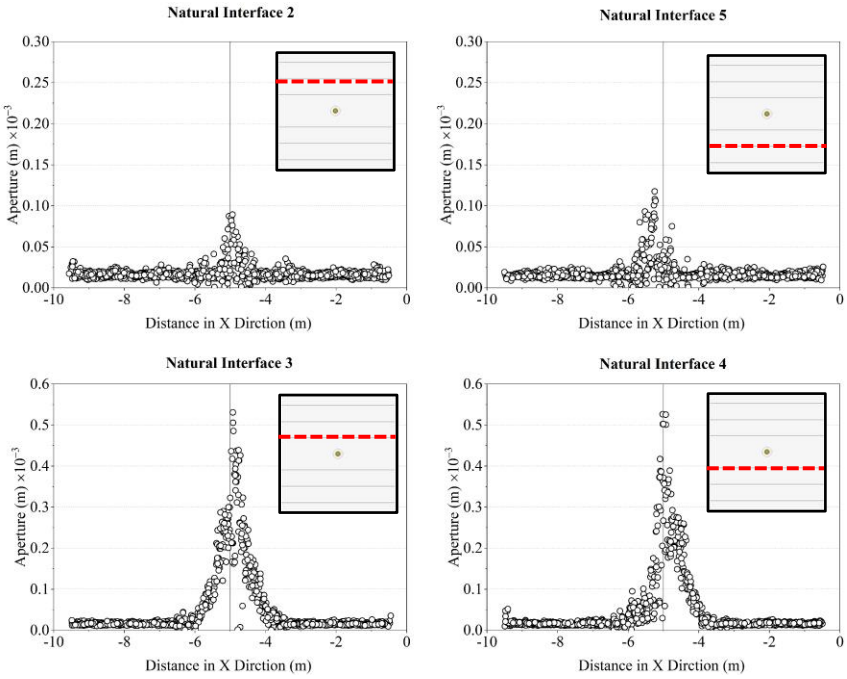

(b) Q=0.1 m^3/s

Figure 4.22 Profiles of natural interface aperture in XZ plane at Z=4m for injection rates of (a) 0.02 m^3/s, and (b) 0.1 m^3/s. HF in this plane is at X=-5 m.

4.4 Discussion

To assess that the above results hold true universally, the considered parameters are transformed into a dimensionless space. The elastic modulus was defined as the ratio of the modulus in the caprock layer to the modulus of the reservoir, denoted as effective Young's modulus (E_E); the ratio of the tensile strength of the natural interface and caprock layer (which was assumed the same in this study) to the tensile strength of the reservoir formation was denoted as effective tensile strength (T_E); the effective stress anisotropy (S_E) was defined as the ratio of the maximum to the minimum horizontal principal stresses; and the effective injection rate (Q_E) was defined as the ratio of the injection rate to the minimum value used in each case. All these dimensionless parameters were calculated to see if they present a meaningful trend for quantitative analysis of the HF propagation and its geometry.

The Stimulated Area Ratio (SAR), defined as the ratio of the TSA to the SSA was also used here. This larger SARs indicate more penetrability of the fracture versus connectivity or larger height (vertical extension) as opposed to horizontal extension. The relationship between the effective Young's modulus and the SAR is presented in Figure 4.23(a), which shows minor changes to the SAR as the stiffness of the caprock increases. This may be explained due to the fact that both TSA and SSA were boosted by fluid pressure that was restricted to enter the stiff caprock. Figure 4.23(b) shows the change of SAR as a function of the effective stress anisotropy. It is seen that SAR increases as stress anisotropy increases, a result which is consistent with the previous findings of this study which showed that high maximum horizontal stress reduces the SSA along the natural interfaces. The relationship between the SAR and the effective tensile strength is presented in Figure 4.23(c). The results of this figure show a significant increase of SAR when tensile strength increases. This is due to the fact that high tensile strengths prevent further opening of the fractures

formed by interfacial slip. Figure 4.23(d) illustrates the effect of injection rate on the SAR, indicating that there is a general tendency for the SAR to decrease as injection rate increases, with slight variations due to change in inclinations. In a nutshell, the above results suggest that the Young's modulus and injection rate favor horizontal propagation of HF (Figure 4.24(b)), whereas stress anisotropy and tensile strength favor vertical propagation of HF (Figure 4.24(a)).

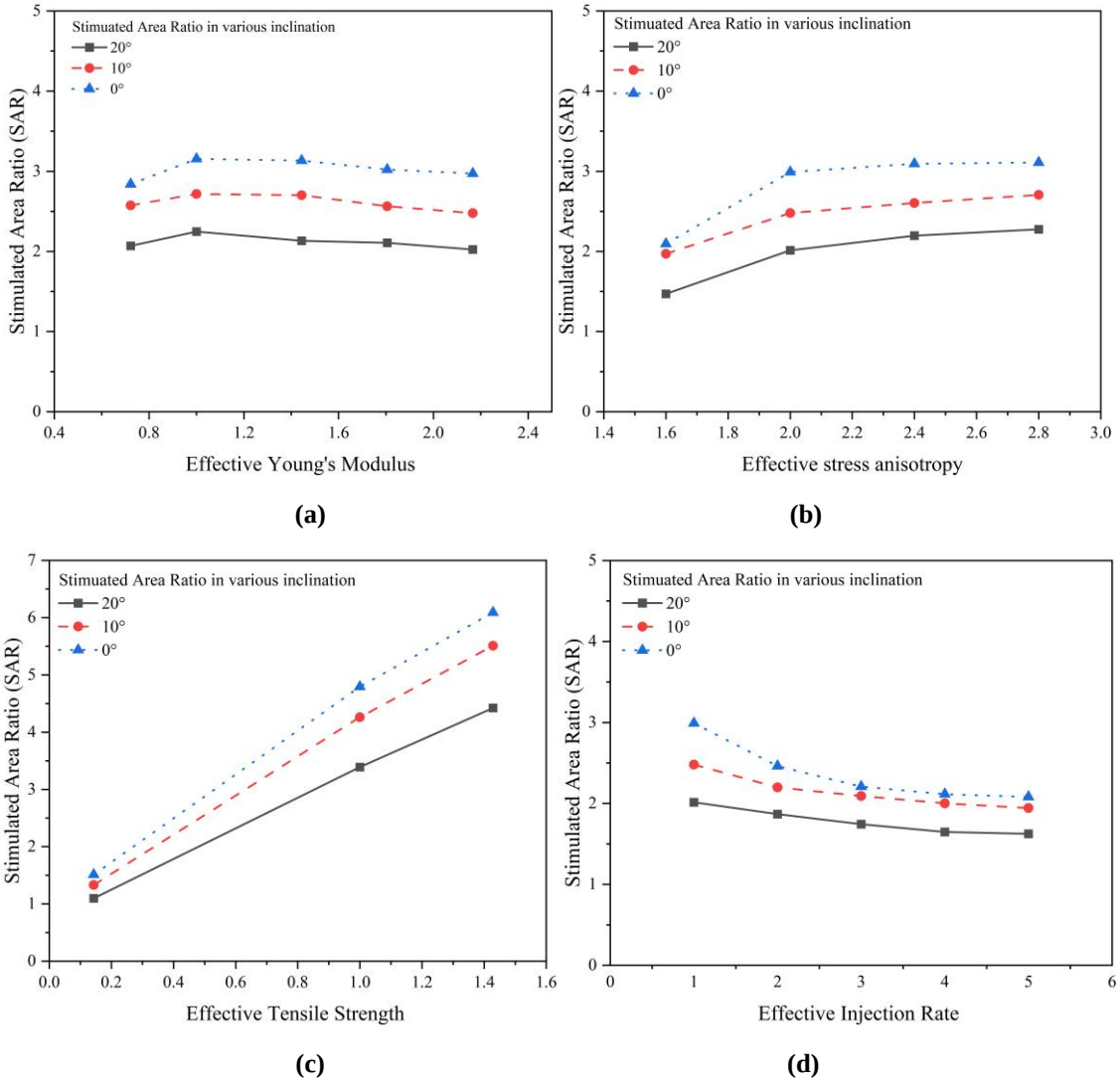

Figure 4.23 The effect of (a) Young's modulus, (b) Stress anisotropy, (c) Tensile strength, and (d) Injection rate on stimulated area ratio (SAR).

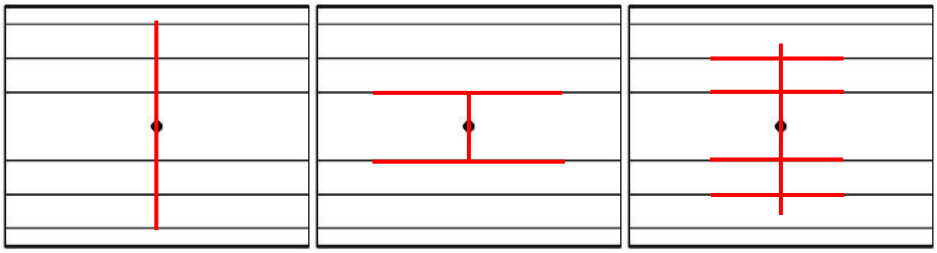

(a) VHF **(b) HHF** **(c) HFN**

Figure 4.24 Illustration of the three HF geometries: (a) a vertical HF, (b) a horizontal HF, and (c) HF network.

The evolution of HF from vertical to horizontal propagation mode can be visualized schematically in Figure 4.25, where the bottom left and top right vertexes represent the vertical hydraulic fracture (VHF) and horizontal hydraulic fracture (HHF) propagation, respectively. In this figure, the bottom right and top left vertices represent the tension and shear stimulated areas, respectively. The transition between VHF and HHF propagation regimes is determined by SAR. This means that the tensile strength and stress anisotropy enable HF to evolve from HHF to VHF via the path close to the SSA, whereas injection rate evolves from VHF to HHF via the path along the TSA. Furthermore, the Young's modulus has an effect on the propagation mode through TSA and SSA, causing it to follow a nearly diagonal path along the rectangle. Further investigation is needed to better understand of the relationships between the SAR, the total stimulated area, and the HF network (HFN).

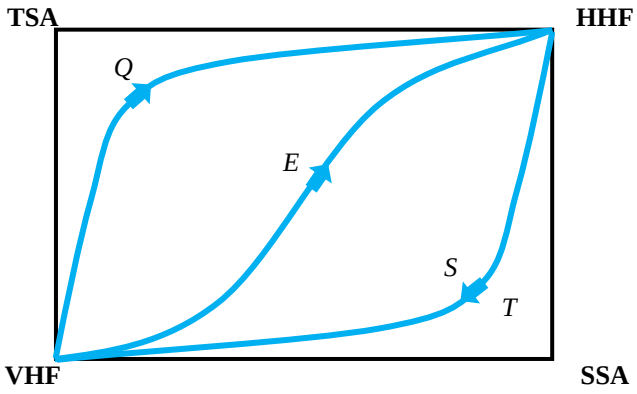

Figure 4.25 Schematic evolution of HF propagation modes in dimensionless space.

4.5 Summary

Based on lattice-based numerical simulation of HF propagation in a laminated model presented in this chapter, the following conclusions were drawn:

(1) Higher caprock Young's modulus promotes HF vertical and horizontal extension. Higher vertical stress anisotropy inhibits HF horizontal extension. Higher tensile strength of the interface and caprock prevents HF horizontal propagation. A higher injection rate promotes HF width growth in the reservoir.

(2) The tension stimulated area (TSA) and shear stimulated area (SSA) were used to determine the vertical and horizontal extendibility of HF. The TSA shows HF's ability to penetrate the interface and propagate vertically, whereas the SSA represents the ability of HF to form interface slippage or horizontal propagation of the fracture. These two parameters can quantitatively describe the behavior of HF propagation when it interacts with natural interfaces.

(3) The ratio of TSA to SSA, known as the stimulated area ratio (SAR), was used as a parameter to show how HF propagation transition occurs between vertical and horizontal directions. The greater the SAR, the greater the HF penetrability. A dimensionless space was used to demonstrate how mechanical and operational factors affect the propagation of HFs along different pathways in a laminated formation.

In the next Chapter, an integrated model will be proposed to predict the hydraulic fracture stimulated potential in complicated geological condition.

Chapter 5

Multi-Cluster Hydraulic Fracture Propagation Pattern in Laminated Formations

5.1 Introduction

Hydraulic fracture operation is the prime technology in stimulation of unconventional reservoirs, including shale plays. In laminated reservoirs such as shales, HF treatment is affected as a function of several factors such as principal stress difference, fracturing fluid viscosity, pumping rate, and formation properties . Many scholars have studied the geometry of a HF initiated from a single cluster in an isotropic medium, with only few works considering the medium as laminated and propagation from multi-clusters, which is more representative of real field operations. In this paper, XSite, a lattice numerical simulator, was used to study the multi-cluster HF propagation modes in a laminated reservoir assuming bedding properties. The effect of reservoir formation as well as caprock and the interface properties will be studies. Simulation results showed that differential horizontal stresses, cluster spacing, and fracturing injection rates significantly affect the HF propagation in laminated reservoirs. High horizontal stress difference is favorable for the HF to penetrate the upper and lower barriers but detrimental for its propagation along the horizontal planes to communicate and form a complex fracture network. The simulation results also showed that the effect of different layers' Young's modulus on fracture height is complicated. When a

fracture enters from a high to a low stiffness layer it can easily cross the interface. Since the tensile strength of the rock influences both fracture initiation and propagation, a low tensile strength layer is more favorable to form complex fracture networks compared to a high tensile strength barrier. It was observed that larger cluster spacing is beneficial for crossing the barrier, whereas less spacing results in fractures to communicate with the interfaces, due to the stress shadow, and generate more complex fracture networks. Although increasing the injection rate favors fracture crossing the barrier, an extremely high injection rate may only increase the fracture height without effectively communicating different layers to form fracture network. An analytical hierarchy process (AHP) based mathematical model was developed considering six most significant parameters in HF propagation in laminated formations to evaluate the stimulation potential based on their different impact on stimulated reservoir volume (SRV). The analysis indicated that stimulation potential index increases with the increase of stimulation area and can be used to predict the potential production in laminated reservoirs.

5.2 Model Setup

Figure 5.1 represents the model used in this study. The dimensions of the model in length (along the X-axis), width (along the Z-axis), and height (along the Y-axis) are 10m, 8m, and 8m, respectively. Six zero-thickness and 1m apart interfaces are used in the model to characterize the cemented interface between layers. Two homogeneous layers with 1 m thickness are assigned between the two interfaces to characterize the caprocks above and below the reservoir formation. Here, the barrier layer and lamination inclination of zero is the horizontal layer, whereas 90° refers to a vertical plane. The reservoir formation of 2 m height is also shown in Figure 5.1. The magnitude of the principal stresses are σ_h=4MPa, σ_H =10.8MPa, and σ_v =17.6 MPa, in X, Y, and

Z directions, respectively. A horizontal wellbore is located at the center of the model, along the negative direction of the x-axis, parallel to the direction of the minimum horizontal principal stress. Three clusters are placed at 3.5m, 5m, and 6.5m from the reference point in the X direction and initial cracks are placed at these points as notches to facilitate the initiation of HF. The simulation is initially run in a mechanical model for 0.1 s (numerical time) to achieve initial model equilibrium and continues in the fluid-solid coupling mode after starting the fluid step and keeping fluid injection into each cluster at a constant rate afterward.

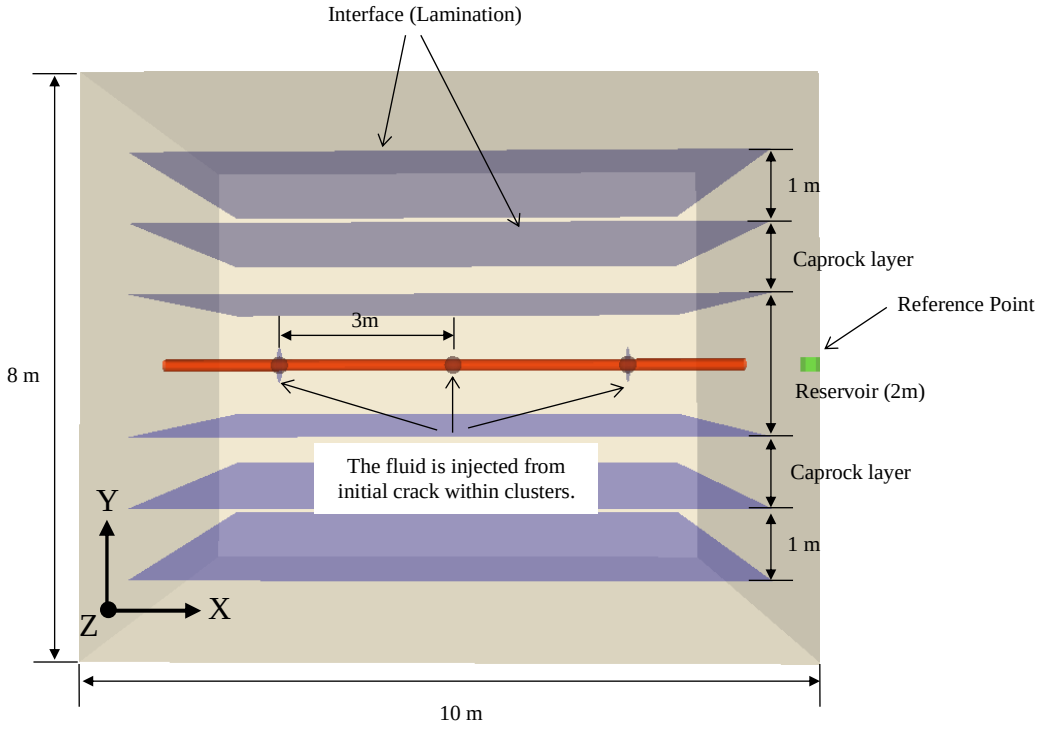

Figure 5.1 The XSite model geometry used in this study.

The mechanical properties of the reservoir formation and the caprocks are shown in Table 5.1. The injected fluid is Slick water with a viscosity of 0.001Pa.s. It is difficult to obtain the interface data, so the tensile strength, cohesion, and internal friction angle of the bedding interface in the initial model were set to be 2.1 MPa, 6 MPa, and 30°, respectively, with reference to the data from previous studies (Liu et al., 2019).

Table 5.1 Mechanical properties of formations and barriers.

Parameters	Reservoir	Caprocks	Natural Interface
Tensile strength, T_0, psi (MPa)	3.5	3.5	2.1
Friction angle, θ, (°)	26.565	26.565	30
Uni-axial compressive strength, UCS, (MPa)	79.5	79.5	-
Young's modulus, E, (GPa)	27.2	60	-
Uni-axial Poisson's ratio, v	0.221	0.221	-
Density (kg/m^3)	2600	2600	-
Porosity, ϕ, (%)	14.7	14.7	-
Permeability, K, (m^2)	1.7×10^{-15}	1.7×10^{-15}	-
Cohesion, S_0, (MPa)	-	-	6

5.3 Results and Analysis

In this section, the effect of formation properties as well as operational parameters on HF propagation will be simulated numerically and the results are presented. The conception stimulated area (SA) is proposed to quantitatively evaluate the fracture area generated by HF, the shear-SA is defined as the area of natural discontinuities undergo shear slippage, whereas the tensile-SA is the area of induced tension fractures in mass.

5.3.1 Young's Modulus

In this section, the effect of cap rocks Young's modulus on hydraulic fracture propagation was investigated. As shown in Figure 5.2, results of SA as a function of the Young's modulus of the caprocks and the deviation of the lamination planes. The total simulated area consists of tension stimulated area (TSA) and shear stimulated area (SSA). One can find from Figure that the increased TSA contributes more to the increased total stimulated area at various inclination, whereas the shear stimulated area remains nearly unchanged. This means that as Young's modulus

rises, the hydraulic fracture tends to propagate vertically rather than along the bedding interface, i.e., easier to cross the laminations. In order to prove this perspective, a detailed comparison between low and high Young's modulus caprock layer models are shown in Figure 5.3, which shows the section view of three hydraulic fractures propagation and their interaction with natural interfaces as well as caprock layer in laminated reservoir. As we can see in the Figure 5.3(a), hydraulic fractures prefer extending a short distance along the interfaces when they contacted natural interfaces, then reinitiate on the other side of interfaces. However, when hydraulic fractures propagation in high Young's modulus as shown in Figure 5.3(b), the two sides fractures propagate deviated from original direction because of stress shadow effect but without any offset happens during the whole interaction process. Also, the high modulus caprock layer case shows a longer and thinner fracture geometry. This is because Young's modulus qualifies the relationships between tensile stress and axial strain in linear elastic region of a material, hence it is difficult to initiate and propagate for hydraulic fracture in low Young's modulus formation (ductile formations) due to additional energy absorbed by plastic deformation and strong fluid-rock interactions (Wang, 2015). As a result, a high Young's modulus of the caprocks is advantageous for vertical hydraulic fracturing penetration in a laminated reservoir.

Also, since the low caprock layer deviation from horizontal prone hydraulic fracture crossing the natural interfaces, thus reduces the possibility of interface slippage result in less SSA but more TSA. Moreover, As shown in Figure 5.4, the vertical penetration of the hydraulic fracture morphology changes significantly with the change in inclination while maintaining the caprock's Young's modulus at 60Gpa. The penetration pattern does not change much as the inclination increases from 0 to 10°, whereas it appears to be unilaterally and bilaterally inhibited when the inclination approaches 15° to 20°, as shown in Figures 5.4 (d) and (e).

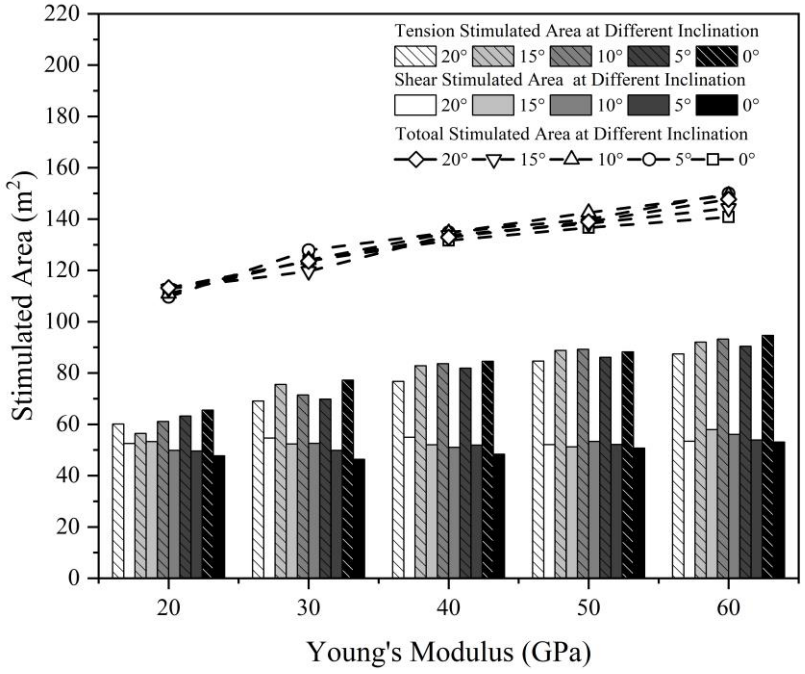

Figure 5.2 Stimulated area with different Young's modulus at different interface inclinations.

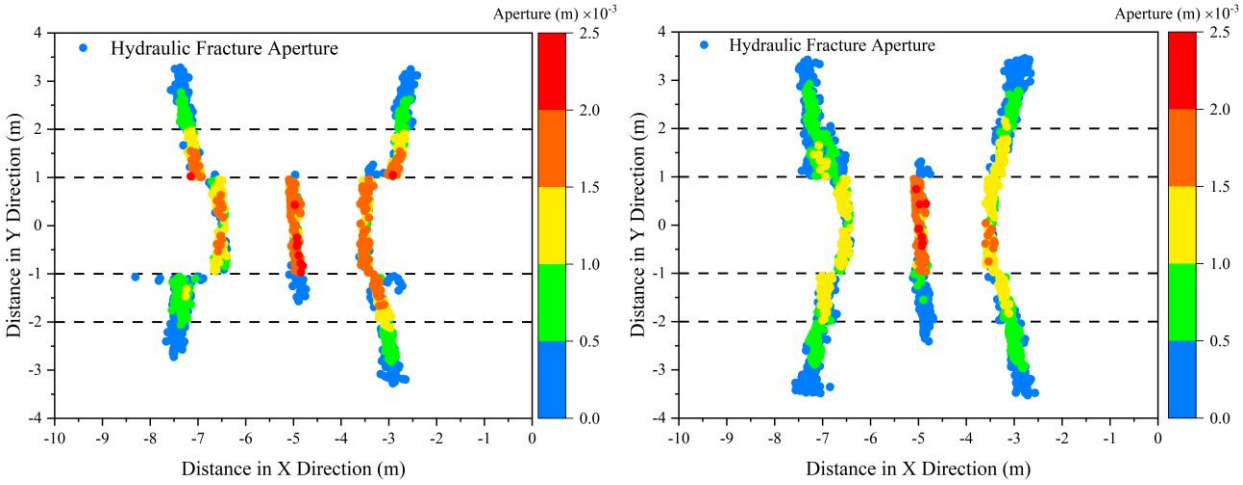

(a) *E*=20 MPa **(b) *E*=60 MPa**

Figure 5.3 Hydraulic fracture aperture when caprock's Young's modulus of (a) 20 MPa, (b) 60 MPa.

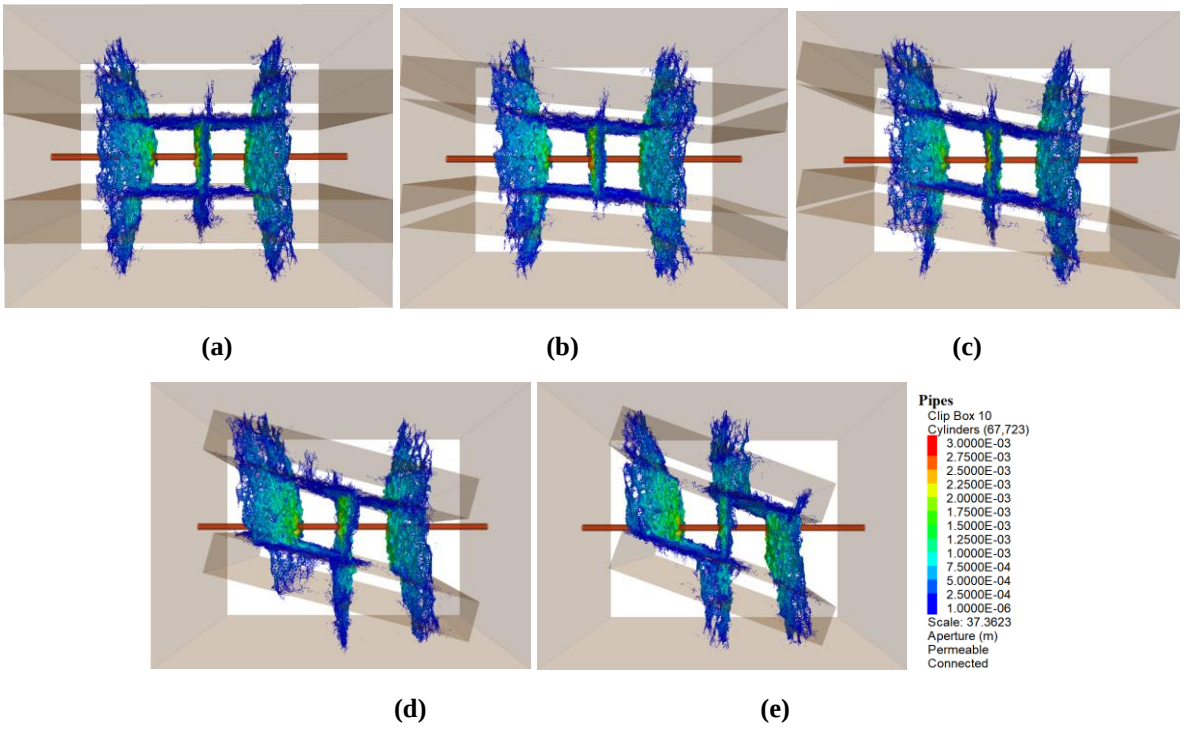

Figure 5.4 Variation of fracture morphology with the change of lamination inclination when Young's modulus is 60 MPa for different interface inclinations of (a) 0°, (b) 5°, (c) 10°, (d) 15°, and (e) 20°.

A further study was done to see how the difference in Young's modulus affect fracture propagation at a particular inclination of 0°, as an example. The results presented in Figure 5.5 show that in this case, the middle fracture is prone to vertical propagation as Young's modulus increases. When the caprock's Young's modulus is less than reservoir's, the middle fracture is completely confined between the upper and lower barriers, resulting in the "工" type fracture, as shown in Figure 5.5 (a). On the other side, when the caprock's Young's modulus is more than reservoir's, the middle fracture partial crossing the natural interface into the caprock layers, as shown from Figure 5.5 (b) to (e).

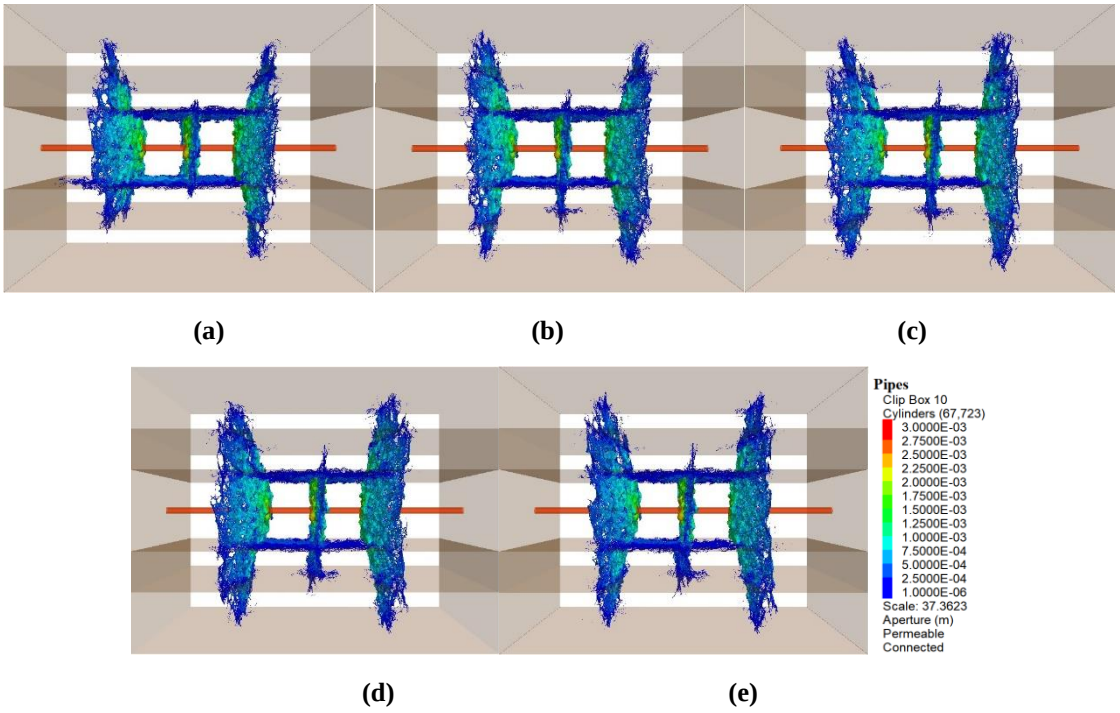

Figure 5.5 Variation of fracture morphology with the change of Young's modulus for barrier inclination of 5° and different barrier Young's moduli of (a) 20 GPa, (b) 30 GPa, (c) 40 GPa, (d) 50 GPa, and (e) 60 GPa.

5.3.2 Vertical stress anisotropy

To examine the effect of the vertical stress anisotropy on fracture propagation, the minimum horizontal principal stress was maintained at 5 MPa, while the principal vertical stress was varied from 5 MPa to 8 MPa, 10 MPa, 12 MPa, and 14 MPa. This implies differential stresses of 0 MPa, 3 MPa, 5 MPa, 7 MPa, and 9 MPa, respectively.

Figure 5.6 shows that at differential stress of 0 MPa, the fracture stimulated area grows with decreasing inclination and reaches a minimum of 0° inclination. The effect of inclination on the stimulated area is gradually decreasing as differential stress increased, and the total SA becomes approximately 145m^2 at an inclination of 0°. When the inclination is constant, however, the total stimulated area does not increase monotonically as the differential stress increases. As shown in Figure 5.7, when the differential stress increases from 0MPa to 9MPa, for example, the total

stimulated area increased significantly, while the tension stimulated area and shear stimulated area present an increasing and decreasing trend, respectively.

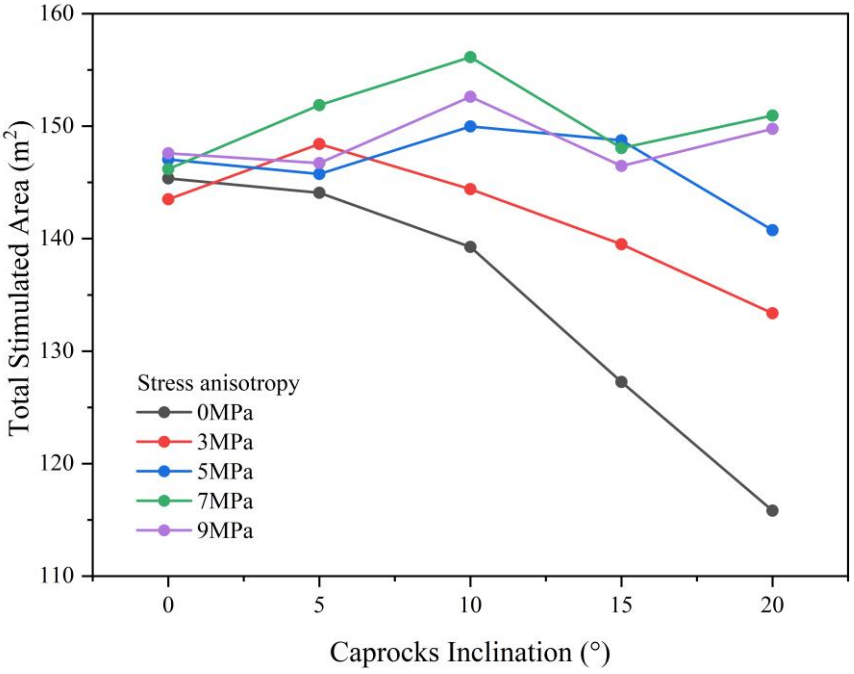

Figure 5.6 Total Stimulated area for each interface inclination under different inclination.

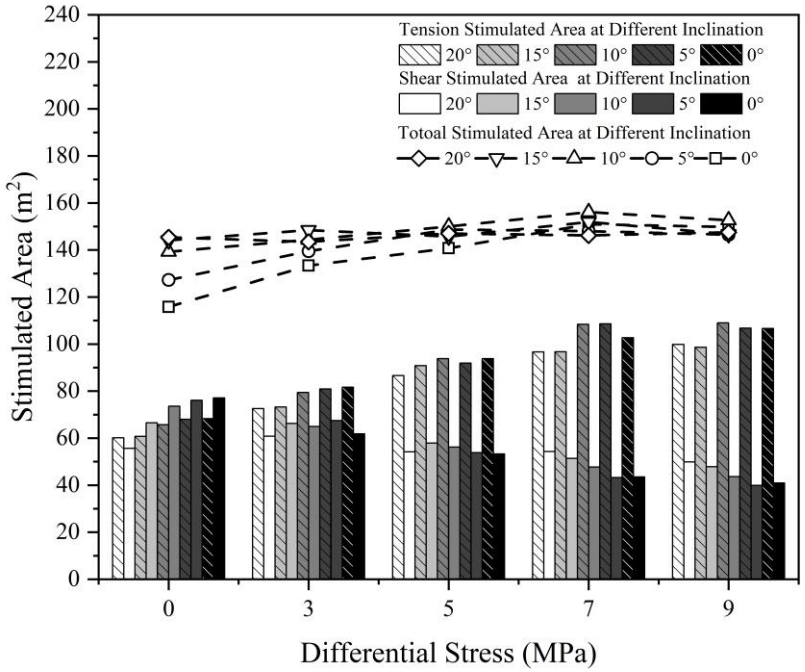

Figure 5.7 Total Stimulated area for each interface inclination under different stress anisotropy.

In the next step, the lamination inclination was fixed to 90° in the model to analyze the effect of the differential stress changes from 0 MPa to 9 MPa on fracture morphology. The simulation results are shown in Figure 5.8.

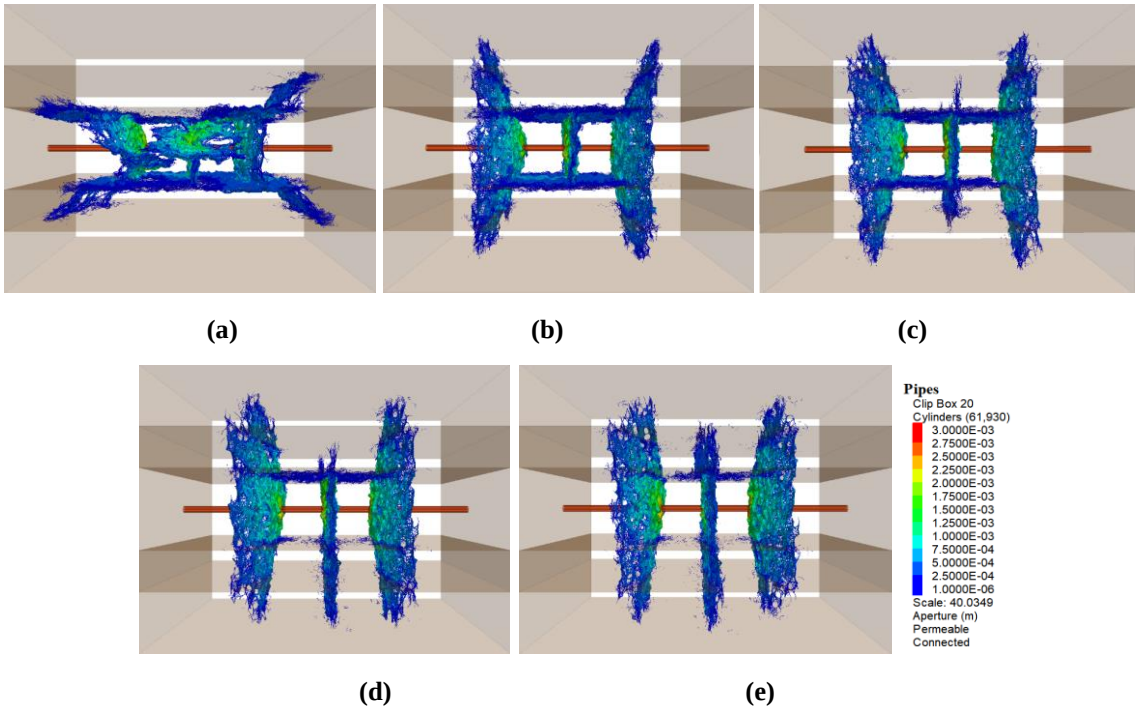

Figure 5.8 Variation of fracture morphology as a function of vertical stress anisotropy and interface inclination of 90° and stress differential of (a) 0MPa, (b) 3 MPa, (c) 5 MPa, (d) 7 MPa, and (e) 9 MPa.

The change in the stress difference, as shown in Figure 5.8, has a significant impact on the fracture extension pattern. According to a previous study (Hossain & Rahman, 2008), the fracture has not yet penetrated the upper and lower barriers before torsional extension occurs at a stress difference of 0 MPa. That is because when the differential stress is 0, the induced stresses generated at the beginning of fracture extension dominated and easily change the stress magnitude and direction at the fracture tip, resulting in the severe torsional phenomenon shown in Figure 5.8 (a). When the differential stress reaches 3 MPa, the hydraulic fracture no longer twists; in the meantime, fractures on both the left and right sides penetrate the caprocks, while the middle fracture is contained. The

middle fracture penetrates further into the caprocks as the differential stress increases from 5 to 9 MPa, with nearly complete penetration when the differential stress reaches 9MPa. This phenomenon occurs because the differential stress gradually increases, and the induced stress generated by the fracture extension is already difficult to influence the magnitude and direction of the stress at the crack tip, making it difficult for the fracture to deflect in the propagation and thus reducing the complexity of the entire fracture network, which is easy to form a single, independent vertical fracture. At the same time, it can be seen that as the stress difference increases, the left and right crack deflection decreases significantly.

The simulation results show that at 7 MPa differential stress and 10° inclination, fractures reach their maximum vertical extension and widespread communication along interfaces occur to form a complex fracture network, resulting in the maximum SA. HFs are more likely to penetrate the caprocks if there is large differential stress. Extreme differential stress, on the other hand, consistently reduces the complexity of fracture networks and makes it more likely to form a single fracture plane, resulting in a negative impact on the SA.

5.3.3 Tensile strength of Reservoirs and Caprocks

The tensile strength has a significant impact on fracture initiation and extension pattern . Numerous experimental results show that the interaction between the HF and the interface impacts the morphology of the induced fracture. As a result, in laminated reservoirs, activation of the interface is required for the formation of a complex fracture network in both vertical and lateral directions. The interaction between HF and natural interface results in different mechanisms like crossing, arresting, and opening(Sarmadivaleh et al., 2014). Furthermore, according to sedimentology, the barrier in laminated reservoirs is known to exert significant control over hydrocarbon transport. In this study the barrier's lithological properties are assumed to be the same. Here, we examine the

effect of the tensile strength of the caprock and the interface on the vertical extension of HF. The reservoir rock tensile strength in this study is 3.5 MPa, while the caprocks and interface tensile strengths synchronize vary from 0.5 MPa to 3.5 MPa and 5 MPa, respectively.

As shown in Figure 5.9, the total SA decreases significantly as the tensile strength of both the caprocks and the interface increases, especially between 0.5MPa and 3.5MPa range. Figure 5.10 shows that the total SA is generally large when the tensile strength is 0.5 MPa, which is less than the reservoir tensile strength of 3.5MPa. Meanwhile, the maximum SA is expected to be at 75° inclination, regardless of the tensile strength of the caprocks and interface.

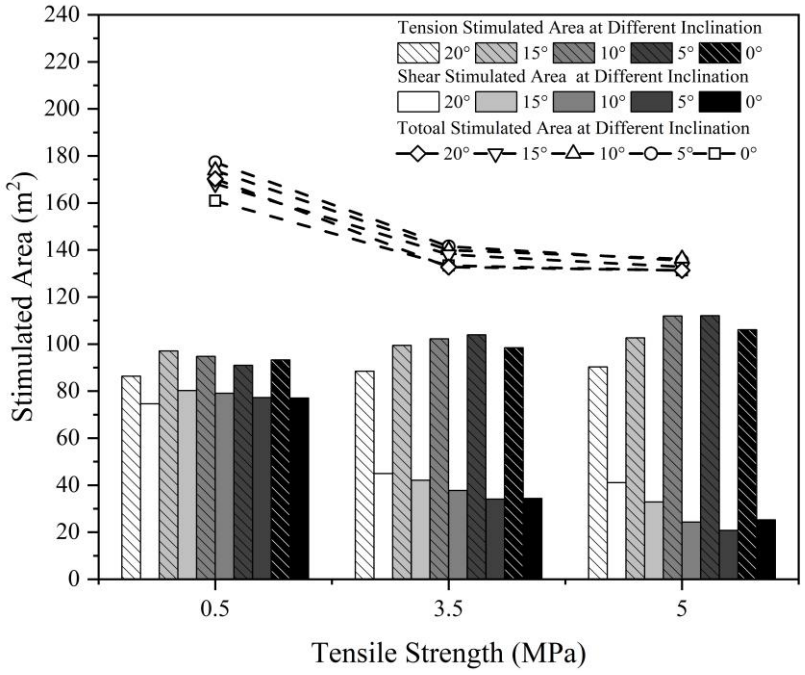

Figure 5.9 Relationship between stimulated area and caprocks tensile strength and different interface inclinations.

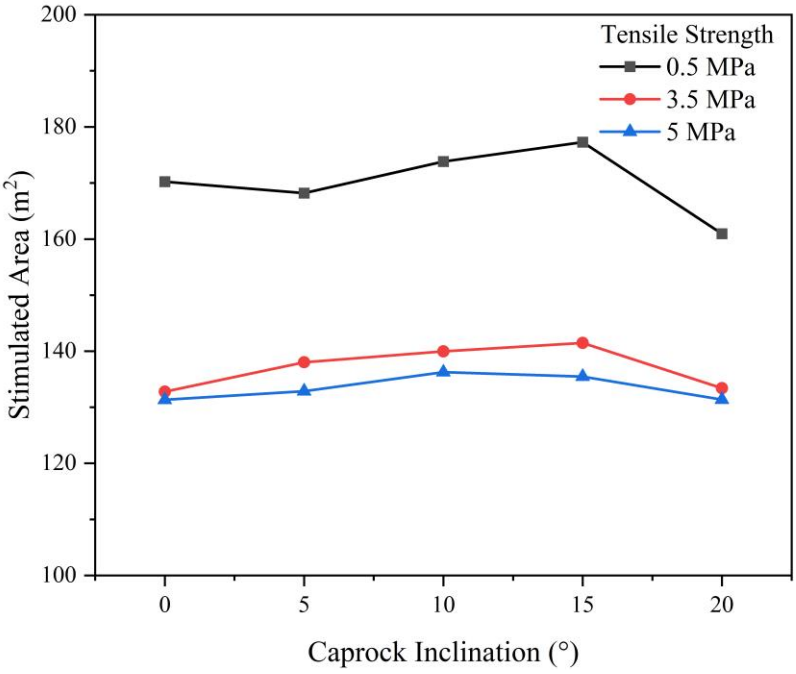

Figure 5.10 Relationship between stimulated area and interface inclination as a function of the tensile strength of the caprock and interface.

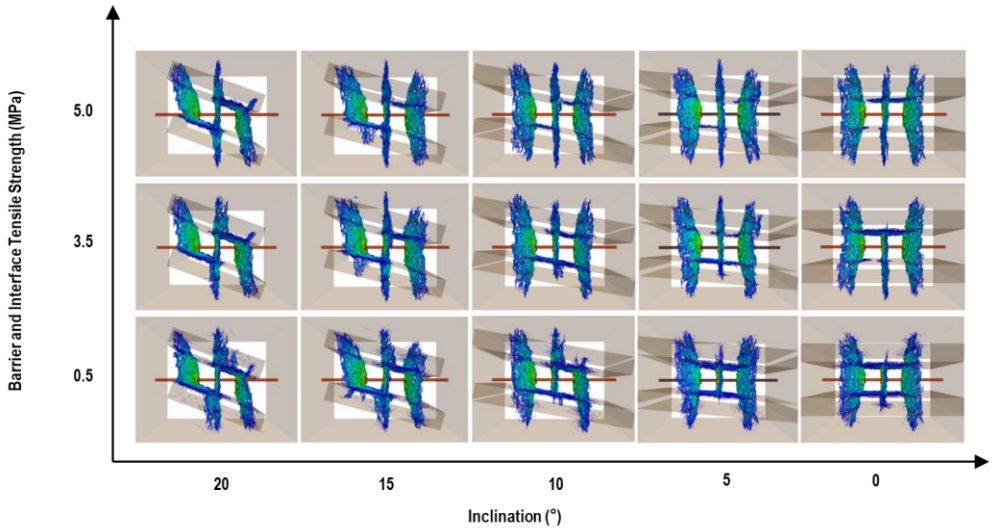

Figure 5.11 Variation of fracture morphology for different caprocks tensile strength and interface inclinations.

The effect of inclination and tensile strength on fracture morphology is shown in Figure 5.11. At 70° and 75° inclination, two sides of the hydraulic fracture appeared to be unilaterally restricted, but this disappeared at 80° inclination. Moreover, higher tensile strength indicates more stable rock

mass when compared to the caprocks and interface with lower tensile strength. So, when the HF transits to the low strength caprock from the higher strength reservoir, then it is more likely to turn and propagate along the interface. Conversely, it is more likely to form a single vertical fracture.

5.3.4 Cluster Spacing

Previous research has reported that a small cluster spacing causes significant interaction between multiple HFs (X. Liu et al., 2020; Wang, 2016). Those studies, on the other hand, rarely consider the impact of the reservoir/caprocks interfaces on multi-cluster hydraulic fracture propagation. Three different cluster spacings of 1m, 2m, and 3m were considered in this study to examine their effect on fracture propagation. In addition, due to model size constraints, inclination was limited to 10°, 5°, and 0°. The rest of the parameters are the same as those reported in Table 5.1.

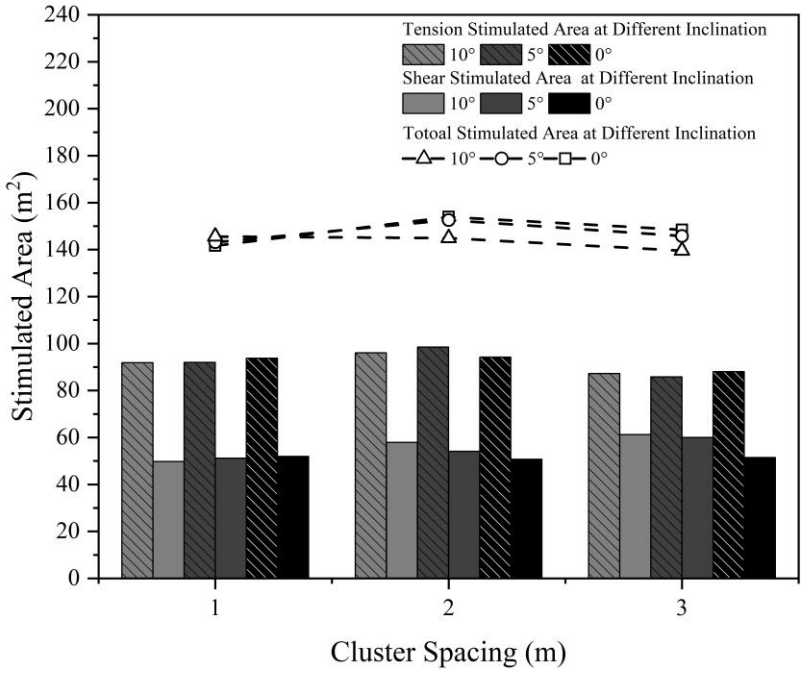

Figure 5.12 Variation of fracture stimulated area as a function of the interface inclinations at different cluster spacings.

As can be seen in Figure 5.12, the SA for the three cluster spacings does not differ significantly, and as the interface inclination increases, they gradually approach the same value of 145 m^2. For

example, at a 1 m cluster spacing, the total SA increases slowly as the inclination changes and peaks at 0°. The total SA tends to decrease with increasing inclination for cluster spacing of 2m and 3m, reaching a maximum at an inclination of 10°. A small cluster spacing, in particular, has a significant impact on fracture propagation due to the high stress shadow, resulting in the middle fracture twisting completely along the interface. In a laminated reservoir, fracturing with a larger cluster spacing favors vertical propagation with less communication with the interface. Furthermore, the 2m spacing shows the most stimulated area across all barrier inclination cases, owing to the ability of the middle fracture to communicate with the interface while still maintaining good caprocks penetration in an appropriate fracture spacing. The fracture SA reaches its maximum at a cluster spacing of 2m and an inclination of 10°, according to the simulation results. The stress shadow impact can be moderated with proper cluster spacing, allowing the middle fracture to communicate with the fractures on both sides and maintain good vertical penetration.

Since cases of inclination at 10° have sufficient differentiation in SA, further investigation was dedicated on the effect of the variable cluster spacing under a specific inclination on fracture propagation in a laminated reservoir. The results of this attempt are shown in Figures 5.13 and 5.14. Figure 5.13 illustrates that at a specific cluster spacing, higher interface inclination promotes easier interface slippage to connect HF with the natural interface in the horizontal direction. Figure 5.14 demonstrates that at a particular interface inclination, larger cluster spacing facilitates the HF to penetrate into the natural interface in the vertical direction.

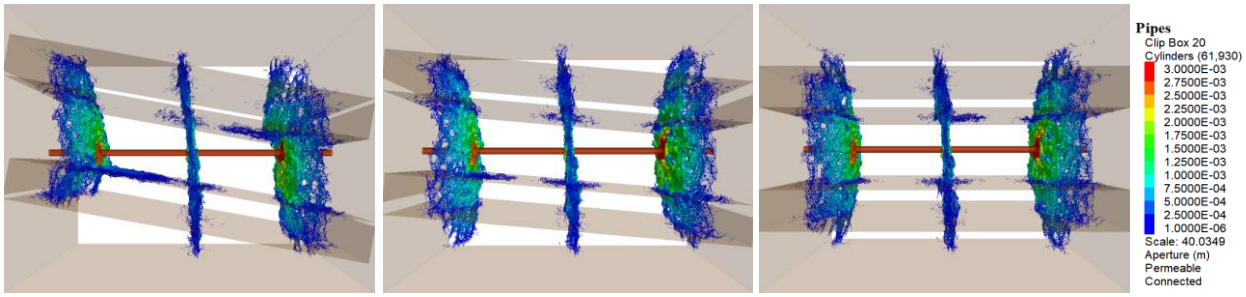

(a) **(b)** **(c)**

Figure 5.13 Variation of fracture morphology with the change of interface inclination for cluster spacing of 3m at interface inclination of (a) 10°, (b) 5° and (c) 0°.

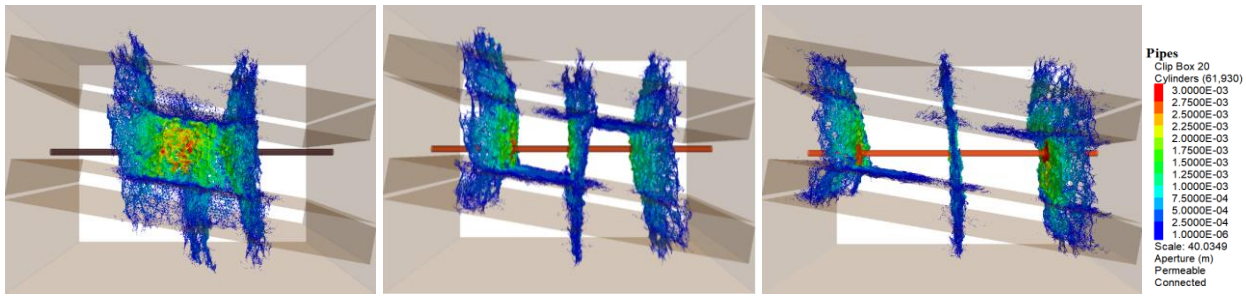

(a) **(b)** **(c)**

Figure 5.14 Variation of fracture morphology for different cluster spacings at an interface inclination of 10° for cluster spacings of (a) 1m, (b) 2m and (c) 3m.

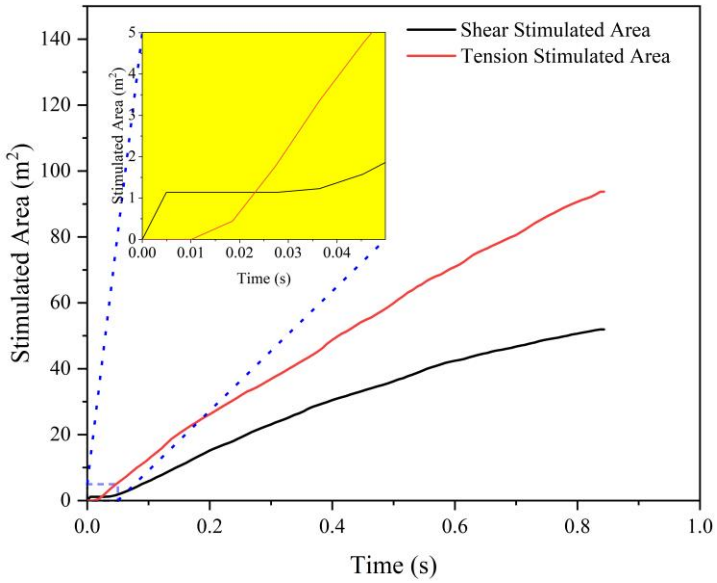

Figure 5.15 Shear and tension stimulated area for the case of interface inclination of 0° and cluster spacing of 1m.

Previous studies have shown that in real fracturing process, the shear strength of the rock is mainly required to overcome at the early stage of fracturing in formation or when the fracture encounters the laminated surface or microcrack, and then the tensile strength is the main inhibition to overcome during the stable propagation stage of fracture. A diagram of shear and tension SA shown in Figure 5.15 confirms this. It is seen that in the case of small cluster spacing, when the fracturing fluid is injected and the fracture starts to initiate, stress shadow is generated. At this time the fracture on both sides turns and creates shear failure, that causes the shear stimulated curve to grow rapidly from the initial moment and gradually becomes flat. On the other side, the tension stimulated area curve shows that the initial stage after crack initiation is not dominated by tensile failure. After a while, the fracture tension extension dominated the development of the SA.

5.3.5 Injection Rate

Fluid injection rate is the least expensive parameter to control fracturing efficiency. The effect of injection rate on multi-cluster fracture propagation patterns and formation of the SA is investigated.

The injection rate was changed from $0.02m^3/s$ to $0.04m^3/s$, $0.06m^3/s$, $0.08m^3/s$, and $0.1m^3/s$, respectively. The results are presented in Figure 5.16. This Figure shows that the injection rate of $0.04m^3/s$ presents a maximum total SA, at nearly most interface inclinations. In Figure 5.17, the injection rate is set to $0.06m^3/s$ to investigate how inclination affects fracture morphology. Even though these five cases have similar SA values, they have different fracture propagation modes. The vertical fracture morphology does not differ much when the fracturing fluid injection rate is maintained at $0.06m^3/s$ when the interface inclinations are 0°, 5°, and 10°, however, the difference is noticeable when the interface inclination is increased to 15° and 20°. When compared to a low interface inclination, the middle fracture shows more penetration into the caprocks, while the two sides fractures show slight penetration.

To study the effect of fracturing fluid injection rate on the vertical fracture penetration at inclination of 0°, the simulation results are shown in Figure 5.18. The results show that by increasing the injection rate the penetration becomes more apparent, especially when the injection rate exceeds 0.1m^3/s. This is because under the condition of a particular leakage coefficient, the high injection rate of the fluid can effectively avoid fracture closure by timely fluid refill. The results show that a higher fracturing fluid injection rate is favorable for fracture vertical penetration.

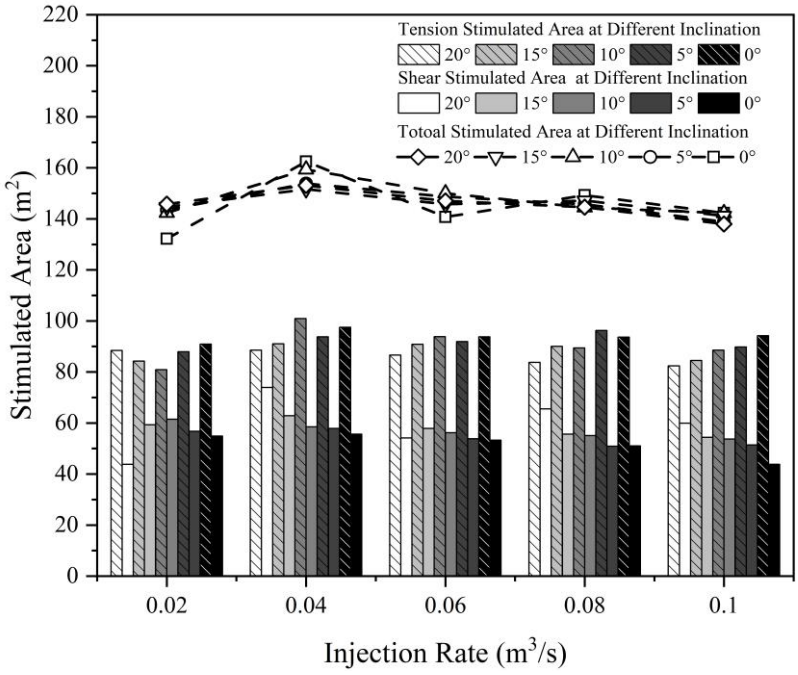

Figure 5.16 Total stimulated area: relationship of tension and shear Stimulated area and injection rate at different inclinations.

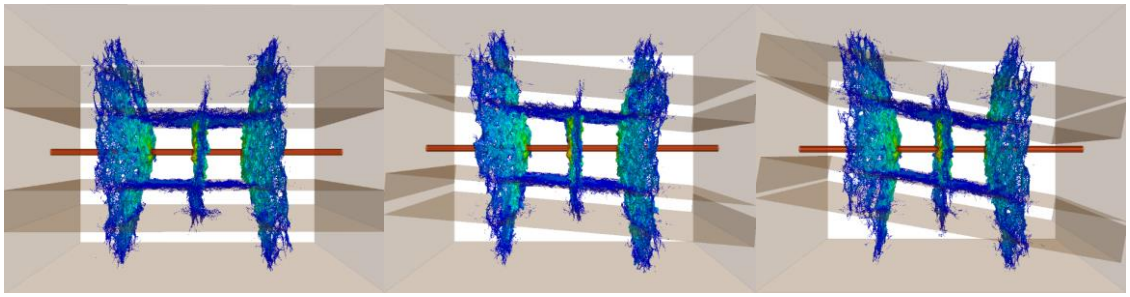

(a) **(b)** **(c)**

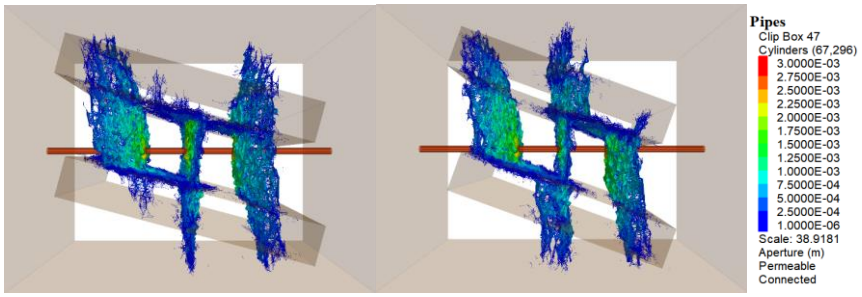

(d) **(e)**

Figure 5.17 Fracture extension patterns at injection rate of 0.06m^3/s and interface inclinations of (a) 0°, (b) 5°, (c) 10°, (d) 15° and (e) 20°.

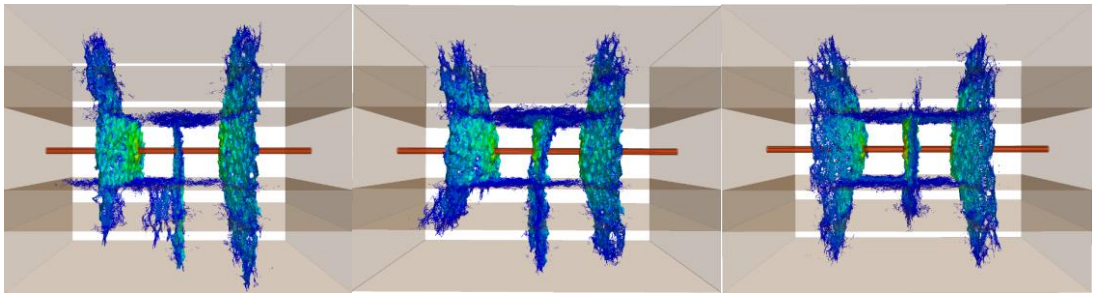

(a) **(b)** **(c)**

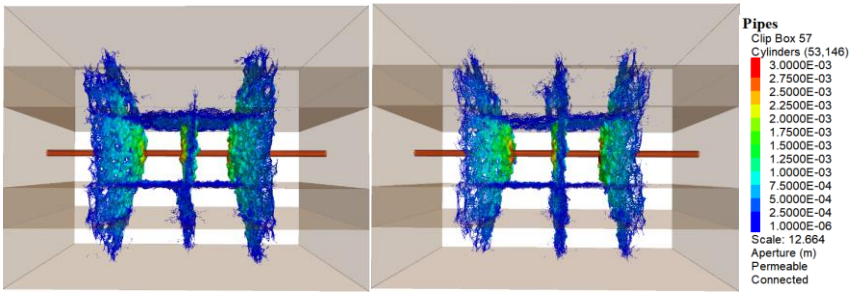

(d) **(e)**

Figure 5.18 Fracture extension pattern for interface inclination of 0° at different fracturing fluid injection rates of (a) 0.02 m^3/s, (b) 0.04 m^3/s, (c) 0.06 m^3/s, (d) 0.08 m^3/s and I 0.10 m^3/s.

5.3.6 Fluid Viscosity

The fluid viscosity was gradually increased to investigate its impact on fracture vertical penetration. The viscosity of the fracturing fluid was set to 0.001 Pa.s, 0.005 Pa.s, and 0.01 Pa.s. Figures 5.19 and 20 show the results.

The total stimulated area slightly increases as the fluid viscosity increases, as shown in Figure 5.19. The fluid viscosity effect on fracturing can be explained as the higher viscous fluid diminishes the

lateral fluid leak-off subsequently elevates the fracture volume during the fracturing treatment (B. Zhang et al., 2016). Results present models with high viscosity fluid favor to the fracture tension stimulated area, however, the low viscous fluid is more favorable in interface reactivation result in more interfacial slippage.

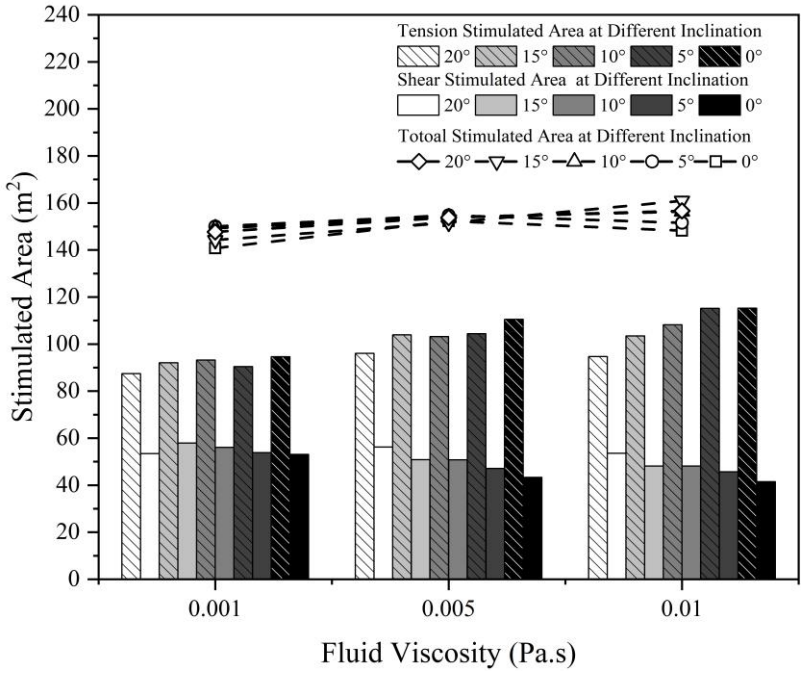

Figure 5.19 Relationship between total Stimulated area and interface inclination at different fluid viscosities.

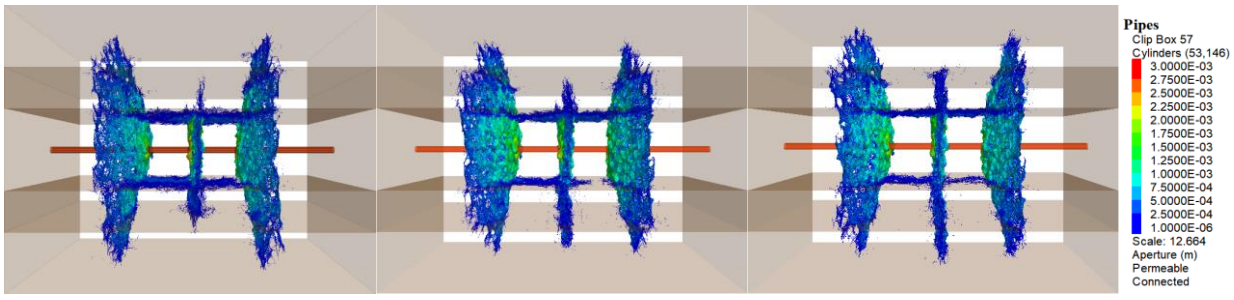

(a) **(b)** **(c)**

Figure 5.20 Fracture pattern at 0° interface inclination and different fluid viscosities of (a) 0.001Pa.s (b) 0.005Pa.s (c) 0.01Pa.s.

As seen from Figure 5.20, in contrast to low viscosity fluids, which can form a short middle fracture planes, the middle fracture propagation longer in vertical direction as the fluid viscosity increases. This because when the high viscosity fluid used, fracture breakdown pressure as well as propagation pressure higher than that with low viscous fluid, resulting in the middle fracture less affected by the stress shadow of two sides fractures.

5.4 Tension versus Shear Fractures

In the previous section, the SA was used as an indicator to characterize the contact area of the HF with reservoirs. This SA consists of tension and shear SAs, which indicates the different types of fractures, i.e., opened and sheared fractures. Here, we propose two terms of penetrate-ability and connectivity, to describe the degree of HF penetrating into the caprocks and connecting the natural interfaces. Therefore, the tension stimulated area can be an indicator to quantify the penetrate-ability of HF, whereas the shear SA is an indicator to quantify the connectivity with natural interfaces.

In order to see impacts of parameters considered in section 5.3 on the HF penetrate-ability and connectivity in laminated reservoir. Six individual parameters are transferred into a dimensionless space to assess their influence. The effective tensile strength was defined as the ratio of the tensile strength of the natural interface and caprock layer (which was assumed the same and synchronize change in this study) to the tensile strength of the reservoir formation; the ratio of the Young's modulus in caprock layer to the reservoir was denoted as effective Young's modulus; the effective injection rate was defined as the ratio of the injection rate to the minimum values used in each case; and the effective stress anisotropy was defined as the difference between maximum and minimum principal stress. Also, the dimensionless stimulated area was defined as all variables corresponding

stimulated area to the minimum variable corresponding stimulated area, i.e., the dimensionless tension stimulated area of the 3 effective differential stress was calculated by the ratio of the corresponding tension stimulated area 77.56 m^2 to the minimum effective differential stress (0 effective differential stress) corresponding stimulated area 64.56 m^2 to get the 1.2 dimensionless stimulated area. All of these dimensionless stimulated areas were calculated to see if they present a meaningful trend for quantitative analysis of the HF propagation and its geometry.

Simulation results of the SA in section 5.3 correspond to change of interface inclination from 20° to 0°. In order to eliminate the effect of the inclination, stimulated areas of 5 different inclinations were averaged to obtain a unique value, thus only the variables influence can be analyzed. Figure 5.21 shows the tension and shear SAs as a function of the six influencing factors. From this Figure the positive and negative influencing results are summarized in Table 5.2.

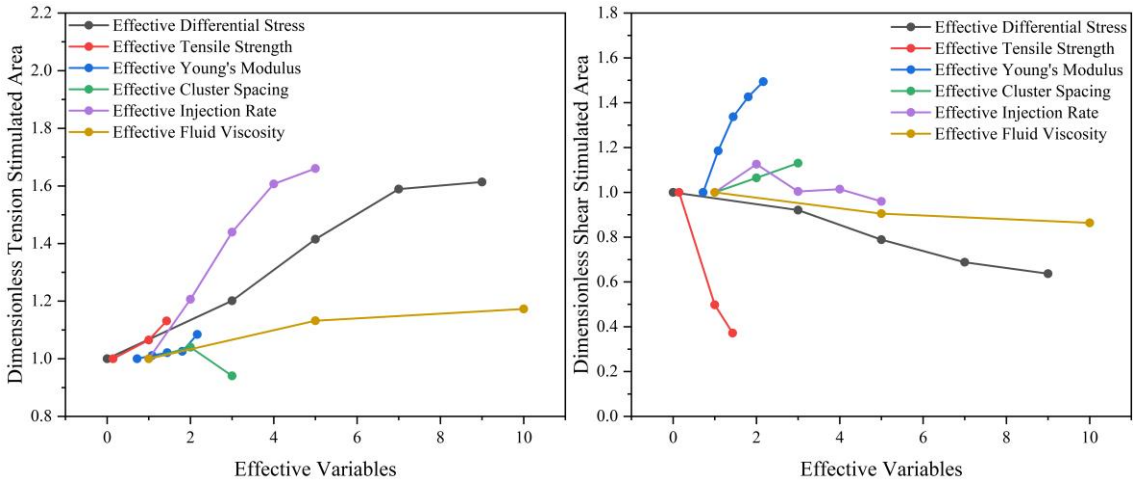

Figure 5.21 The effect of all influencing factors on dimensionless (a) tension stimulated area (b) shear stimulated area.

Table 5.2 Qualitative measure of contribution of each influencing factor on penetrate-ability and connectivity of natural interfaces by HF.

Effects	Type	Parameters					
		Young's Modulus	Differential Stress	Tensile strength	Cluster Spacing	Injection Rate	Fluid Viscosity
Penetrate-ability (Vertical)	Positive	✓	✓	✓	✓	✓	✓
	Negative						
Connectivity (Horizontal)	Positive	✓			✓		
	Negative		✓	✓		✓	✓

5.5 Analytic Hierarchy Process (AHP)

The Analytic Hierarchy Process (AHP) was initiallyveloped by Saaty in 1970 and is currently being applied to choice and ranking problems. A well-known advantage of AHP is the relative weighting of multiple factors for a complex evaluation. In this study, we use this quantitative evaluation method for the measurement of the Stimulation Potential Index (SPI).

In general, fours steps should come into consideration for AHP application (Larrodé et al., 2012):

1. Developing a hierarchy for the decisional problems

Choosing the most influential factors to help to solve the problem by isolating them into three levels of hierarchy: the goal, the criteria, and the attributes.

2. Evaluating a pairwise matrix (differ from traditional analysis according to experiences)

Considering a matrix according to the subjective experience and judgment of experts is prone to many errors. Here, we determine the matrix based on their data analysis results from the numerical simulation which is a more scientific approach. As shown in Table 5.3, the number a_{ij} indicates the contribution of factor *i* to the *j*.

3. Deriving the weight of each factor

The weight coefficient of each factor could be calculated from the Asymptotic Normalization Coefficient (ANC). The weight w_i can be formulated as:

$$W_i = \frac{\sum_{j=1}^{n} \frac{a_{ij}}{\sum_{k=1}^{n} a_{kj}}}{n} \ (i = 1,2, \dots, n) \tag{5.1}$$

where a_{ij} scales the significance of factors in the matrix.

4. Evaluating and ranking each parameter

This step is used to identify the most appropriate solution to the problem and rank them.

$$SPI = \sum_{x}^{j} w_j^i \, x_j^i \ (i = 1,2, \dots, n) \tag{5.2}$$

where $x_i{}^j$ is the influencing value of i_{th} value, and *SPI* is the result of the i_{th} factor on the objective, which means the stimulation potential index.

Table 5.3 Numerical scales of factor contribution according to experience and judgment (Sui et al., 2016).

Numerical scale a_{ij}	**Meaning and explanation**
1	Factors *i* and *j* contribute equally to the objective
2	Factor *i* is favored slightly over factor *j*
3	Factor *i* is favor fairly over factor *j*
4	Factor *i* is favor strongly over factor *j*
5	Factor *i* is favor very strongly over factor *j*
6	Factor *i* is favor extremely important over factor *j*
Reciprocals (i.e., 1, 1/3, 1/5, …1/9)	The reciprocal number reflects the reverse comparison positions of above

In order to take six factors into consideration in varying dimensions, values, and effective range, one assigns the following average weights to them to accomplish a potential production evaluation

with the AHP method. We can determine the positive and negative effects of factors using Table 5.2.

$$x_i = \begin{cases} \dfrac{(X - X_{min})}{(X_{max} - X_{min})} \text{ for positive factors} \\ \dfrac{(X_{max} - X)}{(X_{max} - X_{min})} \text{ for negative factors} \end{cases} \quad (5.3)$$

Here, x_j means the normalized factor, and X_{max} and X_{min} are maximum and minimum values of influencing factors. Therefore, the normalized factors x_j (j=1, 2, 3, …, 6) embodies Young's modulus, horizontal differential stress, tensile strength, cluster spacing, injection rate, fluid viscosity of laminated reservoir, respectively. A matrix of influencing factor's scales, corresponding to penetrate-ability and connectivity shown in Tables 5.4 and 5.5, are then constructed to determine the weight of each factor based on Equation. (5.1).

5.5.1 Evaluation of Stimulation Potential

An AHP process was used first to compare and then summarize the significance of the six factors for stimulation potential. i.e., the significance of one factor is calculated concerning another. Two matrixes of influencing parameters of penetrate-ability and connectivity are shown in Tables 5.4 and 5.5, respectively. Considering parametric evaluation of the SPI concludes that the penetrate-ability of HF in a laminated reservoir is more controlled by the injection rate and differential stress than fluid viscosity and tensile strength. Cluster spacing and Young's modulus are the next important influencing parameters. For the connectivity along the natural interface, tensile strength shows to be the most significant factor, followed by Young's modulus, differential stress, and fluid viscosity. The cluster spacing and injection rate are the two least important factors.

Table 5.4 The scale matrix of the six influencing factors on penetrate-ability.

A_{ij}	**Young's modulus**	**Differential stress**	**Tensile strength**	**Cluster spacing**	**Injection rate**	**Fluid viscosity**
Young's modulus	1	1/5	1/3	1/2	1/6	1/4
Differential stress	5	1	3	4	1/2	2
Tensile strength	3	1/3	1	2	1/4	1/2
Cluster spacing	2	1/4	1/2	1	1/5	1/3
Injection rate	6	2	4	5	1	3
Fluid viscosity	4	1/2	2	3	1/3	1

Table 5.5 The scale matrix of the six influencing factors on connectivity.

A_{ij}	**Young's modulus**	**Differential stress**	**Tensile strength**	**Cluster spacing**	**Injection rate**	**Fluid viscosity**
Young's modulus	1	2	1/2	5	3	4
Differential stress	1/2	1	1/3	4	2	3
Tensile strength	2	3	1	6	4	5
Cluster spacing	1/5	1/4	1/6	1	1/3	1/2
Injection rate	1/4	1/3	1/5	2	1/2	4
Fluid viscosity	1/3	1/2	1/4	3	1	2

Based on the scale matrix, applying the Equation (5.3) yields the weight of each influencing parameters in penetrate-ability:

$$w_j^p = \left(w_1^p, w_2^p, w_3^p, w_4^p, w_5^p, w_6^p\right) = (0.04, 0.25, 0.1, 0.07, 0.38, 0.16) \quad (5.4)$$

whereas the weight of each influencing parameters in connectivity is:

$$w_j^c = (w_1^c, w_2^c, w_3^c, w_4^c, w_5^c, w_6^c) = (0.25, 0.16, 0.38, 0.04, 0.07, 0.1) \quad (5.5)$$

Consequently, the weight of ultimate SPI calculated as the arithmetic mean of each influencing factor with respect to penetrate-ability and connectivity:

$$w_j = \frac{\left(w_j^p + w_j^c\right)}{2} = (w_1, w_2, w_3, w_4, w_5, w_6) = (0.15, 0.21, 0.24, 0.05, 0.22, 0.13) \quad (5.6)$$

Here, the weight values of w_1 to w_6 represent Young's modulus, differential stress, tensile strength, cluster spacing, injection rate, and fluid viscosity, respectively.

Accordingly, the SPI corresponding to each influencing factor can be calculated as

$$SPI = 0.15x_1^i + 0.2x_2^i + 0.24x_3^i + 0.06x_4^i + 0.22x_5^i + 0.13x_6^i \quad (5.7)$$

Substituting the value of x_j^i of each factor, the SPI of HF at a various formation properties and operational parameters in a laminated reservoir is obtained. Therefore, the maximum potential of HF stimulated area in laminated reservoir calculated based on Equation (5.7).

5.5.2 Case Study

In this section, the proposed methodology will be used to analyze the SPI during HF treatment in a laminated reservoir. A set of parameters created with the Monte Carlo method within the possible range are used for validation purposes, as shown in Table 5.6. Here, the fluid viscosity is the commonly used slick water in HF operations. Following the steps presented in previous section, Table 5.7 lists the normalized influencing factors of various generated laminated reservoirs' properties.

Substituting the value x_j^i of each influencing factor from Table 5.7, the coefficients of SPI of laminated reservoirs at various formation properties are shown in Figure 5.22. In this Figure, lines

represent the total SA obtained from simulations as well as columns are corresponding SPIs calculated based on Equation (5.7). Results demonstrate SPIs increase with the increase of SA in general, the presented similar trend is able to validate the prediction potential of the proposed quantification method. Therefore, a quantification method that considers the contribution of multiple influencing factors to laminated reservoir stimulation potential is necessary.

Table 5.6 Generated parameters required for SPI analysis.

	Young's modulus (GPa)	Differential stress (MPa)	Tensile strength (MPa)	Cluster spacing (m)	Injection rate (m3/s)	Fluid viscosity (Pa.s)
Case 1	30.45	4.45	0.39	1.45	0.08	0.001
Case 2	49.6	2.1	0.53	1.5	0.07	0.001
Case 3	43	5.7	2.5	1.5	0.08	0.001
Case 4	46.2	8.97	3.13	1.319	0.02	0.001
Case 5	55.92	8.49	3.91	1.41	0.07	0.001

Table 5.7 Normalized influencing parameters of laminated formation.

	Young's modulus (GPa)	Differential stress (MPa)	Tensile strength (MPa)	Cluster spacing (m)	Injection rate (m^3/s)	Fluid viscosity (Pa.s)
Case 1	0.26	0.49	0.08	0.22	0.75	0
Case 2	0.74	0.23	0.11	0.25	0.59	0
Case 3	0.58	0.63	0.50	0.25	0.73	0
Case 4	0.66	0.56	0.63	0.16	0.03	0
Case 5	0.90	0.94	0.78	0.21	0.62	0

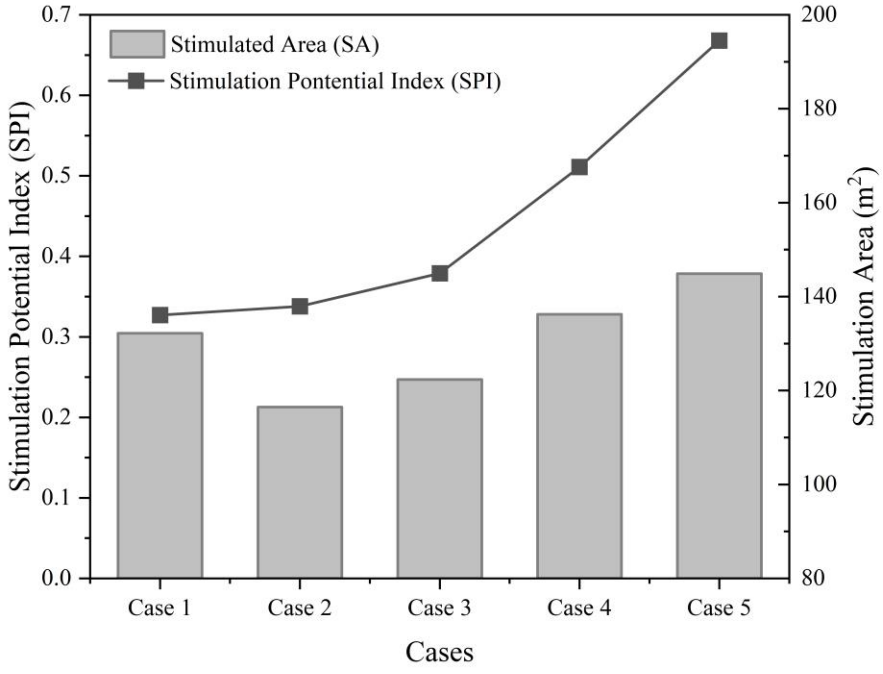

Figure 5.22 The coefficient of SPI varying with reservoir properties.

5.6 Summary

In this chapter, lattice-based numerical simulations were conducted to study the influence of the caprock and interface characteristics on the HF propagation pattern in shale reservoirs consideration multi-clusters HFs. Followings are the main conclusions from this study.

(1) The ultimate morphology of the fracture is influenced by the interface characteristics as well as the caprock and reservoir properties. Formation properties and operational parameters are the two major determinants of fracture morphology in general. Horizontal differential stress, cluster spacing, barrier and interface tensile strength, fracturing fluid injection rate, and viscosity are the major influencing factors.

(2) The larger horizontal differential stress is favorable for a HF to cross the caprocks during multi-cluster fracturing in laminated reservoirs, however, it is not favorable for its propagation and communication along the horizontal interfaces. When the differential stress is 7 MPa and the

interface inclination is 80°, the fracture network is well developed, and the SA is maximized. The simulation results showed that excessive differential stress reduces the complexity of fracture systems. Cluster spacing and differential stress were found to have similar effects, causing the middle fracture length to increase as cluster spacing and horizontal differential stress increase. By increasing cluster spacing, the stress shadow is reduced, and the fracture deflection on both sides is reduced. As a result, an appropriate cluster spacing allows stress shadows to cause HFs to communicate with each other, forming a connected network and maintaining good layer penetration.

(3) When the inclination is kept constant, the vertical length of the middle HF increases as the caprocks and interface tensile strength decreases, whereas the connectivity at the interface increases as the caprocks and interface tensile strength increases. When the inclination is 80° and the tensile strength is 5MPa, i.e., the tensile strength of the caprock is greater than the reservoir formation, the most complexity of the fracture network and the maximum area of fracture SA are achieved.

(4) The effect of interface inclination on the SA is negligible, according to an analysis of the effect of fluid injection rate on the SA. The penetrate-ability of the middle fracture improves significantly as the fracturing fluid injection rate increases. When the injection rate reaches $0.1m^3/s$, the middle fracture completely penetrates the caprocks, and its fracture height exceeds that of the fractures on the left and right sides. Vertical fracture extension is aided by a higher inclination angle and a higher fracture fluid injection rate, and the fracture SA peaks when the fluid injection rate reaches $0.1m^3/s$ at an inclination of 85°. However, fracturing complexity will be hampered if the fluid injection rate is too high.

(5) A lower viscous fracturing fluid favor the fracture propagate along the natural interfaces whereas high viscous fluid easier for fracture penetrate interfaces. When the high viscosity fracturing fluid injection, middle fracture propagates longer than the case with low viscosity.

(6) A new methodology proposed for the quantitative evaluation of the stimulation potential of laminated reservoir based on the analysis of contribution of the six influencing factors. A series of artificially generated formation with different rock properties for establishing the evaluation model of stimulation and verifying the accuracy of the proposed method.

In the next chapter, conclusions and recommendations of this dissertation will be summarized.

Chapter 6

Conclusions and Recommendations

6.1 Conclusions

The main conclusions from this study are summarized below.

- A conception of IPRI was proposed to characterize the slope of the log-log plot of pressure time curve during the fracture propagation stage.
- Sensitivity analysis of angle of approach, interfacial friction, injection fluid viscosity, and differential stress were done to study their influence on IPRI.
- Based on 140 simulation cases with varying input parameters, a predictive model was created. The model's results demonstrated a strong ability to predict the interaction modes corresponding to some lab experimental data.
- Caprock that is higher Young's modulus facilitates HF vertical and horizontal extension. Increased vertical stress anisotropy prevents HF horizontal extension. HF horizontal propagation is prevented by the higher tensile strength of the interface and caprock. A higher injection rate encourages the reservoir's HF width to increase.
- The tension stimulated area (TSA) and shear stimulated area (SSA) was used to determine the vertical and horizontal extendibility of HF. The TSA shows HF's ability to penetrate

the interface and propagate vertically, whereas the SSA represents the ability of HF to form interface slippage or horizontal propagation of the fracture. These two parameters can quantitatively describe the behavior of HF propagation when it interacts with natural interfaces.

- The stimulated area ratio (SAR), which is the ratio of TSA to SSA, was used as a parameter to show how HF propagation transitions between vertical and horizontal directions. The SAR is proportional to HF penetrability. A dimensionless space was used to show how mechanical and operational factors influence the propagation of HFs along different pathways in a laminated formation.

- An ultimate morphology of the fracture is influenced by the caprock, reservoir, and interface characteristics. Determinants of fracture morphology are formation properties and operational parameters. In specific, horizontal differential stress, cluster spacing, barrier and interface tensile strength, fracturing fluid injection rate, and viscosity are the major influencing factors.

- Increasing the horizontal differential stress is favorable for multi-cluster fracturing in laminated reservoirs, but it is not favorable for horizontal interface propagation and communication. Excessive differential stress was found to reduce the complexity of fracture systems. The middle fracture length increases as both cluster spacing and horizontal differential stress increase. Cluster spacing increases, stress shadow is reduced, and fracture deflection on both sides is reduced. Due to this, stress shadows cause HFs to communicate, resulting in a connected network and maintaining good layer penetration.

- The middle HF length increases as the caprocks and interfaces tensile strength increase, while the interface connectivity increases when the caprocks and interface tensile strength decrease.

- According to the fluid injection rate analysis, the effect of interface inclination on the SA is negligible. Injection rate has a dramatic effect on middle fracture penetrate-ability. Increasing the fracture fluid injection rate and the inclination angle together make the fracture extend farther vertically. However, excessively high fluid injection rates would inhibit the fracture complexity.

- The fracture propagates along the natural interfaces with a lower viscous fracturing fluid, whereas the high viscous fluid easily penetrates interfaces for fractures. When high viscosity fluid injected, the middle fracture propagates longer than a low viscosity fracture.

- The six influencing factors of a laminated reservoir were considered in a new approach to quantitative evaluation of the stimulation potential. A series of artificially generated formations, each with different rock properties, used to develop and verify the method of stimulation.

6.2 Recommendations and Future Works

- The predictive model proposed in Chapter 3 still needs field scale fracturing treatment to prove the feasibility.
- In Chapter 4, the stimulated area used to characterize the hydraulic fracture propagation pattern, vertical penetration versus horizontal shear slip, cannot represent the real stimulated area after shut in the pumping. Proppants will be mixed with fracturing fluid to investigate the propped area in the reservoir in future work.
- The stress shadow effect in multi-cluster hydraulic fracture was not clarified in Chapter 5, especially its influence on hydraulic fracture interaction with natural interfaces in the laminated reservoir.
- The stimulation potential evaluation model in Chapter 6 only verified with a small range of artificially generated data, which should be extended to real field data to prove the accuracy.

Reference

Adachi, J., Siebrits, E., Peirce, A., & Desroches, J. (2007). Computer simulation of hydraulic fractures. *International Journal of Rock Mechanics and Mining Sciences*, *44*(5), 739–757. https://doi.org/10.1016/j.ijrmms.2006.11.006

Afsar, F. (2014). *Fracture propagation and reservoir permeability in limestone-marl alternations of the Jurassic Blue Lias Formation (Bristol Channel Basin , UK)*.

Alcoser, L., Ovalle, A., & Parsons, M. (2012). The Bakken: Utilizing a Petroleum System Based Analysis to Optimally Exploit One of the World's Largest Oil Deposits. *All Days*, 14–42. https://doi.org/10.2118/158918-MS

Bakhshi, E., Rasouli, V., Ghorbani, A., Fatehi Marji, M., Damjanac, B., & Wan, X. (2019). Lattice Numerical Simulations of Lab-Scale Hydraulic Fracture and Natural Interface Interaction. *Rock Mechanics and Rock Engineering*, *52*(5), 1315–1337. https://doi.org/10.1007/s00603-018-1671-2

Beale, M. H., Hagan, M. T., & Demuth, H. B. (2020). *Deep Learning Toolbox ™ User ' s Guide*.

Beugelsdijk, L. J. L., De Pater, C. J., & Sato, K. (2000). Experimental hydraulic fracture propagation in a multi-fractured medium. *Proceedings of the SPE Asia Pacific Conference on Integrated Modelling for Asset Management*, 177–184. https://doi.org/10.2523/59419-ms

Blanton, T. (1986). Propagation of hydraulically and dynamically induced fractures in naturally fractured reservoirs. *SPE Unconventional Gas Technology Symposium*, 613–621. https://doi.org/10.2523/15261-MS

Bourne, S. J., Brauckmann, F., Rijkels, L., Stephenson, B. J., Weber, A., & Willemse, E. J. M. (2000). Predictive modelling of naturally fractured reservoirs using geomechanics and flow simulation. *Society of Petroleum Engineers - Abu Dhabi International Petroleum Exhibition and Conference 2000, ADIPEC 2000*, *6*(1). https://doi.org/10.2118/87253-ms

Calvez, J. L., Malpani, R., Xu, J., Stokes, J., Williams, M., Le Calvez, J., Malpani, R., Xu, J., Stokes, J., Williams, M., Probert, T., Bradford, I., Cambridge, E., & Zakhour, N. (2016). Hydraulic Fracturing Insights from Microseismic Monitoring. *Oilfield Review*, *28*(2), 16–33.

Carrier, B., & Granet, S. (2012). Numerical modeling of hydraulic fracture problem in permeable medium using cohesive zone model. *Engineering Fracture Mechanics*, *79*, 312–328. https://doi.org/10.1016/j.engfracmech.2011.11.012

Cheng, Y., & Zhang, Y. (2020). Experimental Study of Fracture Propagation: The Application in Energy Mining. *Energies*, *13*(6), 1411. https://doi.org/10.3390/en13061411

Chuprakov, D. A., Akulich, A., Siebrits, E., & Thiercelin, M. J. (2010). *Hydraulic Fracture Propagation in a Naturally Fractured Reservoir*. 1–12. https://doi.org/10.2118/128715-ms

Chuprakov, D., Melchaeva, O., & Prioul, R. (2014). Injection-sensitive mechanics of hydraulic fracture interaction with discontinuities. *47th US Rock Mechanics / Geomechanics Symposium*, *47*(5), 1625–1640. https://doi.org/10.1007/s00603-014-0596-7

Damjanac, B., & Cundall, P. (2016). Application of distinct element methods to simulation of hydraulic fracturing in naturally fractured reservoirs. *Computers and Geotechnics*, *71*, 283–294. https://doi.org/10.1016/j.compgeo.2015.06.007

Damjanac, B., Detournay, C., & Cundall, P. A. (2016). Application of particle and lattice codes to simulation of hydraulic fracturing. *Computational Particle Mechanics*, *3*(2), 249–261. https://doi.org/10.1007/s40571-015-0085-0

Damjanac, B., Detournay, C., Cundall, P. A., & Varun. (2013). Three-dimensional numerical model of hydraulic fracturing in fractured rock masses. *ISRM International Conference for Effective and Sustainable Hydraulic Fracturing 2013*, 819–830. https://doi.org/10.5772/56313

Daneshy, A. (2019, January 29). Three-dimensional analysis of interactions between hydraulic and natural fractures. *Society of Petroleum Engineers - SPE Hydraulic Fracturing Technology Conference and Exhibition 2019, HFTC 2019*. https://doi.org/10.2118/194335-ms

Daneshy, A. A. (2007). Hydraulic Fracture Propagation in Layered Formations. *Society of Petroleum Engineers Journal*, *18*(01), 33–41. https://doi.org/10.2118/6088-pa

Dohmen, T., Blangy, J. P., & Zhang, J. (2014). Microseismic depletion delineation. *Interpretation*, *2*(3), SG1–SG13. https://doi.org/10.1190/INT-2013-0164.1

Dou, F., Wang, J. G., Leung, C. F., & Ma, Z. (2021). The alterations of critical pore water pressure and micro-cracking morphology with near-wellbore fractures in hydraulic fracturing of shale reservoirs. *Engineering Fracture Mechanics*, *242*(November 2020), 107481. https://doi.org/10.1016/j.engfracmech.2020.107481

Dou, F., Wang, J. G., Wang, H., Hu, B., & Li, C. (2019). Discrete Element Analysis for Hydraulic Fracture Propagations in Laminated Reservoirs with Complex Initial Joint Properties. *Geofluids*, *2019*, 1–23. https://doi.org/10.1155/2019/3958583

Eberhardt, E., Stead, D., & Coggan, J. S. (2004). Numerical analysis of initiation and progressive failure in natural rock slopes-the 1991 Randa rockslide. *International Journal of Rock Mechanics and Mining Sciences*, *41*(1), 69–87. https://doi.org/10.1016/S1365-1609(03)00076-5

Economides, M. J., & Nolte, K. . (2000). Reservoir Stimulation. In *Enhanced Oil Recovery Field Case Studies* (Vol. 53, Issue Third Edition). https://doi.org/10.1017/CBO9781107415324.004

Fallahzadeh, S., Hossain, M., James Cornwell, A., & Rasouli, V. (2017). Near Wellbore Hydraulic Fracture Propagation from Perforations in Tight Rocks: The Roles of Fracturing Fluid Viscosity and Injection Rate. *Energies*, *10*(3), 359. https://doi.org/10.3390/en10030359

Fatahi, H., Hossain, M. M., & Sarmadivaleh, M. (2017). Numerical and experimental investigation of the interaction of natural and propagated hydraulic fracture. *Journal of Natural Gas Science and Engineering*, *37*, 409–424. https://doi.org/10.1016/j.jngse.2016.11.054

Feng, Y., Jones, J. F., & Gray, K. E. (2015). Pump-in and Flow-back Tests for Determination of Fracture Parameters and In-situ Stresses. *AADE National Technical Conference and Exhibition, April 2015*, 11.

Feng, Y., Jones, J. F., & Gray, K. E. (2016). A Review on Fracture-Initiation and -Propagation Pressures for Lost Circulation and Wellbore Strengthening. *SPE Drilling & Completion*, *31*(02), 134–144. https://doi.org/10.2118/181747-pa

Fisher, M. K., Heinze, J. R., Harris, C. D., Davidson, B. M., Wright, C. A., & Dunn, K. P.

(2004). Optimizing Horizontal Completion Techniques in the Barnett Shale Using Microseismic Fracture Mapping. *SPE Annual Technical Conference and Exhibition*. https://doi.org/10.2118/90051-MS

Fu, W., Ames, B. C., Bunger, A. P., & Savitski, A. A. (2016). Impact of Partially Cemented and Non-persistent Natural Fractures on Hydraulic Fracture Propagation. *Rock Mechanics and Rock Engineering*, *49*(11), 4519–4526. https://doi.org/10.1007/s00603-016-1103-0

Fu, W., Savitski, A. A., & Bunger, A. P. (2018). Analytical criterion predicting the impact of natural fracture strength, height and cemented portion on hydraulic fracture growth. *Engineering Fracture Mechanics*, *204*(September), 497–516. https://doi.org/10.1016/j.engfracmech.2018.10.002

Fu, W., Savitski, A. A., Damjanac, B., & Bunger, A. P. (2019). Three-dimensional lattice simulation of hydraulic fracture interaction with natural fractures. *Computers and Geotechnics*, *107*(April 2018), 214–234. https://doi.org/10.1016/j.compgeo.2018.11.023

Geertsma, J., & Klerk, F. d. (1969). Rapid Method of Predicting Width and Extent of Hydraulically Induced Fractures. *J Petroleum Technology*, *21*(12), 1571–1581. https://doi.org/10.2118/2458-pa

Goldstein, R. V., & Osipenko, N. M. (2015). Initiation of a secondary crack across a frictional interface. *Engineering Fracture Mechanics*, *140*, 92–105. https://doi.org/10.1016/j.engfracmech.2015.03.036

Gu, H., & Weng, X. (2010). Criterion for Fractures Crossing Frictional Interfaces at Non-orthogonal Angles. *44th US Rock Mechanics Symposium and 5th U.S.-Canada Rock Mechanics Symposium*, 1–6.

Gu, Hongren, & Siebrits, E. (2005). Effect of formation modulus contrast on hydraulic fracture height containment. *SPE Production and Operations*, *23*(2), 170–176. https://doi.org/10.2118/103822-pa

Hossain, M. M., & Rahman, M. K. (2008). Numerical simulation of complex fracture growth during tight reservoir stimulation by hydraulic fracturing. *Journal of Petroleum Science and Engineering*, *60*(2), 86–104. https://doi.org/10.1016/j.petrol.2007.05.007

Hunsweek, M. J., Shen, Y., & Lew, A. J. (2006). A finite element approach to the simulation of hydraulic fractures with lag. *International Journal for Numerical and Analytical Methods in Geomechanics*, *30*(13), 1303–1336. https://doi.org/10.1002/nag

Isah, A., Hiba, M., Al-Azani, K., Aljawad, M. S., & Mahmoud, M. (2021). A comprehensive review of proppant transport in fractured reservoirs: Experimental, numerical, and field aspects. *Journal of Natural Gas Science and Engineering*, *88*(October 2020), 103832. https://doi.org/10.1016/j.jngse.2021.103832

Ivars, D. M., Pierce, M. E., Darcel, C., Reyes-Montes, J., Potyondy, D. O., Young, R. P., & Cundall, P. A. (2011). The synthetic rock mass approach for jointed rock mass modelling. *International Journal of Rock Mechanics and Mining Sciences*, *48*(2), 219–244. https://doi.org/10.1016/j.ijrmms.2010.11.014

Kang, H., Lou, J., Gao, F., Yang, J., & Li, J. (2018). A physical and numerical investigation of sudden massive roof collapse during longwall coal retreat mining. *International Journal of Coal Geology*, *188*(January), 25–36. https://doi.org/10.1016/j.coal.2018.01.013

Khristianovic, S. A., & Zheltov, Y. P. (1955). Formation of vertical fractures by means of highly viscous liquid. *World Petroleum Congress Proceedings*, *1955-June*, 579–586.

Larrodé, E., Moreno-Jiménez, J. M., & Muerza, M. V. (2012). An AHP-multicriteria suitability evaluation of technological diversification in the automotive industry. *International Journal of Production Research*, *50*(17), 4889–4907. https://doi.org/10.1080/00207543.2012.657975

Lecampion, B., & Desroches, J. (2015). Simultaneous initiation and growth of multiple radial hydraulic fractures from a horizontal wellbore. *Journal of the Mechanics and Physics of Solids*, *82*, 235–258. https://doi.org/10.1016/j.jmps.2015.05.010

Leem, J., Day, R., Latimer, C., Lakani, R., & Reyna, J. (2014). Geomechanics in Optimal Multi-Stage Hydraulic Fracturing Design for Resource Shale and Tight Reservoirs. *EAGE Workshop on Geomechanics in the Oil and Gas Industry*, *December*, 115–119. https://doi.org/10.3997/2214-4609.20140468

Lei, Q., Latham, J. P., & Tsang, C. F. (2017). The use of discrete fracture networks for modelling coupled geomechanical and hydrological behaviour of fractured rocks. *Computers and Geotechnics*. https://doi.org/10.1016/j.compgeo.2016.12.024

Li, H., Zou, Y., Liu, S., & Valko, P. P. (2017). Numerical investigation of multi-well, multi-stage hydraulic fracture height growth in laminated shale reservoirs using finite-discrete element method. *51st US Rock Mechanics / Geomechanics Symposium 2017*, *3*(October).

Ling, K., & Zeng, Z. (2013). *Geomechanical Study of Bakken Formation for Improved Oil Recovery*.

Liu, X., Qu, Z., Guo, T., Sun, Y., Wang, Z., & Bakhshi, E. (2019). Numerical simulation of non-planar fracture propagation in multi-cluster fracturing with natural fractures based on Lattice methods. *Engineering Fracture Mechanics*, *220*(March), 106625.

https://doi.org/10.1016/j.engfracmech.2019.106625

Liu, X., Rasouli, V., Guo, T., Qu, Z., & Sun, Y. (2020). Numerical simulation of stress shadow in multiple cluster hydraulic fracturing in horizontal wells based on lattice modelling. *Engineering Fracture Mechanics*, *238*(June), 107278. https://doi.org/10.1016/j.engfracmech.2020.107278

Liu, Y. J., Mukherjee, S., Nishimura, N., Schanz, M., Ye, W., Sutradhar, A., Pan, E., Dumont, N. A., Frangi, A., & Saez, A. (2012). Recent Advances and Emerging Applications of the Boundary Element Method. *Applied Mechanics Reviews*, *64*(3). https://doi.org/10.1115/1.4005491

Lu, C., Xiao, Y., Chun, J., & Li, G. (2020). Stability of the formation interface under the impact of hydraulic fracture propagation in the vicinity of the formation interface. *Petroleum Science*, *0123456789*. https://doi.org/10.1007/s12182-019-00416-x

Martins, R. (1989). *Recent advances in hydraulic physical modelling*. https://doi.org/10.1007/978-94-009-2344-7

Maxwell, S. C. (2011). *What does microseismicity tells us about hydraulic fractures? November*, 1565–1569. https://doi.org/10.1190/1.3627501

Mews, K. S., Alhubail, M. M., & Barati, R. G. (2019). A review of brittleness index correlations for unconventional tight and ultra-tight reservoirs. In *Geosciences (Switzerland)* (Vol. 9, Issue 7, p. 319). https://doi.org/10.3390/geosciences9070319

Mohammadnejad, T., & Khoei, A. R. (2013). An extended finite element method for hydraulic fracture propagation in deformable porous media with the cohesive crack model. *Finite*

Elements in Analysis and Design, *73*, 77–95. https://doi.org/10.1016/j.finel.2013.05.005

Morozov, A. D., Popkov, D. O., Duplyakov, V. M., Mutalova, R. F., Osiptsov, A. A., Vainshtein, A. L., Burnaev, E. V., Shel, E. V., & Paderin, G. V. (2020). Data-driven model for hydraulic fracturing design optimization: focus on building digital database and production forecast. *Journal of Petroleum Science and Engineering*, *194*. https://doi.org/10.1016/j.petrol.2020.107504

Nagel, N. B., Sanchez-Nagel, M. A., Zhang, F., Garcia, X., & Lee, B. (2013). Coupled numerical evaluations of the geomechanical interactions between a hydraulic fracture stimulation and a natural fracture system in shale formations. *Rock Mechanics and Rock Engineering*, *46*(3), 581–609. https://doi.org/10.1007/s00603-013-0391-x

Nejma. (2020). *SIMULATION OF NOTCH DRIVEN HYDRAULIC FRACTURE IN OPEN* (Issue August).

Nordgren, R. P. (1972). Propagation of a Vertical Hydraulic Fracture. *Society of Petroleum Engineers Journal*, *12*(04), 306–314. https://doi.org/10.2118/3009-pa

Perkins, T. K., & Kern, L. R. (1961). Widths of Hydraulic Fractures. *Journal of Petroleum Technology*, *13*(09), 937–949. https://doi.org/10.2118/89-pa

Potyondy, D. O., & Cundall, P. A. (2004). A bonded-particle model for rock. *International Journal of Rock Mechanics and Mining Sciences*, *41*(8 SPEC.ISS.), 1329–1364. https://doi.org/10.1016/j.ijrmms.2004.09.011

Qiu, D., Rasouli, V., Damjanac, B., & Wan, X. (2019). Narrow versus Wide Fairway Fracture Geometry. *53 Rd US ROCK MECHANICS / GEOMECHANICS SYMPOSIUM*.

Renshaw, C. E., & Pollard, D. D. (1995). An experimentally verified criterion for propagation across unbounded frictional interfaces in brittle, linear elastic materials. *International Journal of Rock Mechanics and Mining Sciences And*, *32*(3), 237–249. https://doi.org/10.1016/0148-9062(94)00037-4

Rich, J., & Ammerman, M. (2010). Unconventional Geophysics for Unconventional Plays. *SPE Unconventional Gas Conference*, 216–222. https://doi.org/10.2523/131779-MS

Rueda, J., Mejia, C., & Roehl, D. (2019). Hydro-mechanical modeling of hydraulic fracture propagation and its interactions with frictional natural fractures. *Computers and Geotechnics*, *111*(February), 290–300. https://doi.org/10.1016/j.compgeo.2019.03.020

Sarmadivaleh, M. (2012). Experimental and Numerical Study of Interaction of a Pre-Existing Natural Interface and an Induced Hydraulic Fracture. In *Curtin University*. https://doi.org/10.13140/RG.2.1.1286.2882

Sarmadivaleh, M., & Rasouli, V. (2014). Modified Reinshaw and Pollard Criteria for a Non-Orthogonal Cohesive Natural Interface Intersected by an Induced Fracture. *Rock Mechanics and Rock Engineering*, *47*(6), 2107–2115. https://doi.org/10.1007/s00603-013-0509-1

Sarmadivaleh, M., & Rasouli, V. (2015). Test Design and Sample Preparation Procedure for Experimental Investigation of Hydraulic Fracturing Interaction Modes. *Rock Mechanics and Rock Engineering*, *48*(1), 93–105. https://doi.org/10.1007/s00603-013-0543-z

Savitski, A. A., & Detournay, E. (2002). *Propagation of a penny-shaped fluid-driven fracture in an impermeable rock : asymptotic solutions*. *39*, 6311–6337.

Sayers, C. M., & Calvez, J. Le. (2010). Characterization of microseismic data in gas shales using

the radius of gyration tensor. *SEG Technical Program Expanded Abstracts 2010*, *2*, 2080–2084. https://doi.org/10.1190/1.3513255

Schmidt, D. D., Smith, S. A., Sorensen, J. A., & Steadman, E. N. (2011). *Evaluation of Key Factors Affecting Successful Oil Production in the Bakken Formation , North Dakota – Phase II* (Issue November).

Settgast, R. R., Fu, P., Walsh, S. D. C., White, J. A., Annavarapu, C., & Ryerson, F. J. (2017). A fully coupled method for massively parallel simulation of hydraulically driven fractures in 3-dimensions. *International Journal for Numerical and Analytical Methods in Geomechanics*, *41*(5), 627–653. https://doi.org/10.1002/nag.2557

Shi, F., Wang, X., Liu, C., Liu, H., & Wu, H. (2017). An XFEM-based method with reduction technique for modeling hydraulic fracture propagation in formations containing frictional natural fractures. *Engineering Fracture Mechanics*, *173*, 64–90. https://doi.org/10.1016/j.engfracmech.2017.01.025

Simonson, E. R., Abou-Sayed, A. S., & Clifton, R. J. (1978). Containment of Massive Hydraulic Fractures. *Society of Petroleum Engineers Journal*, *18*(1), 27–32. https://doi.org/10.2118/6089-pa

Smith, M. B., Bale, A. B., Britt, L. K., Klein, H. H., Siebrits, E., & Dang, X. (2001). Layered Modulus Effects on Fracture Propagation, Proppant Placement, and Fracture Modeling. *SPE Annual Technical Conference and Exhibition*, 2919–2932. https://doi.org/10.2118/71654-ms

Sui, L., Ju, Y., Yang, Y., Yang, Y., & Li, A. (2016). A quantification method for shale fracability based on analytic hierarchy process. *Energy*, *115*, 637–645.

https://doi.org/10.1016/j.energy.2016.09.035

Sun, W. J., Kothari, S., & Sun, C. C. (2018). The relationship among tensile strength, Young's modulus, and indentation hardness of pharmaceutical compacts. *Powder Technology*, *331*, 1–6. https://doi.org/10.1016/j.powtec.2018.02.051

Tan, P., Jin, Y., Han, K., Hou, B., Chen, M., Guo, X., & Gao, J. (2017). Analysis of hydraulic fracture initiation and vertical propagation behavior in laminated shale formation. *Fuel*, *206*, 482–493. https://doi.org/10.1016/j.fuel.2017.05.033

Tang, J., & Wu, K. (2018). A 3-D model for simulation of weak interface slippage for fracture height containment in shale reservoirs. *International Journal of Solids and Structures*, *144–145*, 248–264. https://doi.org/10.1016/j.ijsolstr.2018.05.007

Teufel, L. W., & Clark, J. A. (1984). Hydraulic Fracture Propagation in Layered Rock: Experimental Studies of Fracture Containment. *Society of Petroleum Engineers Journal*, *24*(1), 19–32. https://doi.org/10.2118/9878-PA

Wang, H. (2015). Numerical modeling of non-planar hydraulic fracture propagation in brittle and ductile rocks using XFEM with cohesive zone method. *Journal of Petroleum Science and Engineering*, *135*, 127–140. https://doi.org/10.1016/j.petrol.2015.08.010

Wang, H. (2016). Numerical investigation of fracture spacing and sequencing effects on multiple hydraulic fracture interference and coalescence in brittle and ductile reservoir rocks. *Engineering Fracture Mechanics*, *157*(February 2016), 107–124. https://doi.org/10.1016/j.engfracmech.2016.02.025

Wang, H. (2019). Hydraulic fracture propagation in naturally fractured reservoirs: Complex

fracture or fracture networks. *Journal of Natural Gas Science and Engineering*, *68*(June), 102911. https://doi.org/10.1016/j.jngse.2019.102911

Wangen, M. (2013). Finite element modeling of hydraulic fracturing in 3D. *Computational Geosciences*, *17*(4), 647–659. https://doi.org/10.1007/s10596-013-9346-2

Warpinski, N. R., & Teufel, L. W. (1987). Influence of Geologic Discontinuities on Hydraulic Fracture Propagation. *Journal of Petroleum Technology*, *39*(2), 689–696. https://doi.org/https://doi.org/10.1016/B978-081551554-8.50015-X

Warpinski, Norman R., Schmidt, R. A., & Northrop, D. A. (1982). In-Situ Stresses: the Predominant Influence on Hydraulic Fracture Containment. *Journal of Petroleum Technology*, *34*(3), 653–664. https://doi.org/10.2118/8932-PA

Waters, G., Dean, B., Downie, R., Kerrihard, K., Austbo, L., & McPherson, B. (2009). Simultaneous hydraulic fracturing of adjacent horizontal wells in the woodford shale. *Society of Petroleum Engineers - SPE Hydraulic Fracturing Technology Conference 2009*, 694–715. https://doi.org/10.2118/119635-ms

Wong, J. K. (2017). *Three-dimensional multi-scale hydraulic fracturing stimulation in heterogeneous material using Dual Lattice Model* (Issue May). https://doi.org/10.17863/CAM.17439

Yu, H., Dahi Taleghani, A., & Lian, Z. (2019). On how pumping hesitations may improve complexity of hydraulic fractures, a simulation study. *Fuel*, *249*(February), 294–308. https://doi.org/10.1016/j.fuel.2019.02.105

Yushi, Z., Xinfang, M., Shicheng, Z., Tong, Z., & Han, L. (2016). Numerical Investigation into

the Influence of Bedding Plane on Hydraulic Fracture Network Propagation in Shale Formations. *Rock Mechanics and Rock Engineering*, *49*(9), 3597–3614. https://doi.org/10.1007/s00603-016-1001-5

Zhang, B., Li, X., Zhang, Z., Wu, Y., Wu, Y., & Wang, Y. (2016). Numerical Investigation of Influence of In-Situ Stress Ratio, Injection Rate and Fluid Viscosity on Hydraulic Fracture Propagation Using a Distinct Element Approach. *Energies*, *9*(3), 140. https://doi.org/10.3390/en9030140

Zhang, F. (2012). Pattern formation in fluid injection into dense granular media. In *Georgia Institute of Technology* (Vol. 29, Issue 1).

Zhang, Q., Zhang, X.-P., & Ji, P.-Q. (2019). Numerical study of interaction between a hydraulic fracture and a weak plane using the bonded-particle model based on moment tensors. *Computers and Geotechnics*, *105*(August 2018), 79–93. https://doi.org/10.1016/j.compgeo.2018.09.012

Zhou, J., Chen, M., Jin, Y., & Zhang, G. qing. (2008). Analysis of fracture propagation behavior and fracture geometry using a tri-axial fracturing system in naturally fractured reservoirs. *International Journal of Rock Mechanics and Mining Sciences*, *45*(7), 1143–1152. https://doi.org/10.1016/j.ijrmms.2008.01.001

Zhou, Y., Yang, D., Zhang, X., Chen, W., & Xiong, Q. (2020). A Numerical Method for Fracture Crossing Based on Average Stress Levels. *Rock Mechanics and Rock Engineering*, *53*(10), 4471–4485. https://doi.org/10.1007/s00603-020-02054-x

Zou, Y., Zhang, S., Ma, X., Zhou, T., & Zeng, B. (2016). Numerical investigation of hydraulic fracture network propagation in naturally fractured shale formations. *Journal of Structural*

Geology, *84*, 1–13. https://doi.org/10.1016/j.jsg.2016.01.004